UNIVERSITÁ DEGLI STUDI DI PADOVA
Department of Mathematics

PhD School in Civil and Environmental Engineering Sciences
XXVI Cycle

CONTRIBUTION TO MODELING OF SOIL-PLANT-ATMOSPHERE INTERACTIONS AND COUPLED HYDRO-GEOPHYSICAL DATA ASSIMILATION

PhD School Director: Prof. Stefano Lanzoni
Supervisor: Prof. Mario Putti

PhD Student: **Gabriele Manoli**

January 2014

> “*As far as the propositions of mathematics*
> *refer to reality, they are not certain,*
> *and as far as they are certain,*
> *they do not refer to reality.*”
>
> A. Einstein, *Geometry and Experience*, 1921

Contents

List of Figures

List of Tables

Summary

Understanding the complex feedback mechanisms regulating the land-atmosphere system has become a scientific imperative, as human induced changes may impact the stability of the Biosphere, both locally and globally. The present thesis work aims at improving current understanding and forecasting capabilities of the Soil-Plant-Atmosphere (SPA) continuum. To this purpose a numerical model of soil moisture dynamics is coupled with plant transpiration and photosynthesis. Soil moisture dynamics is modeled by the 3-D Richards equation and plant uptake is described by an Ohm's law type model accounting for water potential gradients and root, xylem and stomatal conductances. The transpiration flux from soil to the atmosphere is driven by the leaf water potential which is controlled by both local soil moisture conditions and atmospheric forcing. The hydraulic model is linked to the atmosphere by the calculation of the stomatal conductance which is optimized for maximum carbon gain considering Fickian mass transfer of CO_2 and H_2O through stomata and a biochemical model of photosynthesis. The model is used to investigate competition for water among multiple tree rooting systems in a Loblolly pine (*Pinus Taeda*) plantation and then coupled with a crop growth module to investigate farmland productivity at the field scale. In order to provide a fully-coupled description of the SPA system, the soil-plant model is then coupled with a slab representation of the Atmospheric Boundary Layer (ABL) and used to investigate the role of water table fluctuations and free atmospheric state on convective rainfall initiation. Model results compared well with measurements of soil moisture, sap flow in the plant xylem as well as energy fluxes above the canopy and convective rainfall initiation time.

In order to deal with the high degree of uncertainty related to both measurement and model errors the applicability of a data assimilation algorithm has also been explored to incorporate physical measurements into the transient hydrological model. Given the recent development of indirect geophysical surveys to monitor soil-plant interactions in the vadose zone, we tested an innovative iterative particle filter approach for coupled hydro-geophysical inversion of Electrical Resistivity Tomography (ERT) data. Model results demonstrate the ability of the method to improve model prediction and estimate multiple model parameters and this work lays the foundation for application of the methodology to soil-plant-atmosphere modeling.

Sommario

La comprensione dei molteplici meccanismi che regolano l'interazione tra suolo, vegetazione e atmosfera è oggi divenuta un imperativo nel campo della ricerca scientifica, poichè numerose sono le conseguenze che la presenza antropica può avere sulla stabilità della Biosfera, a livello sia globale che locale. Questo lavoro di tesi si propone l'obiettivo di sviluppare nuovi strumenti modellistici che consentano una più accurata comprensione e descrizione del sistema suolo-vegetazione-atmosfera. A tal fine, un modello di trapirazione e fotosintesi della vegetazione è stato introdotto in un codice numerico per la descrizione del flusso in mezzi porosi. La dinamica dell'umidità del suolo è descritta dall'equazione tridimensionale di Richards, mentre il trasporto d'acqua attraverso le radici ed all'interno della pianta è definito tramite un modello di resistenze e potenziali idrici basato sulla legge di Ohm. Il flusso traspirativo è regolato dal potenziale fogliare, a sua volta determinato da condizioni locali di umidità del suolo e dalle forzanti atmosferiche. Il modello idraulico di assorbimento radicale è collegato all'atmosfera tramite il calcolo della resistenza stomatica, determinata sulla base di un modello di ottimizzazione dell'apertura degli stomi che massimizza la fotosintesi (descritta per mezzo di un modello biochimico) e minimizza la traspirazione. Tale approccio modellistico è stato impiegato per comprendere i meccanismi di competizione tra diverse piante per l'assorbimento idrico in una piantagione di *Pinus Taeda.* Il modello è stato inoltre integrato con un modulo di crescita del mais (*Zea mays L.*) per studiare la produttività agricola alla scala di bacino. Al fine di descrivere in modo completo le interazioni fra vegetazione ed atmosfera, il modello è stato poi accoppiato con la dinamica dello strato limite planetario ed utilizzato per comprendere l'effetto della falda e delle condizioni dell'atmosfera libera sugli eventi di precipitazione dovuti alla formazione di nubi convettive. I risultati modellistici illustrati in questa tesi sono confrontati con osservazioni di contenuto d'acqua nel suolo, misure di flussi xilematici, flussi energetici al di sopra della *canopy* ed eventi convettivi di precipitazione, dimostrando le ottime capacità predittive del modello sviluppato.

Sia le osservazioni che i risultati numerici sono tuttavia caratterizzati da un certo grado di errore. Per ovviare a tale incertezza è stato pertanto studiato un algoritmo di assimilazione dei dati che consente di incorporare le osservazioni fisiche nel modello dinamico idrologico. Dal momento che recenti studi di settore si sono focalizzati sull'utilizzo di metodi geofisici indiretti per la caratterizzazione dei processi di interazione fra suolo e vegetazione, in questo lavoro di tesi è stato sviluppato un metodo *particle filter* iterativo per l'inversione idro-geofisica accoppiata di dati di tomografia elettrica. I risultati presentati in questa tesi dimostrano l'abilità del metodo proposto di migliorare le previsioni e stimare i parametri del modello e pongono le basi per un nuovo approccio alla simulazione numerica del sistema suolo-vegetazione-atmosfera.

1

Introduction

1.1 Motivations

Vegetated ecosystems cover approximately 30% of Earth's land surface (42 million km^2 [Bonan, 2008]), they provide many economic, ecological and social benefits [Anderegg et al., 2013] and understanding how the Soil-Plant-Atmosphere (SPA) continuum responds to anthropogenic modifications (e.g. groundwater pumping, deforestation) or climate change (rising temperature and CO_2) is an open challenge. Over the last 20 years the interaction between hydrology and plants dynamics received increasing attention within the climate, hydrologic, and ecological communities [Rodrguez-Iturbe and Porporato, 2004] leading to the current improved understanding of the hydrologic cycle and the way ecosystems operate and survive [Rodrguez-Iturbe and Porporato, 2004].

The description of the SPA system initially relied on the simple concepts of field capacity and available water [Santini, 2013] but the development of more sophisticated monitoring techniques and modeling approaches led to a more accurate, highly dynamic and non-linear description of the SPA system, accounting for both soil and atmospheric feedback mechanisms. Recent studies highlighted the importance of a better understanding of the ecosystem-climate feedbacks with regard to regional albedo, precipitation and water and energy exchange [Anderegg et al., 2013]. In fact, although these kinds of consequences have already been partially explored [e.g., de Arellano et al., 2012], some key gaps still persist due to the large number of interacting biotic and abiotic processes occurring within the SPA system at different space and time scales [Siqueira et al., 2009]. Hence the need for more accurate mechanistic models capable of describing the complex feedback mechanisms regulating the energy, water and carbon fluxes between the biosphere and the atmosphere.

Another emerging research area in soil physics consists in the use of non invasive, time lapse geophysical measurements to quantify water balance exchanges in the root-soil system [Jury et al., 2011]. As a matter of fact, the current understanding of the soil-plant interactions is limited by a lack of spatially extensive data describing the dynamics of root water uptake processes [Boaga et al., 2013]. Traditional ecohydrological monitoring consisted in point-based measurements (lacking of spatial information) or remote sensing techniques (unable to penetrate deep in the root-zone). Non-invasive geophysical techniques such as Electrical Resistivity Tomography (ERT) are promising alternatives to monitor soil moisture dynamics in the root zone and quantify the spatial distribution of plants water use [Boaga et al., 2013, Garré et al., 2011, Srayeddin and Doussan, 2009]. However, to achieve a quantitative description of soil moisture dynamics, geophysical observations has to be included in a modeling framework. The understanding of subsurface phenomena is thus affected by a high degree of uncertainties related to both measurements and model errors and the development of more accurate inversion techniques capable of providing quantitative information on subsurface hydrological variables is a contemporary challenge.

This thesis is a contribution to modeling the ecohydrological feedback mechanisms regulating the SPA system. The physical processes investigated in this study are illustrated in Fig. 1.1 and briefly outlined in the next section. First an innovative Soil-Plant-Atmosphere model is developed and applied to different case studies. Then the ability of geophysical surveys to monitor vadose zone processes is discussed and an innovative data assimilation framework for the coupled hydro-geophysical inversion of ERT data is proposed.

1.2 Outline

In this dissertation we present an innovative SPA continuum model based on a mechanistic description of plant transpiration and photosynthesis coupled with the three-dimensional Richards equation for soil moisture dynamics. The soil-plant hydraulic model accounts for soil-root and trunk xylem conductances to describe root water uptake (RWU) at the tree scale and it is linked to the atmosphere via a stomatal conductance model that combines a conventional biochemical formulation for photosynthesis with an optimization hypothesis that regulates stomatal aperture in order to maximize carbon uptake and minimize the evaporative water loss. In Chapter 2, the model is developed and applied to a Loblolly pine plantation in North Carolina, USA. The novelty of the modeling approach consists in embedding plant physiological mechanisms in a robust three-dimensional soil moisture model. Such a modeling framework allows to diagnose plant responses to water stress in the presence of competing rooting systems and generalize plant-water relations at larger scales.

Given the three-dimensionality of the new approach, the model is then applied to simulate the ecohydrological processes governing farmland productivity in a crop field. In Chapter 3 the model is coupled with a crop growth module and applied to a case study on the southern margin of the Venice lagoon, Italy. Part of this research consisted in field data collection: geophysical surveys, lab testing and continuous monitoring of hydrological parameters together with crop yield distribution were performed and acquired from 2010 to 2012. The dataset is presented in Chapter 3 and used to set up field scale simulations of soil-crops dynamics.

The Soil-Plant model is then coupled with a slab representation of the Atmo-

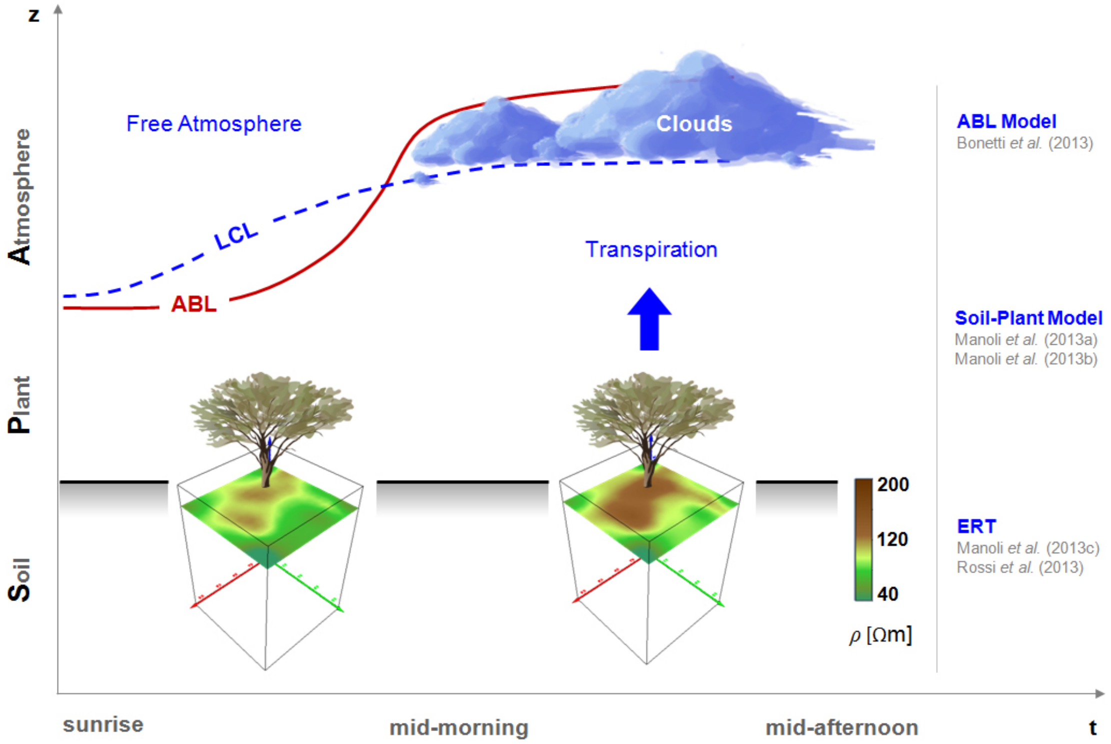

Figure 1.1: Thesis outline: first a Soil-Plant model is developed and applied to different case of studies (Chapter 2 and 3); then the model is coupled with a slab representation of the ABL and LCL to explore the role of vegetation on convective triggering (Chapter 4); finally a data assimilation framework is developed for the coupled inversion of resistivity (ρ) data (Chapter 5). An example of monitoring the Soil-Plant system by ERT is shown (data from [Boaga et al., 2013]). The results presented in this dissertation have been published [Manoli et al., 2013b] or submitted for publication [Bonetti et al., 2013, Manoli et al., 2013a,c, Rossi et al., 2013]

spheric Boundary Layer (ABL) and used to gain insight into the complex feedback mechanisms governing surface energy fluxes and convective rainfall initiation (Chapter 4). As a matter of fact the transpiration fluxes control the dynamics of the ABL and the Lifting Condensation Level (LCL) and thus their crossing (a necessary but not sufficient condition for convection trigger). In Chapter 4 the coupled SPA-ABL model is parametrized on the field case study in North Carolina and used to explore the role of water table fluctuations and free atmosphere (FA) conditions on convective rainfall initiation. Simulation results demonstrate the interplay of soil and FA conditions on convection triggers suggesting the existence of a rainfal-no rainfall transition zone.

The results presented in Chapter 2 and 3 highlighted the need for spatial extensive information to understand the complex dynamics of soil-plant interactions. In Chapter 5 the ability of ERT to monitor vadose zone processes is investigated. In order to overcome the limitations of traditional inversion of ERT data we propose a sequential data assimilation approach to combine geophysical observations with hydrological simulations [Pasetto et al., 2012, Rings et al., 2010]. We use the Sequential Importance Resampling (SIR) method to assimilate ERT measures in a coupled hydrogeophysical model: ERT observations are blended in the simulation to update the state of the system and estimate the model parameters accounting for both model and observations uncertainties. The methodology is tested on a controlled infiltration experiment (avoiding the presence of vegetation) in order to efficiently evaluate the performance of the method. The long term objective is to couple numerical modeling with ERT monitoring of the soil-plant system, but the application of the method to vegetated conditions is left for future work.

2

Modeling Soil-Plant-Atmosphere Interactions

2.1 Summary

In this chapter competition for water among multiple tree rooting systems is investigated using a soil-plant model that accounts for soil moisture dynamics and root water uptake (RWU), whole plant transpiration, and leaf-level photosynthesis. The model is based on a numerical solution to the 3D Richards equation modified to account for a 3D RWU, trunk xylem, and stomatal conductances. The stomatal conductance is determined by combining a conventional biochemical demand formulation for photosynthesis with an optimization hypothesis that selects stomatal aperture so as to maximize carbon gain for a given water loss. Model results compare well with measurements of soil moisture throughout the rooting zone, of total sap flow in the trunk xylem, as well as of leaf water potential collected in a Loblolly pine forest. The model is then used to diagnose plant responses to water stress in the presence of competing rooting systems. Unsurprisingly, the overlap between rooting zones is shown to enhance soil drying. However, the 3D spatial model yielded transpiration-bulk root-zone soil moisture relations that do not deviate appreciably from their proto-typical form commonly assumed in lumped eco-hydrological models. The increased overlap among rooting systems primarily alters the timing at which the point of incipient soil moisture stress is reached by the entire soil-plant system. The contents of this chapter has been submitted for publication to *Advances in Water Research*:

Manoli, G., Bonetti, S., Domec, J. C., Putti, M., Katul, G., and Marani, M. (2013a). Tree root systems competing for soil moisture in a 3D soil-plant model. *Submitted.*

2.2 Introduction

Background Forest ecosystems provide many economic, ecological and social benefits [Anderegg et al., 2013] and play a key role in regulating the energy, carbon, and water fluxes between the biosphere and the atmosphere. Soil water is extracted by plant roots, flows through the plant vascular system and evaporates from the plant leaves thus providing a bridge in which soil water reservoir and atmospheric water vapor concentration interact. Root water uptake (RWU) controls the water dynamics in the subsurface, thereby affecting plant water availability [Couvreur et al., 2012], soil water content [Huxman et al., 2005], and the partitioning of net radiation into latent and sensible heat fluxes thereby impacting atmospheric boundary layer dynamics [Anderegg et al., 2013, de Arellano et al., 2012, Maxwell et al., 2007]. Yet, despite its documented importance, a number of thorny issues remain when representing RWU in hydrological and atmospheric models [Dirmeyer et al., 2006], and addressing a subset of these issues frames the compass of this work. Among the least studied of these issues is the representation of RWU when competition among trees for available root-water occurs. Such competition is rarely accounted for in conventional ecological and hydrological models. Earlier work mostly focused on grass-trees competition in the vertical dimension. In this type of competition, it was assumed that deep tree roots use water not consumed by the shallow grass rooting system [Richard et al., 2011, Rodrguez-Iturbe et al., 1999a] and the competition for RWU becomes apparent when vertically-averaging the grass-tree rooting system [Daly et al., 2000, Rodrguez-Iturbe et al., 1999a]. Even within this restricted representation, resolving such rooting competition was shown to be essential in reproducing biomass dynamics [Daly et al., 2000, Rodrguez-Iturbe et al., 1999a]. One of the barriers to progressing on the root-water competition issue is the inherent three-dimensional nature of the problem. Here, a new 3D model of RWU is developed to investigate the effects of overlapping root-systems within a forest canopy so as to infer up-scaled representation of such competition effects on bulk ecohydrologic models.

RWU Modeling Modeling RWU requires coupling plant transpiration and photosynthesis together with a three-dimensional evolving soil moisture field. Two main approaches, both based on Richards' equation to describe soil water dynamics [Couvreur et al., 2012], have been used to model RWU: (1) a macroscopic approach and (2) a microscopic approach that accounts for the detailed root architecture. The first approach accounts for RWU by introducing a "macroscopic" sink term, generally defined as a function of spatially-distributed root parameters (e.g. root length density). This approach assumes that the vertically integrated RWU can be represented via a potential transpiration dictated by atmospheric demand for water vapor modulated by an ad-hoc water stress function (e.g. Feddes approach Feddes et al. [1978]). Some compensatory mechanisms have been incorporated within such a framework Jarvis [1994], Šimůnek et al. [2006]. When water potential gradients (WPG) are employed, this approach can reproduce important processes such as hydraulic redistribution (HR) [Vogel et al., 2013]. HR has been observed in a number of experiments [Caldwell and Richards, 1989, Domec et al., 2010] and included in different modeling approaches [Amenu and Kumar, 2008, Domec et al., 2012, Mendel et al., 2002, Neumann and Cardon, 2012, Siqueira et al., 2008, 2009, Vogel et al., 2013, Volpe et al., 2013]. While most models in this class can satisfactorily reproduce both compensation and redistribution mechanisms, they generally use a vertically distributed RWU approximation, thereby censoring any horizontal interactions among plants. Multidimensional macroscopic models do exist [Ivanov et al., 2008, Šimůnek et al., 2006], but they generally use simplified RWU functions that may be unrealistic in heterogeneous soils [Kuhlmann et al., 2012]. The importance of a three-dimensional perspective has been recently underlined [Javaux et al., 2008] spawning a number of simulations of water flow through soil and roots using a root hydraulic network [Couvreur et al., 2012, Doussan et al., 2006, Javaux et al., 2008, Kalbacher et al., 2011]. This second approach includes detailed plant-scale models based on explicitly resolved root architecture coupled with the three-dimensional Richards equation for water flow in the soil-root system of an isolated single small plant or seedling [Couvreur et al., 2012, Doussan et al., 2006, Javaux et al., 2008]. Because the precise root architecture for multiple interacting trees is rarely known a priori, and given the computational demands involved, a root architecture approach is not yet feasible for large scale hydrological simulations. An intermediate approach that retains the 3D properties of the problem and yet provides a numerically-viable simplified RWU approach is needed when exploring the interplay of hydrological, physiological, and ecological mechanisms at the watershed scale. Existing 3D models (belonging to both categories) commonly neglect photosynthetic activity of the plant, which largely controls transpiration, and hence RWU. An approach that also accommodates these mechanisms and can be embedded in a robust three-dimensional soil moisture model offers a decisive advantage when generalizing plant-water relations at larger scales. With such a representation, the competition between plants for soil water (e.g. neighboring trees in a forest stand) can be made explicit and its effects on upscaled watershed processes can be explored.

Objectives The main objective here is to develop a mechanistic 3D model of RWU so as to explore the implications of root competition on ecosystem transpiration and carbon uptake. More specific objectives are to (1) develop and apply a soil-plant-atmosphere model incorporating a 3D description of soil water dynamics, (2) investigate the effects of some biotic and abiotic compensatory mechanisms such as HR and Darcian redistribution on RWU and water use efficiency, and (3) evaluate the effects of tree-to-tree overlapping root zones on ecosystem level RWU rates. The main novelty is a framework in which a 3D hydrological model is coupled to plant transpiration and leaf photosynthesis that is then used to explore root water uptake for overlapping tree rooting systems in the presence of dynamic groundwater fluctuations.

2.3 Mathematical model

The transpiration flux is expressed in terms of gradients in water potential through a series of conductances along the pathway connecting water from the soil (ψ_i), to the xylem (ψ_R), and to the leaf (ψ_L), (Fig. 4.1). Stomatal conductance is assumed to maximize carbon gain, while minimizing water loss. The following assumptions are made Volpe et al. [2013]:

- a1) water extracted by roots only feeds transpiration and no water storage occurs within the plant system,
- a2) each soil layer is directly linked to the xylem through the root biomass allocated to the same layer,
- a3) energy losses in the root system are negligible compared to the dissipation in the soil and soil-root interface,
- a4) RWU is not limited by any other mechanism (e.g. nutrient limitation).
- a5) root growth is here ignored, though it may be significant at long time scales.

2.3.1 Soil-Plant exchanges

A recent 1D root model [Volpe et al., 2013] is expanded here to a 3D general framework. Richards' equation is used to describe soil moisture dynamics in a three-dimensional porous medium and is given as:

$$S_s S_w(\psi)\frac{\partial \psi}{\partial t} + n\frac{\partial S_w(\psi)}{\partial t} = \vec{\nabla}\cdot\left[\mathbf{K}_s K_r(\psi)\left(\vec{\nabla}\psi + \eta_z\right)\right] + q(\psi, x, y, z, t, \psi_L), \quad (2.1)$$

where S_s is the elastic storage term [m^{-1}], S_w is water saturation [-], ψ is the soil water potential [m], t is time [s], n is the porosity [-], $\mathbf{K}_s$ is the saturated hydraulic conductivity [m s^{-1}] tensor, K_r is the relative hydraulic conductivity [-], $\eta_z = (0,0,1)^T$ is the gravitational potential energy gradient with z, the vertical coordinate, directed upward and $q(\psi, x, y, z, t, \psi_L)$ is a macroscopic source/sink term [s^{-1}] through which soil water dynamics is coupled with the root-plant system via the leaf water potential ψ_L. Anisotropic saturated hydraulic conductivity is modeled as a diagonal matrix with diagonal elements K_x, K_y, and K_z, the saturated hydraulic conductivities along the coordinate directions. Eq. (5.9) is highly nonlinear due to the functional dependence upon pressure head of the soil water retention curves, which are modeled following [van Genuchten and Nielsen, 1985]. The numerical solution to Eq. (5.9) is obtained by means of a Finite Element approach with linear (P1) basis functions and implicit Euler time-stepping, as implemented in the CATHY model [Camporese et al., 2010]. The scheme considers nonlinear boundary conditions at the soil surface to account for ponding or evaporation limitations due to variable surface soil moisture. The numerical solver is based on an unstructured tetrahedral grid and employs time step adaptation to ensure convergence for highly nonlinear problems and address the ODE stiffness resulting from the discretization of the nonlinear source term. Inexact Krylov-based Picard iteration with ad hoc efficient preconditioning is used in the solution of the nonlinear system of equations [Bergamaschi et al., 2013, 2006, Paniconi and Putti, 1994]. Discretization of the source term is obtained by means of the second order accurate midpoint rule,

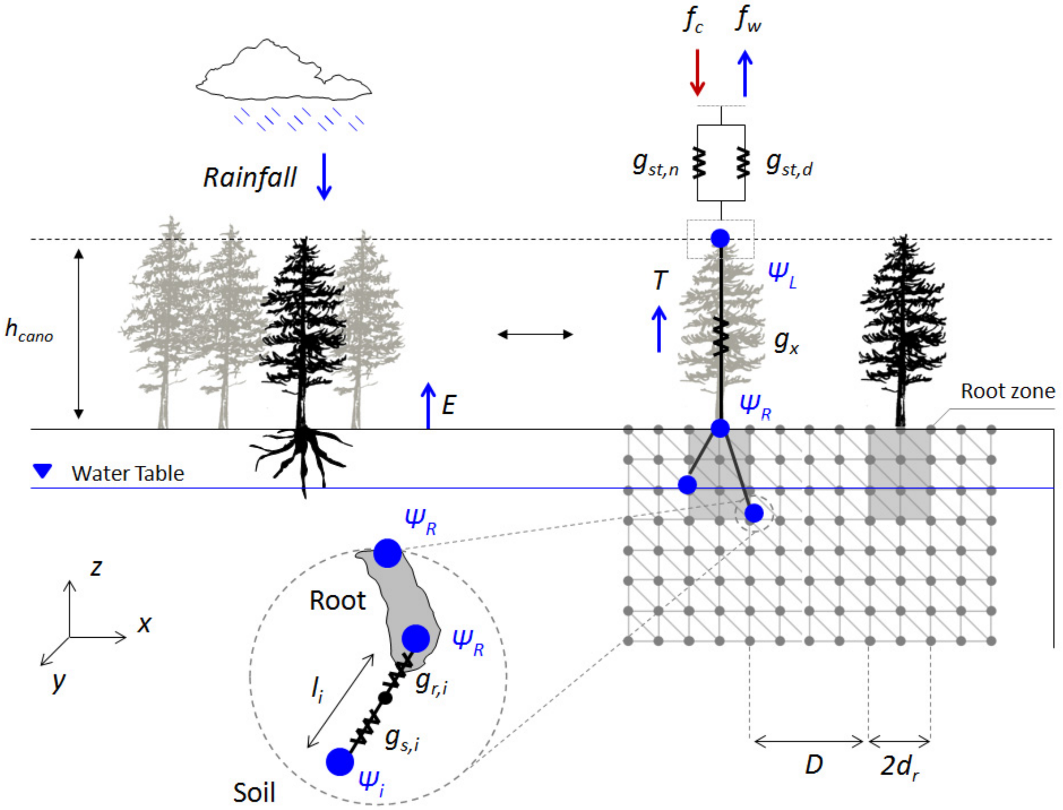

Figure 2.1: Model structure: (a) the pathway of water movement from the soil through the plant system into the atmosphere modeled using a series of conductances. Water fluxes are proportional to potential energy gradients between the soil (ψ_i), the root system (ψ_R), and the leaves (ψ_L). Rainfall, soil evaporation and water table fluctuations are specified as boundary conditions and the root water competition between neighboring trees is evaluated by changing the spacing D between two identical pine trees, each having a root zone length d_r.

by which at each grid node i the source term $q_i = q(\psi_i, x_i, y_i, z_i, t, \psi_L)$ is multiplied by the corresponding nodal soil volume V_i. Coupling between the soil and the root system proceeds as follows: Single plants are defined by a surface grid node, j (with j between 1 and the number of plants in the model domain), which can be identified as the base of the plant trunk. The total water uptake per unit soil volume from node i, appearing in Eq. (5.9), is expressed as the uptake from all plants having non-zero root biomass at node i, i.e. $q_i = \sum_j q_{i,j}$. The term $q_{i,j}$ is the soil water uptaken (per unit soil volume) by the roots of plant j at grid node i. A plant node j is connected to each soil node within its root zone through a conductance, $g_{i,j}$, representing the path traveled by water from the soil pores into the nearest root within the finite element centered in i. The conductance $g_{i,j}$ expresses the water flux from the soil to the root (or viceversa) crossing the root membrane per unit area of the membrane and per unit difference of the total water potential between the soil and the root (see inset in Figure 4.1). To obtain the flux per unit soil volume of the domain entering (or exiting) the root system at node i, it is necessary to account for the total root surface area per unit soil volume, $a_{R,i}$ [m^2_{root} m^{-3}_{soil}], such that the soil water (per unit soil volume) uptaken by the roots of plant j at grid node i is:

$$q_{i,j} = -g_{i,j} \left[(\psi_{R,j} + z_{R,j}) - (\psi_i + z_i) \right] a_{R,i}. \tag{2.2}$$

The total root surface area per unit soil volume is computed as $a_{R,i} = 2\pi r B_i$, where the effective root radius r is assumed to be 2 mm and B_i is the root length density at node i [m_{root} m^{-3}_{soil}]; $z_{R,j}$ is the elevation of the base of the trunk and z_i is the elevation of the i-th grid node [m]. Because of assumption 3 above, the hydraulic head is everywhere constant within the root system set to $\psi_{R,j} + z_{R,j}$, which appears in Eq. (A.2) irrespective of the specific node i considered (see Fig. 4.1). The total soil-to-root conductance, $g_{i,j}$, is calculated by considering the effect of soil conductance ($g_{s,i}$), relative to the average path traveled by water from the soil to the nearest root, and of the root membrane conductance ($g_{r,i}$). The conductance of the path traveled within the soil to the nearest root is $g_{s,i} = K_i l_i^{-1}$, where $K_i = \|K_s K_r\|_i$ is the norm of the soil hydraulic conductivity [m s^{-1}] evaluated at node i and l_i the rizhosphere radius [m], i.e. the mean length traveled from the bulk soil to the root surface. According to Vogel et al. [2013], the length l_i can be estimated as $l_i = \alpha/\sqrt{\pi B_i}$, where $\alpha = 0.53$ is an empirical coefficient. The effective conductance (not conductivity) resulting from two conductances in series is given by $g_{i,j} = (g_{s,i} \cdot g_{r,i})/(g_{s,i} + g_{r,i})$ [Volpe et al., 2013].

The value of $\psi_{R,j}$ is now determined by equating the total water flux uptaken by the root system of plant j, $\sum_i T_j = q_{i,j} \cdot V_i$, to the transpiration rate driven by the potential energy gradient between the trunk base and the leaf [Volpe et al., 2013]. This equality yields

$$T_j = -g_{x,j} \left[(\psi_{L,j} + z_{L,j}) - (\psi_{R,j} + z_{R,j}) \right] A_{x,j}, \tag{2.3}$$

where $\psi_{L,j}$ is the leaf water potential (discussed later), $g_{x,j}$ is the xylem conductance, $A_{x,j}$ is the xylem cross sectional area [m^2], and $z_{L,j}$ is the elevation at which the effective leaf water potential is evaluated at [m]. The conductance $g_{x,j}$ accounts for the vulnerability of the xylem to cavitation according to Daly et al. [2004] (see Appendix for details). The pressure head in the xylem, $\psi_{R,j}$ can be expressed as [Volpe et al., 2013]:

$$\psi_{R,j} = \frac{g_{x,j} A_{x,j} (\psi_{L,j} + h_{c,j}) + S1_j}{S2_j + g_{x,j} A_{x,j}}, \tag{2.4}$$

where $h_{c,j} = z_{L,j} - z_{R,j}$ is the canopy height, $S1_j = \sum_i g_{i,j} a_{R,i} (\psi_i - d_{i,j}) V_i$, $d_{i,j}$ being the difference in elevation between the i-th soil node and the base of the trunk, and $S2_j = \sum_i g_{i,j} a_{R,i} V_i$. The leaf water potential $\psi_{L,j}$ is unknown and, due to the dependence of the sink term $q_{i,j}$ on $\psi_{L,j}$, Eq. (5.9) is under-constrained. A leaf scale mass transfer model is now needed to mathematically close the problem.

2.3.2 Plant-Atmosphere

Even though a single $\psi_{L,j}(t)$ is used to represent the water potential in the entire canopy, the model here incorporates a vertically-explicit description of the light regime. This description decomposes the leaf area into vertical layers so as to account for light attenuation and its effects on the photosynthesis calculations [Volpe et al., 2013]. At each canopy layer, the leaf-scale transpiration is defined by the mass transfer of water vapor between the leaf and the atmosphere at the canopy layer r:

$$f_{w,j,r}\left(\psi_{L,j}\right) = a\; g_{st,j,r}\left(\psi_{L,j}\right) VPD\; \epsilon_w \tag{2.5}$$

where $a = 1.6$ is the relative diffusivity of water vapor with respect to CO_2, $g_{st,j,r}$ is the CO_2 stomatal conductance at canopy layer r [mmol m^{-2} s^{-1}], VPD is the vapor pressure deficit (assuming that the leaf is well coupled to the atmosphere) and $\epsilon_w = MW_w/\rho_w$, where MW_w [g mol^{-1}] and ρ_w [kg m^{-1}] are molar weight and density of water, respectively. The VPD is computed as the difference between vapor pressure at saturation and ambient conditions [Volpe et al., 2013]. Here, air temperature, water vapor and CO_2 concentrations are assumed to be vertically uniform within canopy air volume set to their (time-varying) measured values above the canopy and only the light regime is determined at different canopy layers. The leaf photosynthesis at canopy layer r is described by a biochemical demand function [Farquhar et al., 1980]:

$$f_{c,j,r} = \frac{a_{1,r}}{a_2 + c_{ic,r}}\left(c_{ic,r} - c_{cp}\right), \tag{2.6}$$

where the photosynthetic parameters a_1 and a_2 are selected depending on whether light or Rubisco limits photosynthesis [Volpe et al., 2013] at layer r, c_{cp} is the CO_2 compensation point [mmol μmol^{-1}]. The inter-cellular CO_2 concentration c_{ic} can be eliminated and replaced by stomatal conductance when assuming Fickian mass transfer between the leaf and the atmosphere [Volpe et al., 2013] governs CO_2 exchange. When Rubisco is limiting $a_1 = V_{c,max}$ and $a_2 = K_c(1 + \frac{C_{o,a}}{K_o})$ where $V_{c,max}$ is the maximum carboxylation capacity referenced at 25°C, K_c and K_o are the Michaelis constants for, respectively, CO_2 and O_2 fixation at 25°C and $C_{o,a}$ is the oxygen concentration in the atmosphere. When light is the limiting factor, $a_1 = \gamma Q_{p,r}$ and $a_2 = 2c_{cp}$, where γ is the apparent quantum yield [-], $Q_{p,r}$ is the photosynthetically active radiation at the canopy layer r [μmol m^{-2} s^{-1}]. Light attenuation within the canopy is modeled using an extinction coefficient accounting for leaf angle distribution and solar zenith angle [Volpe et al., 2013]. The photosynthetic parameters are adjusted for air temperature as described elsewhere [Campbell and Norman, 2000]. Stomatal conductance is optimized for maximum carbon gain according to a linearized formulation also described elsewhere [Katul et al., 2010, Volpe et al., 2013]. Because nocturnal transpiration can be significant [Domec et al., 2012, Novick et al., 2009, Vogel et al., 2013], the leaf-level formulation [Katul et al., 2010] is modified to include nighttime transpiration. This modification is based on the fact that effective bulk leaf conductance $g_{st,j}$ accounts for both - the optimal stomatal control by the plant on the stomatal aperture, encoded in $g_{st,d}$, and a residual loss $g_{st,n}$ when stomata are almost closed (e.g. leaks due to imperfect closure, curticular, etc...). Under the assumption that these pathways are parallel (Fig. 4.1), it follows that $g_{st} = g_{st,d} + g_{st,n}$. As conventional in stomatal optimization theories [Katul et al., 2010], an objective function for the plant is assumed to be maximizing the leaf carbon gain f_c at a given water loss f_w (in units of carbon) for a species-specific water use efficiency λ. The following objective function can thus be defined: $f(g_s) = f_c - \lambda \cdot f_w$. Assuming that leaves optimally and autonomously regulates $g_{st,d}$ only, it is possible to set $\partial f(g_{st})/\partial g_{st,d} = 0$ and solve for $g_{st,d}$. Hence, it follows that at the canopy layer r [Katul et al., 2010]:

$$g_{st,r}(\psi_L) = \frac{a_{1,r}}{a_2 + s\ c_a}\left[-1 + \left(\frac{c_a}{a\ \lambda(\psi_L)\ VPD}\right)^{1/2}\right] + g_{st,n}, \tag{2.7}$$

where s is a model constant connected to the long-term c_i/c_a, c_a [mmol mol^{-1}] is the CO_2 concentration in the atmosphere and the cost parameter λ [μmol mol^{-1}], i.e. the cost of water for the plant to complete the photosynthesis, is estimated from the time-integrated leaf water potential according to Manzoni et al. [2011]. We refer to Katul et al. [2010], Volpe et al. [2013] for further details on the optimality model. The nocturnal stomatal conductance $g_{st,n}$ can be determined from the relation between sapflow and VPD [Domec et al., 2012]. Since the cost parameter varies over much longer time scales than the leaf potential (e.g. daily), a single value of λ is used for the different canopy layers (but time varying) and the center of the canopy is used in the calculations of $\psi_{L,j}(t)$ [Volpe et al., 2013].

2.3.3 Non-linear closure equation

Because of the flux continuity across the soil-plant system, integrating Eq. (2.5) over the leaf area and equating to Eq. (2.3) leads to the following nonlinear closure equation for plant j:

$$G_j\left(\psi, \psi_{L,j}\right) = T_j\left(\psi, \psi_{L,j}\right) - \sum\nolimits_r f_{w,j,r}\left(\psi_{L,j}\right) \cdot LAI_{j,r} \cdot A_{c,j} = 0, \tag{2.8}$$

where $A_{c,j}$ is the canopy projected area [m^2] and $LAI_{j,r}$ is the leaf area index at the canopy layer r [m$^2_{leaf}$ m$^{-2}_{soil}$]. Eq. (5.9) is defined for every plant j and is coupled to the discretized Richards equation to augment the nonlinear system for the variable $\psi_{L,j}$. Because of the presence of several inflection points in G_j, the numerical solution is obtained by the secant method at every Picard iteration (see Appendix).

2.4 Case study: A Loblolly pine plantation

2.4.1 Site description

The model is evaluated using a 2-year data set collected in a Loblolly pine plantation situated in the lower coastal plain of North Carolina, USA (35° 11' N, 76° 11' W). A description of the study area and data collected can be found elsewhere [Domec et al., 2012, Sun et al., 2010]. Briefly, the plantation (denoted as US-NC2 in the Ameriflux database) is a 100 ha mid-rotation Loblolly pine stand established in 1992 after clear cutting the mature pine trees [Domec et al., 2012]. The trees were planted at a 1.5 m × 4.5 m spacing [Sun et al., 2010]). The plantation is drained by a network of parallel ditches (90 - 130 cm deep; 90 m spacing) and more widely spaced roadside canals. The meteorological, hydrological, and eco-physiological data used were collected during years 2007 and 2008. Input micro-meteorological data

Table 2.1: Soil hydraulic parameters: porosity values n are defined according to Domec et al. [2012] and the saturated hydraulic conductivities $K_{x,y}$ and K_z are based on laboratory testing from Diggs [2004]. The residual soil moisture content θ_r, the air entry pressure ψ_s, and the exponent parameter n_{vg} are the coefficients of the soil water retention curves according to van Genuchten and Nielsen [1985].

Depth $[mbs]$	n $[-]$	K_{soil} $[ms^{-1}]$	θ_r $[-]$	ψ_s $[m]$	n_{vg} $[-]$
0.00 - 0.30	0.50	7.2×10^{-5}	0.03	-0.10	1.43
0.30 - 0.60	0.45	1.0×10^{-4}	0.02	-0.10	1.33
0.60 - 5.00	0.37	7.2×10^{-5}	0.03	-0.25	2.50

(e.g. air temperature, photosynthetically active radiation or PAR, relative humidity, rainfall) were recorded every minute and averaged every 30-minutes. Water vapor fluxes were also measured using an eddy covariance (EC) system located on the meteorological tower at the site [Sun et al., 2010]. The EC system sampling frequency is 10 Hz and the averaging period is 30 minutes, synchronized with the meteorological measurements. The soil is a stratified sequence of sandy loam (top 30 cm), sandy clay loam (0.3-0.6 m below the surface), and gray sandy clay (below 0.6 m below the surface) [Diggs, 2004, Domec et al., 2012, Sun et al., 2010]. The soil hydraulic parameters are described elsewhere [Diggs, 2004] and summarized in Table 2.1. Soil moisture was measured continuously at 10, 20, 30, 40, 50, 60, 80, and 140 cm depths using Sentek EnviroSCAN capacitance sensors (Sentek Sensor Technologies, Stepney, Australia) and water table fluctuations were monitored every hour by a groundwater well installed at the site [Sun et al., 2010]. Tree transpiration was separately determined from trunk sap flux measurements on different pine trees. Specifically, sapflux measurements were collected at 1.4 m above the ground at four radial positions using 20 mm heat dissipation probes [Domec et al., 2010]. These transpiration estimates are interpreted as the integrated RWU and are used in comparisons with model results.

2.4.2 Model run setup

The model is first compared with measured transpiration and photosynthesis for a single pine tree by using a 1D vertical domain. These simulations are intended to calibrate the model parameters, ensure a physically plausible model behavior, and provide a reference 1D case (i.e. not including competition among neighboring trees). Given the 3D nature of the model formulation, the dimensionality of the model is reduced to 1D by adopting a model domain that consists of vertical line of nodes, where Richards' equation is solved for, surrounded by nodes where boundary conditions (BCs) are imposed using measured water table levels. The vertical profile of the root length density B_i is based on Domec et al. [2012], where measurements commenced at 0.15 m below the soil surface. The B_i near the surface was determined by extrapolation using a typical exponential root distribution profile [Volpe et al., 2013]. Field measurements of the meteorological and hydrological drivers (e.g. rainfall, temperature, relative humidity, PAR, etc..) are used to calculate the atmospheric forcing. Rainfall data are corrected for canopy interception assuming an interception rate of 15% [Sun et al., 2010]. An understory EvapoTrasnpiration (ET) is calculated as the difference between the EC measured latent heat flux (LE) above the canopy converted into mass units [Sun et al., 2010] and the sap flow data. The resulting net flux is then imposed as a Neumann boundary condition at the soil surface of the model domain. Input precipitation is considered as a potential rate and actual infiltration is evaluated based on the soil current saturation state, allowing switching between Neumann and Dirichlet BCs in case of water ponding [Camporese et al., 2010].

The model is subsequently used to simulate two identical and interacting Loblolly pine trees under conditions similar to those observed within the plantation (3D simulations). Considering the tree spacing at the site, a 10 m × 5 m × 5 m model domain is used to represent a portion of the plantation thereby avoiding boundary effects on the numerical solution. The effect of tree competition for RWU is investigated by simulating a 100 days drying cycle. The atmospheric forcing recorded on July 14^{th}, 2007 (a typical day characterized by high transpiration thereby highlighting the implications of root competition on soil water availability and RWU), are repeated periodically during the simulated dry down period: the water table was kept constant at 3 m below the surface and no-flow conditions were imposed on the outer soil boundary. Simulations with different tree spacing D, defined as the distance between the root systems (such that $D < 0$ indicates partially overlapping root systems), are also explored (Fig. 4.1).

In all the 3D model calculations, the following assumptions are adopted and repeated here for clarity: (a) the root system is static (root growth is neglected) and (b) only competition for water is considered, assuming that trees do not compete for other resources. While competition for light is another major factor in forested canopies, the outcome of this competition is not explicitly considered here though it does affect canopy height, leaf area, and ratio of leaf-area to root-area index that are pre-specified here. To compress the 3D simulations so that they are comparable with the 1D simulation results, the root distribution is assumed constant in the horizontal directions and the same volume of roots as in the 1D simulations is considered. Preliminary simulations of a drying cycle were run both with the 1D and 3D set up and comparable results were obtained (not shown here for brevity). A homogeneous lateral root distribution was not based on field conditions, but it is the simplest assumption that allows addressing differences in soil water dynamics and transpiration responses when comparing the 1D and 3D setups.

2.5 Results and discussions

2.5.1 Model calibration

A comparison between measured and modeled soil moisture is presented in Fig. 2.2 for the entire year of 2007. The model satisfactorily captures the observed soil moisture pattens at all depths. The initial discrepancy between simulations and mea-

Table 2.2: Plant model parameters: values are based on previous literature or on field measurements.

Parameter	Description	Unit	Value	Reference
Plant parameters				
h_{cano}	Plant/Canopy height	m	17	Domec et al. [2012]
A_{cano}	Projected canopy area	m^2	9	Assumed
A_{xylem}	Xylem area	m^2	0.06	Assumed
r	Root radius	m	0.02	Assumed
RAI	Root Area Index	m^2 m^{-2}	2.1 - 4.7	Domec et al. [2012]
g_r	Root conductance	s^{-1}	$3{\times}10^{-11}$	Assumed
B	Root lenght density	cm cm^{-3}	0.07 - 3.70	Domec et al. [2012]
LAI	Leaf Area Index	m^2 m^{-2}	2.5 - 5.6	Domec et al. [2012]
Xylem conductance				
$g_{x,max}$	Maximum xylem conductance	s^{-1}	$5{\times}10^{-6}$	Assumed
d	Vulnerability curve coefficient	m	200	Aspinwall et al. [2011], Volpe et al. [2013]
c	Vulnerability curve coefficient	-	2	Aspinwall et al. [2011], Volpe et al. [2013]
Photosynthetic model				
$V_{c,max25}$	Maximum carboxylation capacity at 25°C	μmol m^{-2} s^{-1}	41	Domec et al. [2012]
$K_{c,max25}$	Michaelis constant for CO_2 fixation at 25°C	μmol mol^{-1}	300	Volpe et al. [2013]
$K_{o,max25}$	Michaelis constant for O_2 fixation at 25°C	mmol mol^{-1}	300	Volpe et al. [2013]
$c_{p,25}$	CO_2 compensation point at 25°C	mmol μmol^{-1}	2.6	Volpe et al. [2013]
Stomatal optimality model				
λ^*_{max}	Maximum marginal water use efficiency	μmol mol^{-1}	1755	Manzoni et al. [2011]
β	Empirical parameter	m^{-2}	$1.2{\times}10^{-5}$	Manzoni et al. [2011]
$\psi_{L,max}$	Leaf water potential at maximum λ	m	-277	Manzoni et al. [2011]
γ	Apparent quantum yield	-	0.015	Samuelson et al. [2001]
a	Relative H_2O/CO_2 diffusivity	-	1.6	Katul et al. [2010], Volpe et al. [2013]
s	Coefficient for g_s calculation	-	0.7	Katul et al. [2010], Volpe et al. [2013]
$C_{o,a}$	O_2 concentration in air	mmol mol^{-1}	210	Katul et al. [2010], Volpe et al. [2013]
c_a^*	Reference CO_2 concentration	μmol mol^{-1}	400	Katul et al. [2010], Volpe et al. [2013]
c_a	Ambient CO_2 concentration	mmol mol^{-1}	380	Katul et al. [2010], Volpe et al. [2013]
$g_{s,n}$	Nocturnal stomatal conductance	mmol m^{-2} s^{-1}	18	Domec et al. [2012]

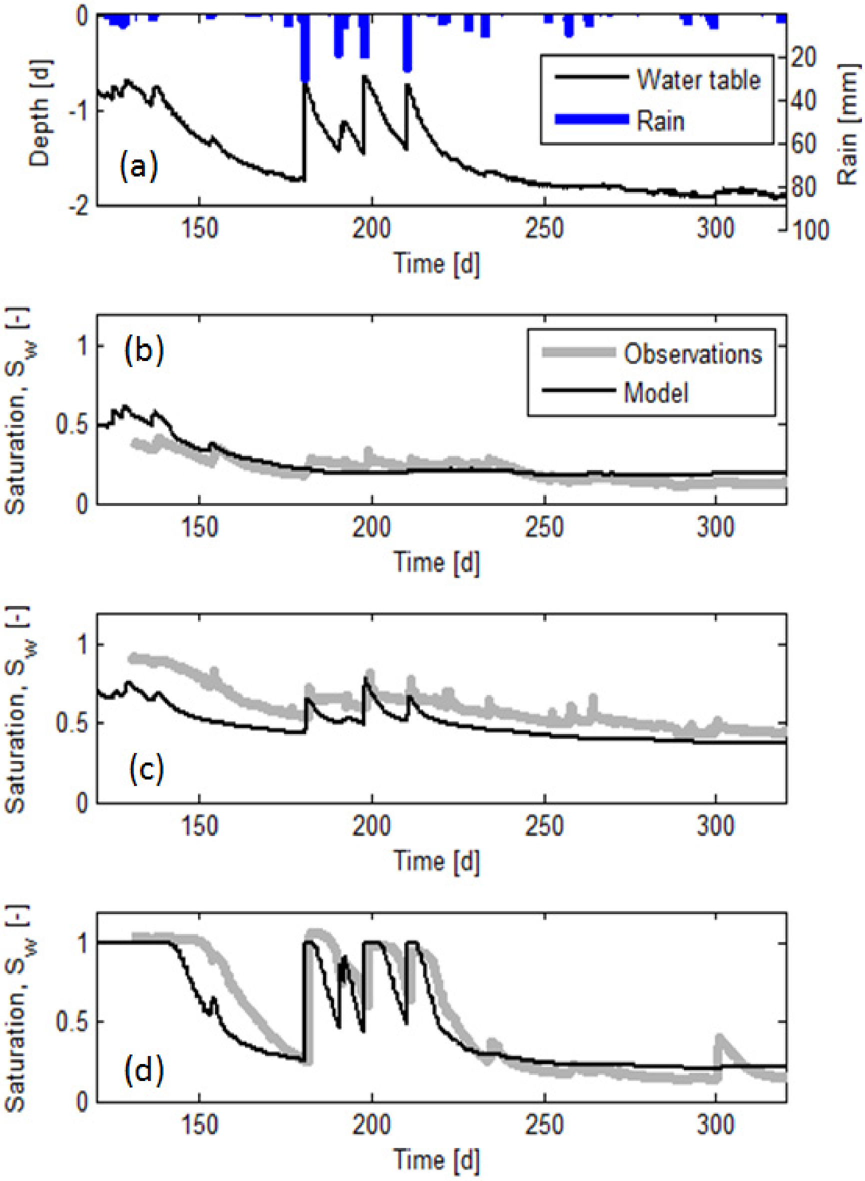

Figure 2.2: Soil water dynamics: (a) rainfall events and water table fluctuations observed at the site during year 2007. Model results are compared with soil saturation S_w measured at a depth of (b) 10 cm, (c) 50 cm and (d) 100 cm.

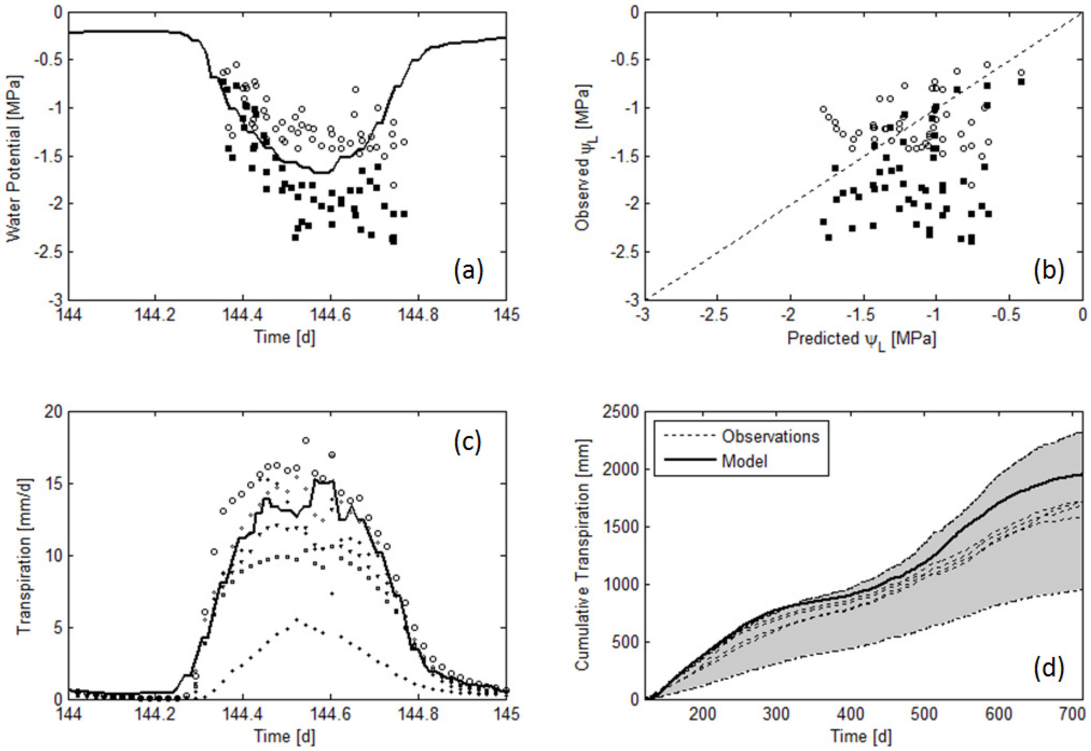

Figure 2.3: Tree transpiration dynamics: (a) modeled leaf water potential ψ_L and (c) tree transpiration during day 144 (year 2007). Leaf (■) and branch (○) water potentials measured on different days of year 2007 are also compared with modeled ψ_L in panel (b) and shown as reference in panel (a). Sap flow measurements from different trees are compared with modeled transpiration on day 144 (different symbols in panel c) and cumulative transpiration over year 2007 and 2008 (dashed lines in panel d).

surements is attributed to the choice of the initial pressure distribution (hydrostatic profile based on the observed water table), but the simulations adjusts after few rainfall events. Other discrepancies between model results and measurements are related to the occasional rapid transients in soil moisture within the deeper layers. These measured transients can be plausibly explained by small scale heterogeneities not accounted for in the model (e.g. preferential flow paths causing fast downward flow or presence of sand/clay lenses not included here). Some evidence that these small scale heterogeneities play a role can indeed be fingerprinted. For example, the peak in soil moisture observed at 1 m below the soil surface on day 305 (Fig. 2.2d) can be explained by the presence of preferential flows since this peak is not related to a water table fluctuation and is not observed in the upper soil layers (Fig. 2.2a-c). Not withstanding these deviations between model calculations and measurements, it can be surmised that the calibrated model behavior realistically reproduces the main processes impacting soil moisture dynamics in this system.

The ability of the model to describe the RWU mechanisms are shown in Fig. 2.3. The model captures the biotic behavior in terms of leaf water potential (Fig. 2.3a-b)

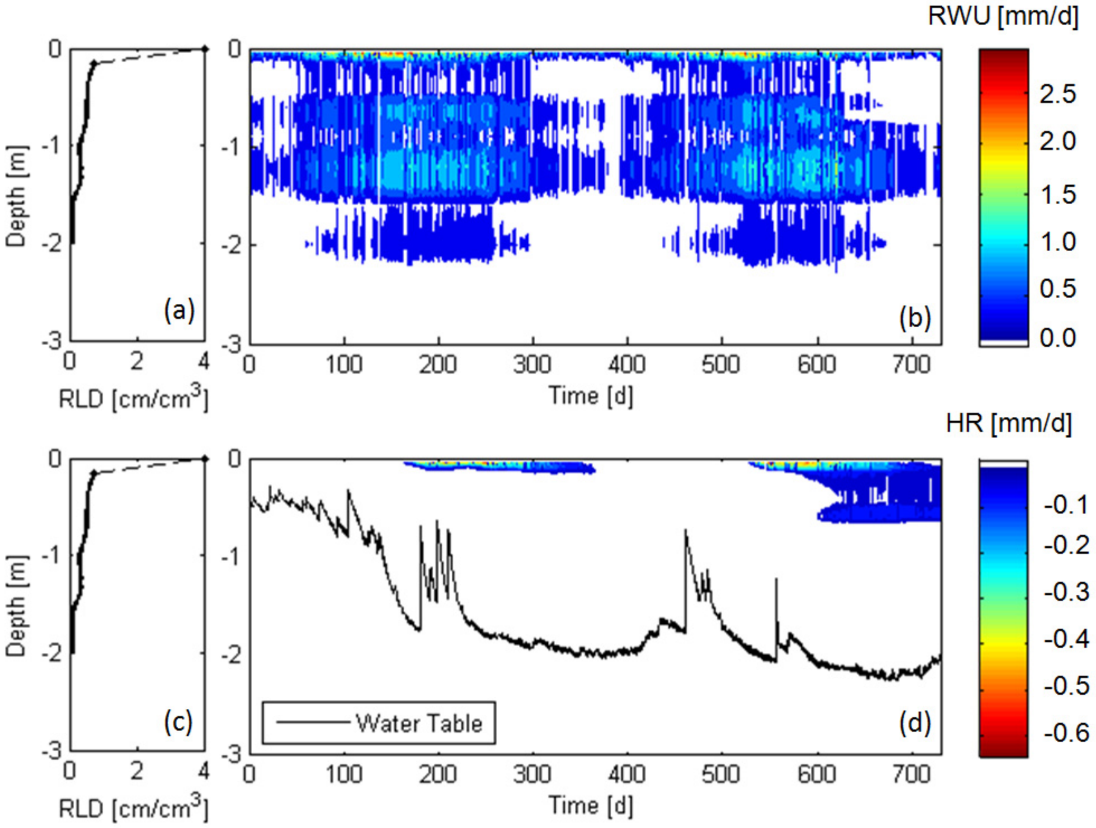

Figure 2.4: Observed root density profile (a,c), modeled RWU (b) and HR (d) during year 2007 and 2008 at different soil depths. The water table fluctuations are also shown (black line in panel b).

and transpiration (Fig. 2.3c-d). Because of the single-layer approximation for the above-ground leaf pressure, modeled ψ_L is compared with measurements from both leaf and branches, showing a reasonable match. The measured sap-flux (Fig. 2.3c) also shows large variability among different trees, but the model provides an adequate description of the mean value (Fig. 2.3c). The dynamics of RWU along the soil column during the two-years period is also illustrated in Fig. 2.4a. The RWU is higher during the summer periods as expected and it decreases during the winter despite the ever-green nature of this stand and the warm climate of NC. During dry periods, soil water is first redistributed by roots in the top soil, subsequently redistribution is more prominent in the deeper layers (Fig. 2.4b). In particular, HR is not high during the first year, as the water table is shallow, while it increases during the second year, due to a significant drop in the water table (Fig. 2.4b). The HR estimates span two order of magnitudes across ecosystems [Neumann and Cardon, 2012] and, as discussed elsewhere [Domec et al., 2010], it can mitigate the effects of soil drying on stand evapotranspiration and net primary productivity. In Loblolly pine plantations, reported estimates of HR can exceed 1 mm d^{-1}, ranging between 6-12% of daily transpiration [Domec et al., 2010]. The model here predicts a peak HR rate of 0.5 mm d^{-1} in 2007 and 1.1 mm d^{-1} in 2008 (i.e. 10-20% of daily

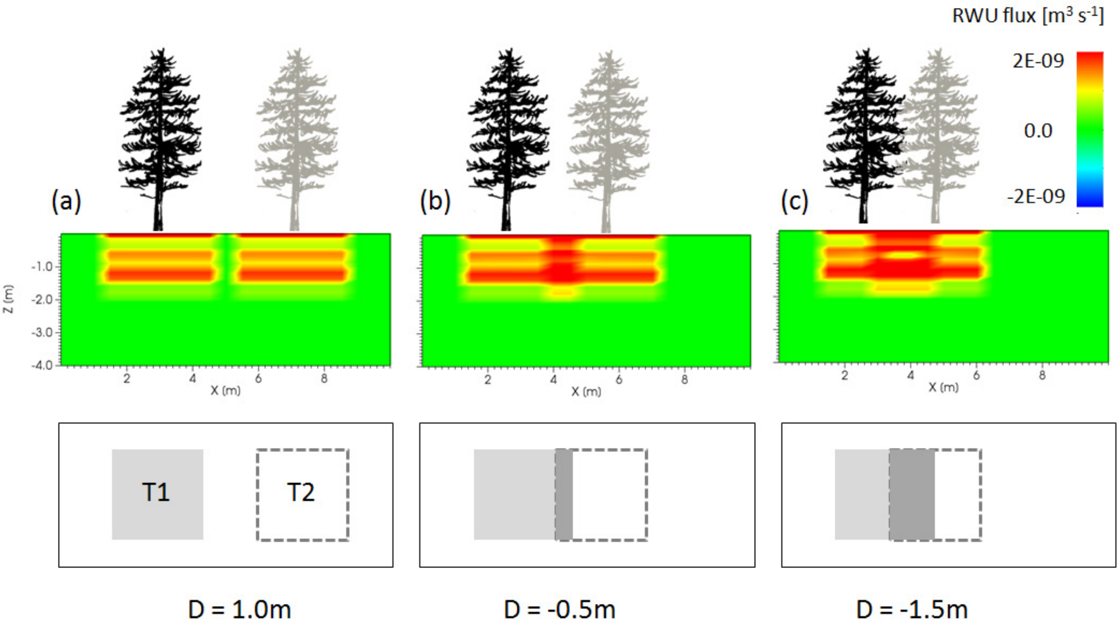

Figure 2.5: Simulation results of RWU by multiple trees. The RWU rates at time $t = 5.5$ days are shown for the test cases with different tree spacing: (a) $D = 1$m, (b) $D = -0.5$m, and (c) $D = -1.5$m.

transpiration), in agreement with the magnitude of HR observed at the site [Domec et al., 2012] and reported elsewhere in the literature [Neumann and Cardon, 2012].

2.5.2 Trees competition

Having demonstrated the model skills, a system of two identical trees (T1 and T2) with interacting roots is now considered so as to explore the effect of root water competition on RWU and photosynthesis. Each tree has a rooting system with a projected surface of 9 m^2 ($d_r = 1.5$ m). Configurations ranging from no interaction ($D = 1.0$ m) to progressively greater overlap ($D = -0.5$ m and $D = -1.5$ m, corresponding to overlaps of 17% and 50% of the projected area of a single root system) are now examined. In the overlap areas, the total RWU increases due to increased local root biomass (Fig. 2.5). An increased root overlap leads to an RWU vertical distribution that appears less localized within the root zone when compared to the biomass proportion allocated to each layer (the 'bumps' in Figure 2.4a). This reduced spatial localization in RWU away from the root density distribution is due to a proportionally greater uptake in the remaining layers, partly activated by the compensatory mechanisms (HR and Darcian redistribution). When the response of a single tree is considered (e.g. T1, as the responses are equal, due to symmetry), greater interaction among the rooting systems causes an earlier onset of HR and of water stress, with a corresponding decrease in RWU (Fig. 2.6a-b). This also results in a faster decline in leaf water potential and a corresponding increase of the cost parameter λ (Fig. 2.6c-d), causing rapid censoring of leaf transpiration.

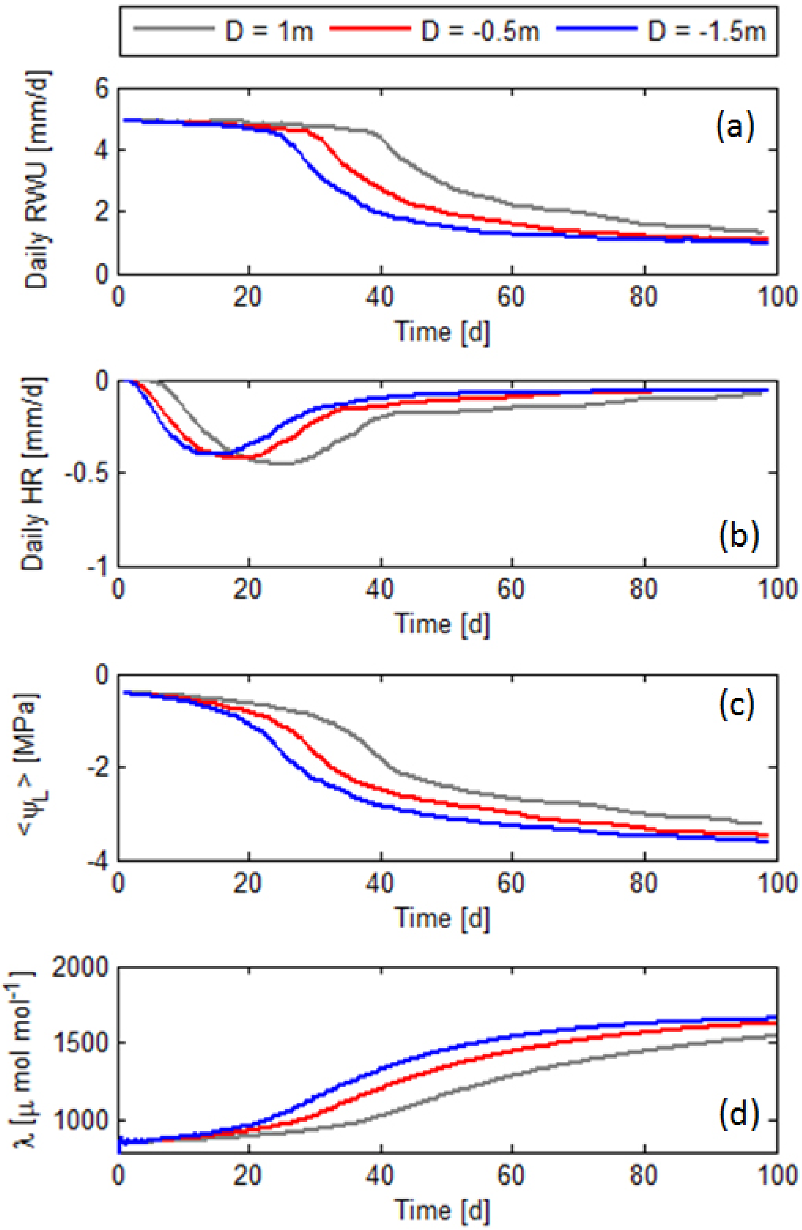

Figure 2.6: Transpiration dynamics of tree T1 for different spacings D: (a) daily RWU, (b) HR, (c) daily averaged ψ_L and λ are shown for the case of non-overlapping ($D = 1$m) and overlapping ($D = -0.5$m and $D = -1.5$m) root systems.

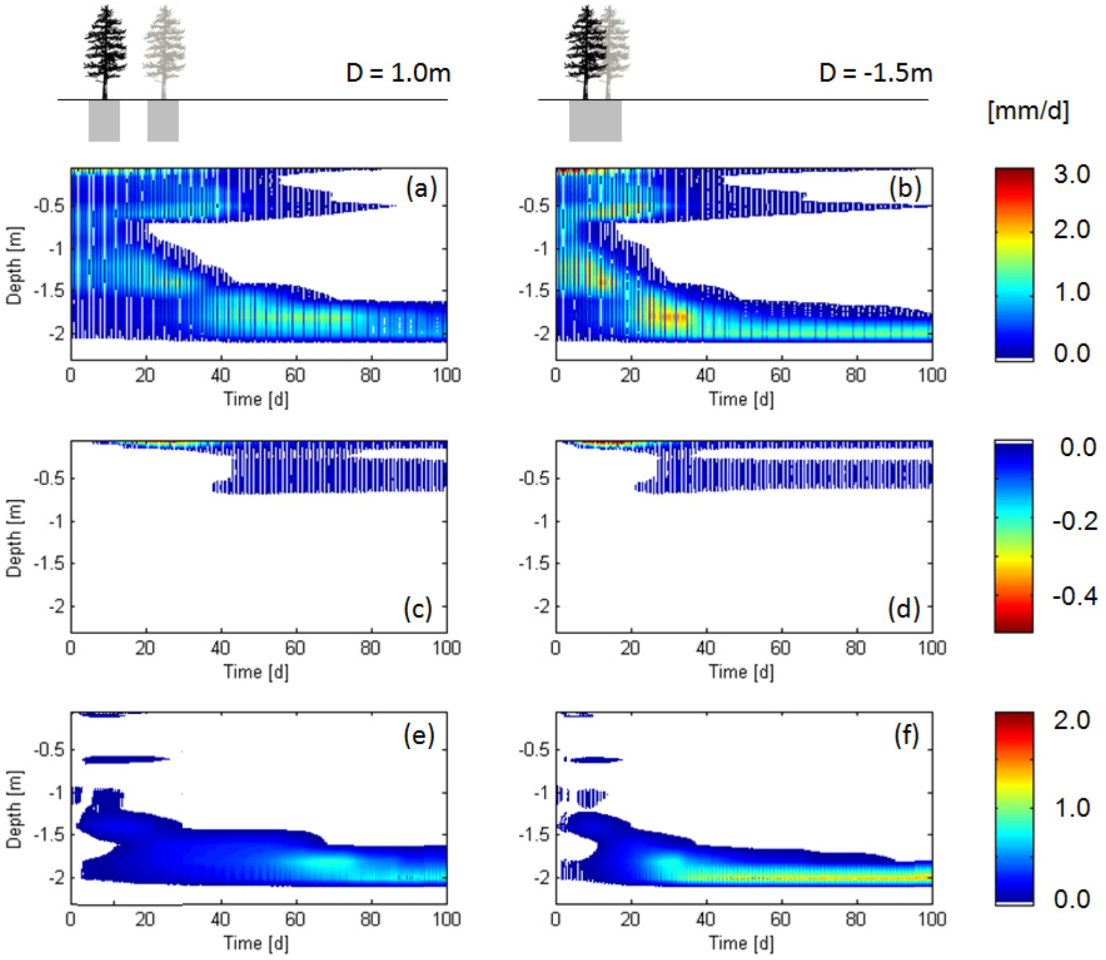

Figure 2.7: Water fluxes in the root zone of tree T1: modeled (a,b) RWU, (c,d) HR and (e,f) the Darcy flux divergence as a function of depth for the case $D = 1$m (left panels) and $D = -1.5$m (right panels).

The space-time distributions of water fluxes exchanged by one tree with the soil within its root zone also show some interesting patterns as the interaction between root systems is increased (Fig. 2.7). As noted earlier, the soil dries more rapidly when root competition for water is intensified, with a corresponding inhibition of RWU and a faster shift of the active uptake layer to greater depthes (Fig. 2.7a,b). The HR flux initially sustains RWU in the top soil layers (Fig. 2.7a,b), where redistribution by Darcy's flow is partially inhibited (Fig. 2.7c,d) by the low soil water saturation and the correspondingly low hydraulic conductivity. Darcian redistribution is, on the contrary, most effective in providing soil moisture within the deeper layers (Fig. 2.7e-f), where the largest proportion of RWU take place when most of the soil column has dried down. Overall, RWU is sustained by upward redistribution of water both through the roots (Fig. 2.7c-d) and through Darcian flow (Fig. 2.7e-f) but, as e.g. shown in Volpe et al. [2013], the Darcy flow accounts for the majority of the redistributed water. Also, it should be emphasized that HR and the Darcian redistribution act in concert within the root zone so as to mediate the spatial regions of reduced soil moisture.

The robustness of these patterns for different root density profile shapes and soil hydraulic properties have also been explored (results shown in the Appendix). Briefly, drying fronts with the same forcings and boundary conditions but with an exponentially distributed root biomass having the same total biomass ($B(z) = e^{a \cdot z + b}$, where a and b are parameters) were simulated. The same system behavior was further explored when the soil was assumed to be uniformly sand ($K_s = 10^{-4}$ m s^{-1}) or silt ($K_s = 10^{-7}$ m s^{-1}). Collectively, these simulation results robustly show the dominance of Darcian upward redistribution to sustain RWU when compared to root HR. The latter provides significant contribution only near the soil surface, and in the initial phase of the soil drying. When the top soil layer is dry, the hydraulic conductivity there rapidly becomes small thus suppressing further root HR: water potentially lifted by the root system cannot in this case infiltrate into the surrounding soil. A second robust feature is that Darcian redistribution tends to be concentrated in the deeper layers, where a greater mean soil saturation ensures relatively high values of soil hydraulic conductivity and allows significant amounts of water to be moved towards the lower boundary of the root zone. As expected, a more conductive soil (sand) produces a faster transition towards stressed plant conditions, but still induces a significant amount of water redistribution by Darcian flow (in the deeper rooting zone) and by the root system (in the upper layers at the initial stages of the drying experiment). In all cases, root competition more rapidly pushes the system to drier conditions and amplifies the importance of these two redistribution mechanisms to support RWU and carbon assimilation.

2.5.3 Transpiration and soil saturation

A 'macroscopic' relation between ET and the root-zone averaged saturation, $\bar{S}_w$, is often assumed in bulk ecosystem models seeking to capture the essential components of the soil-plant-atmosphere system [Eagleson, 1978, Laio et al., 2001, Milly, 1993, Porporato et al., 2004, Rodrguez-Iturbe et al., 1999b]. Typical bulk models are based on a water balance equation describing the change in soil saturation within the entire root-zone as a function of water infiltration (generally accounting for stochastic rainfall, canopy interception and run-off rates [Laio et al., 2001, Porporato et al., 2004, Rodrguez-Iturbe et al., 1999b]) and ET. The ET rate in this context is often defined as a fraction of a maximum evapotranspiration for the ecosystem [Laio et al., 2001, Rodrguez-Iturbe et al., 1999b] through a water stress function, ρ, which varies with $\bar{S}_w$: $ET(\bar{S}_w) = \rho(\bar{S}_w) \cdot ET_{max}$. The form of $\rho(\bar{S}_w)$ and the value of ET_{max} are usually assumed with reference to a zeroth-dimensional spatial framework in which the effects of competition among rooting systems cannot be accounted for. The 3D nature of the model here is used to investigate the implications of root competition on the dependence of RWU/transpiration on $\bar{S}_w$. To this end, we extract from the dry-down experiments corresponding values of ET and $\bar{S}_w$ to construct $ET(\bar{S}_w)$ curves for different root spacings D (Fig. 2.8a). The relation between ET and soil-moisture appears insensitive to D and that ET vs. $\rho(\bar{S}_w)$ curves collapse onto one another. That is, a unique function $\rho(\bar{S}_w)$ emerges even when tree spacing is altered (all else being the same). Irrespective of the D variations, hydraulic limitations to RWU

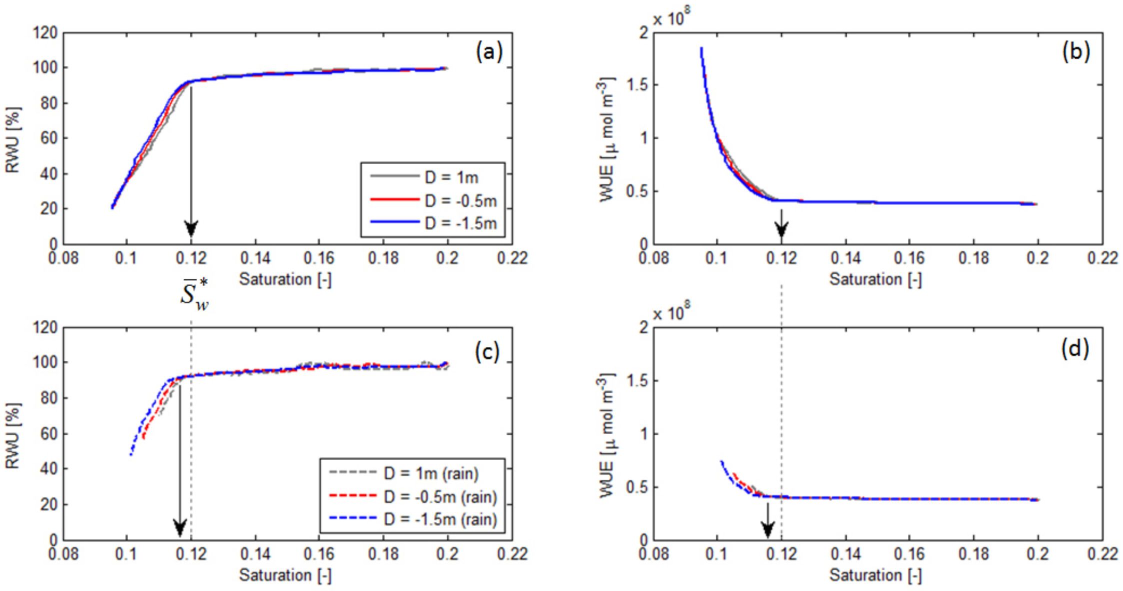

Figure 2.8: Transpiration and soil saturation: (a, c) relative RWU and (b, d) WUE as a function of average soil saturation within the root zone during the drying cycle with (top panels) and without (bottom panels) rainfall.

commence when soil saturation drops below the same critical value of approximately $\bar{S}_w^* = 0.12$. The difference among root spacing scenarios lies in the speed at which the system traverses through the function in Fig. 2.8a. In particular, for $D = 1.0$ m (no overlap), $D = -0.5$ m, and $D = -1.5$ m, the critical soil moisture value is reached after 39, 29, and 24 days, respectively. The mean rainfall inter-arrival time at the site (see Appendix) is generally lower than the time needed for the system to reach such stress conditions (around 90% of the rainfall events has an inter-arrival time $\leq$ 8 days). However, inter-arrival times of 18 days have been observed in 2007-2008, and the degree of root overlapping may play an important role in controlling the transition to stress conditions. Interestingly, the decrease in RWU corresponds to an increase in the Water Use Efficiency (WUE), defined as the ratio of the whole plant photosynthetic rate to the plant transpiration rate ($WUE = f_c/f_w$), which is also insensitive to D (Fig. 2.8b). To verify the robustness of this insensitivity of the stress response function to root competition, further simulations with different boundary conditions were run. In particular, the effect of rainfall is evaluated by running drainage experiments in which a constant rainfall is applied at the top of the domain. An infiltration rate of $1 mmd^{-1}$ was assumed so as to explore how the modified vertical soil moisture profile impacts the $\rho(\bar{S}_w)$ form. Precipitation changes the soil moisture profile with respect to the simple drainage experiment by increasing the available water in the top soil (where most of the root biomass is) thus slowing down the onset of water stress. The main finding is that rainfall shifts the critical value of the mean soil moisture, $\bar{S}_w^*$, towards drier states (Fig. 2.8c,d). Furthermore, the shift of the critical value for water stress does exibit a dependence on the amount of root overlap, albeit relatively mild. Comparable results are obtained from simulations with different soil properties (see Appendix). These results suggest the existence of a stress response function that is independent of the degree of root overlap under dry conditions, but is dependent on rainfall amount and frequency and, mainly, on soil hydraulic properties. Understanding how the soil saturation-RWU relation varies under different hydrological conditions and root biomass allocation strategies is a topic for future work.

2.6 Conclusions

A three-dimensional approach of the soil-plant system is presented and applied to model root water uptake by overlapping rooting systems of Loblolly pine trees. The approach couples Richard's equation for soil moisture redistribution with a mechanistic description of plant transpiration and leaf photosynthesis. The results show that overlapping root systems affect soil moisture dynamics, Darcian redistribution, and hydraulic redistribution. When the three-dimensional RWU is volume-averaged in space, the main effect of overlapping root systems is to induce rapidly the onset of water stress conditions. Averaged ET vs. mean soil moisture relations are relatively independent of the degree of root overlap under dry conditions, but depend on soil hydraulic properties and, to a lesser extent, on the amount of rainfall infiltration. Because the model provides a 3D representation of the processes regulating root water uptake, it can be used to explore inherently spatial effects such as the role of soil heterogeneities and root allocation strategies on RWU and carbon uptake.

3

Modeling and Monitoring Farmland Productivity

3.1 Summary

The southern portion of the Venice coastland is a very precarious environment and salt contamination of land and groundwater is a severe problem that is seriously impacting the farmland productivity. Geophysical surveys, lab testing and continuous monitoring of hydrological parameters together with crop yield distribution were performed and acquired from 2010 to 2012 in a 21 ha basin cultivated with maize crop and representative of the area. I this chapter the dataset is presented and used to set-up a numerical model of soil moisture dynamics coupled with plant transpiration, photosynthesis and growth. The model is applied to the field site to understand the impact of land elevation, soil heterogeneities, and seawater contamination on land productivity. The contents of this chapter has been published in the journal *Procedia Environmental Sciences*:

Manoli, G., Bonetti, S., Scudiero, E., Teatini, P., Binning, P. J., Morari, F., Putti, M., and Marani, M. (2013b). Monitoring and modeling farmland productivity along the venice coastland, Italy. Procedia Environ. Sci., 19:361-368.

3.2 Introduction

Saving water for agricultural activity is an old, but ongoing, challenge [Green et al., 2006, Srayeddin and Doussan, 2009] and a better understanding of the biophysical processes of root-water uptake is required to develop more sustainable irrigation practices. Additionally, saline water intrusion associated with sea level rise is adversely impacting agricultural production of coastal areas at an alarming rate [Green et al., 2006, Volpe et al., 2011]. The southern portion of the Venice coastland, Italy, represents a very precarious environment (Fig. 3.1). Due to an elevation down to 4 mbsl (Fig. 3.1c), the seawater intrusion from the Venice Lagoon and the encroachment of salty water from the mouth of the river network, salt contamination of land and groundwater is a severe problem that is seriously impacting the farmland productivity [Teatini et al., 2011]. Understanding the complex interactions between plant growth, root water uptake, atmospheric and soil dynamics under stressed conditions is therefore necessary to optimize land productivity while preserving water resources. Mathematical modeling has been successfully applied to support on-farm decision-making processes, but understanding and modeling the field scale soil-plant-atmosphere interactions is an open challenge [Jury et al., 2011]. Existing modeling approaches can be divided into two categories: 1) ecophysiological models accounting for detailed crop growth but lacking of a detailed description of water flow (typically a one-dimensional water balance) and 2) hydrological models describing plant water uptake as a sink term in the Richards equation but generally neglecting the feedback mechanisms with plant photosynthesis and growth. The most widely used ecophysiological models, e.g. WOFOST [Supit et al., 1994] and CERES [Ritchie, 1998], account for water dynamics using a simplified water budget over soil compartments with a fixed water-holding capacity. Other models, such as SWAP [van Dam et al., 1997], are Richards equation-based models but only vertical flow is considered thus limiting the model applicability at the field/watershed scale where soil heterogeneities and land elevation may play an important role on plant dynamics. On the other hand most of the existing multidimensional hydrological models account for root water uptake using simplified sink terms in the Richards equation (e.g. HYDRUS [Šimůnek et al., 2006]) but it is shown that the applicability of simplified macroscopic models is limited in heterogeneous media [Kuhlmann et al., 2012]. Recently Katul et al. [2010] presented a stomatal optimization theory to describe the effects of atmospheric CO2 on leaf photosynthesis and transpiration, further coupled with a one-dimensional model of soil moisture dynamics in [Volpe et al., 2013]. The modeling framework presented in [Volpe et al., 2013] is here extended to describe soil productivity at the field/watershed scale and quantify the factors of land degradation on the Venice coastland.

3.3 Case of Study

The study site (Fig. 3.1) is a 21 ha field located at the southern margins of the Lagoon of Venice, North-East of Italy, in proximity of the Brenta and Bacchiglione Rivers and approximately 7 km to the Adriatic Sea shoreline. The area is crossed by two well-preserved paleochannels (visible from satellite images as shown in Fig. 3.1b) that could potentially connect the study site to the Lagoon, or to the above-mentioned rivers. In spring 2012 a micro elevation survey was carried out with the Trimble FM 1000 CNH (Trimble Navigation Ltd., USA) real time kinematic system. The survey showed that the study site lies in the range of ca. -1.5 to -3.3 m below average sea level and the paleochannels are generally higher than the neighboring zones (Fig. 3.1c). Both undisturbed and disturbed soil samples were collected in May 2010 at different depths: disturbed samples were analyzed for soil electrical conductivity ($EC_{1:2}$, dS m-1) and soil texture (%) using a laser particle size analyser while undisturbed cores were analysed for soil bulk density and saturated/unsaturated hydraulic conductivity [Scudiero et al., 2011]. The site characterization is illustrated

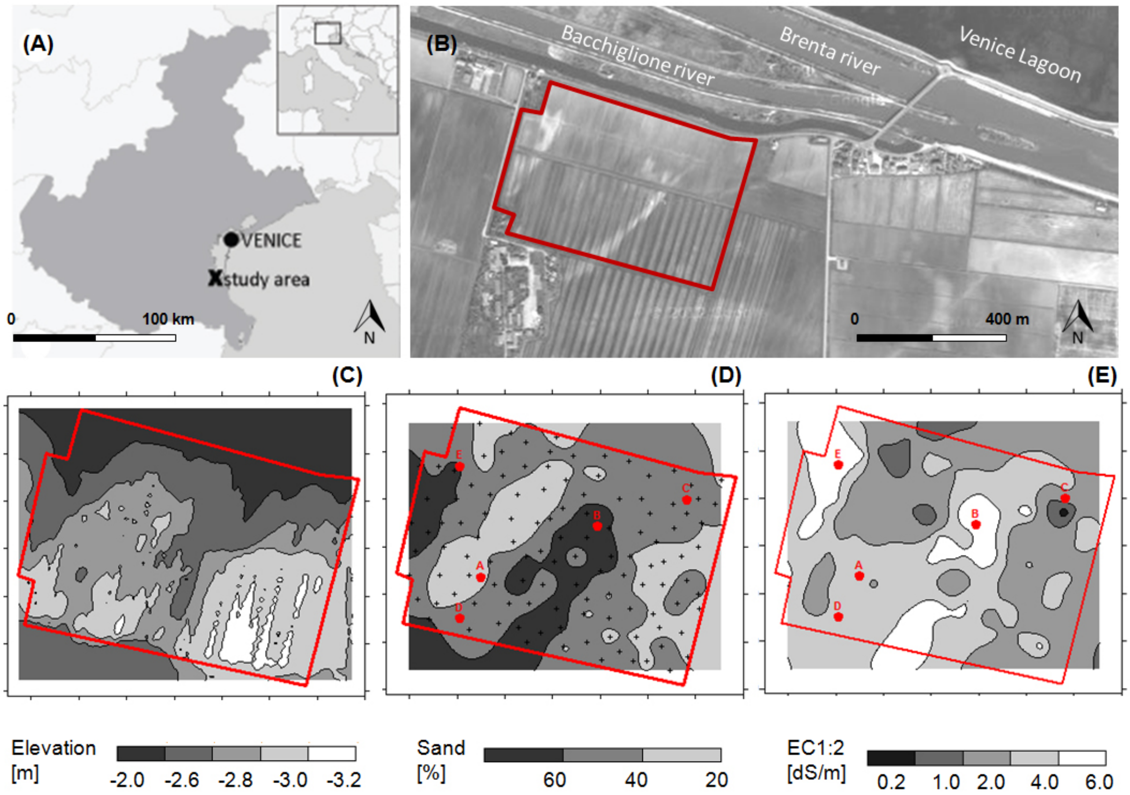

Figure 3.1: . Study area: (a) location with respect to the Venice Lagoon and (b) the crop field. Site characterization: (c) land elevation, (d) soil texture (as sand percentage) and (e) soil salinity (as $EC_{1:2}$). Red dots represent the monitoring stations at the site.

in Fig. 3.1c-e. The field was cropped with maize (*Zea mais L.*) and harvested for grain. Maize grain yield was measured with a combine harvester equipped with a yield monitor (Agrocom, Claas, Germany) and a DGPS.

3.4 Mathematical formulation

3.4.1 Model description

SPA model. The model used in this study makes the following assumptions: a) water extracted by roots is instantaneously transpired by leaves and no water storage can occur within the plant, b) each soil layer is directly linked to the xylem by the root biomass allocated in the layer, and c) the model is applied to maize assuming ample supply of nutrients, and without pests, diseases and weeds. Soil moisture dynamics is described by the three-dimensional Richards equation (see Chapter 2). Plant uptake is described by the Ohm's law type model developed in 2 and schematized in Fig. 3.2a. The transpiration flux is modeled in terms of water potentials in the leaf (ψ_L), in the xylem (ψ_R) and in the soil (ψ_i).

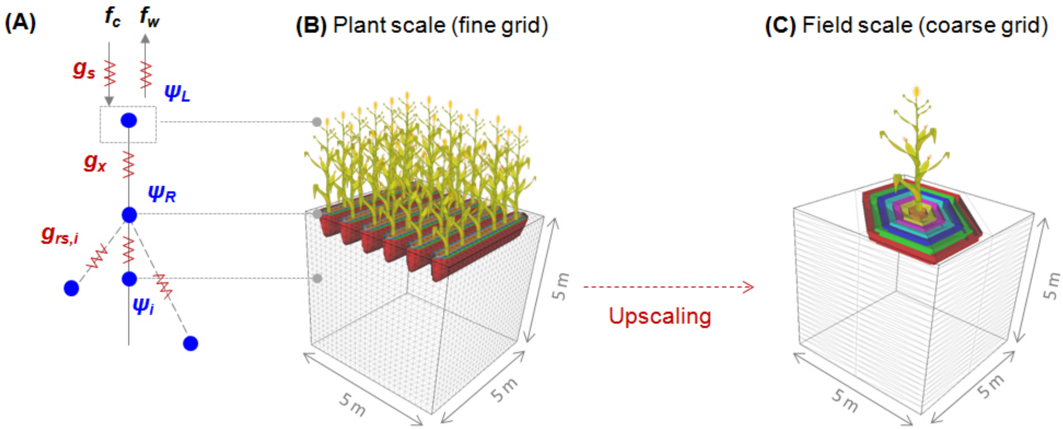

Figure 3.2: Conceptual model (a) and simulation grids: plant scale (b) and field scale (c) model grid.

Crop growth. Carbon assimilation by plant j is described by a biochemical photosynthesis model Farquhar et al. [1980]:

$$f_{c,j} = \frac{a_1}{a_2 + c_i}(c_i - c_p) \tag{3.1}$$

where c_p is the CO_2 compensation point [mmol μmol^{-1}] and the inter-cellular CO_2 concentration c_i is estimated assuming Fickian Mass transfer between the leaf and the atmosphere [Volpe et al., 2013]. The absorbed CO2 is reduced to carbohydrates (CH2O) using the energy supplied by the absorbed light. The carbon flux $f_{c,j}$ is used to calculate the dry matter accumulation based on respiration costs (R) and carbohydrates allocation in the different plant organs (i.e. leaves, stems, roots and storage organs). Dry matter accumulation and partitioning is based on the simulation model for crop growth SUCROS [van Laar et al., 1997]. The accumulation of dry matter in the plant organ k is calculated as follows:

$$w_{k,j}(t) = w_{k,j}(t_0) \int_{t_0}^{t} \alpha_k(t) \cdot (f_{c,j} - R_j) \cdot dt \tag{3.2}$$

where $w_{k,j}(t_0)$ is the initial biomass (at seeding), R_j is the respiration cost and the allocation coefficients α_k depend on the phenological development stage of the crop, which varies between zero at seeding and 2 at maturity. The Leaf Area Index (LAI_j) depends on the rate of growth and senescence of leaves which varies with the development stage of the crop. We refer van Laar et al. [1997] for further details on the crop growth processes. The plant parameters varying with growth are adjusted according to Ref. For Example, the canopy height is defined as:

$$h_{c,j}(t) = h_{cmax,j} \cdot \sqrt{\frac{LAI_j(t)}{LAI_{max,j}}} \tag{3.3}$$

Salt toxicity. According to [Volpe et al., 2011], the parameters a_1 and λ are identified as most significantly controlling the behavior of the linear optimality model under salt-stress condition. Since the water use efficiency λ is a function of the leaf water potential (and it is not an independent parameter as in [Volpe et al., 2011]), salinity is here assumed to affect only the photosynthetic efficiency $a_1 = a_{1,max} \cdot \tau(EC)$ where τ is an empirical salinity response curve defined as [van Genuchten and Hoffman, 1984]:

$$\tau(EC) = \begin{cases} 1 & \text{if } 0 \leq EC \leq EC_{limit} \\ 1 - s \cdot (EC - EC_{limit}) & \text{if } EC > EC_{limit} \end{cases} \tag{3.4}$$

where s and EC_{limit} are fitting parameters. This means any salt-stress is here interpreted as impacting the photosynthetic efficiency of the plant [Volpe et al., 2011] neglecting other possible impacts (e.g. on water use efficiency, soil-root conductances, osmotic pressure, etc.). However, according to the modeling framework presented herein, an inhibition of the photosynthetic efficiency a_1 implicitly influences the water use efficiency (see model description in Chapter 2).

3.4.2 Model setup

The model is calibrated on a single plant and then applied at the plot scale to obtain a sort of upscaled version of the plant model. The procedure is schematized in Fig. 3.2 and will be described with more details in the next section. Given the model resolution and considering that our interest lies in the simulation of the long term crop productivity, the temporal dynamics of salt concentration in the vadose zone is neglected and assumed equal to the measured soil salinity (Fig. 3.1e). This assumption is further justified by the steady state condition reached by the farmland-lagoon system. The limited variability in time of salt concentration has been confirmed also by repeated electro-magnetic surveys covering the whole basin and continuous records of groundwater conductivity in a number of piezometers drilled for the purpose.

3.5 Results and discussion

Calibration and upscaling proceeds as follows. A first set of simulations has been performed to calibrate the model parameters at the plant scale. A cubic portion of soil of dimensions 5×5×5m (subsequently called the plot) is discretized in the x- and y-directions with a 0.2 m spacing (fine grid) allowing a detailed description of 132 plants, i.e. the typical number of plants seeded in a 5×5 m plot (Fig. 3.1b). The upscaled model is then obtained by calibration of the model parameters on the same plot discretized with a coarse grid (2.5m spacing in x and y) where a single plant is used to represent the behavior of the whole fine-scale plot. Calibration is considered achieved when the fluxes in the coarse single-plant plot equal the fluxes in the fine scale plot. The coarse grid corresponds to the volume related to a node of the field scale model. All the plant uptake model parameters used at the plant scale are based on literature values and field observations and only

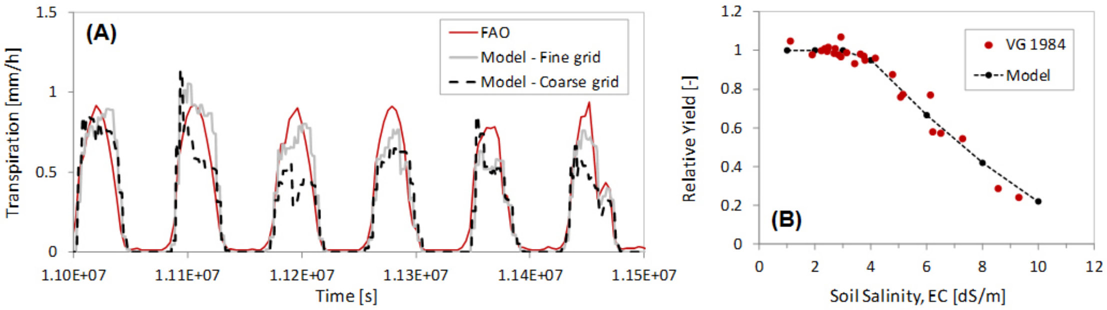

Figure 3.3: Calibration of the transpiration flux (a) and the effect of soil salinity on crop yield (b): model results are compared with experimental data from [van Genuchten and Hoffman, 1984] (VG 1984).

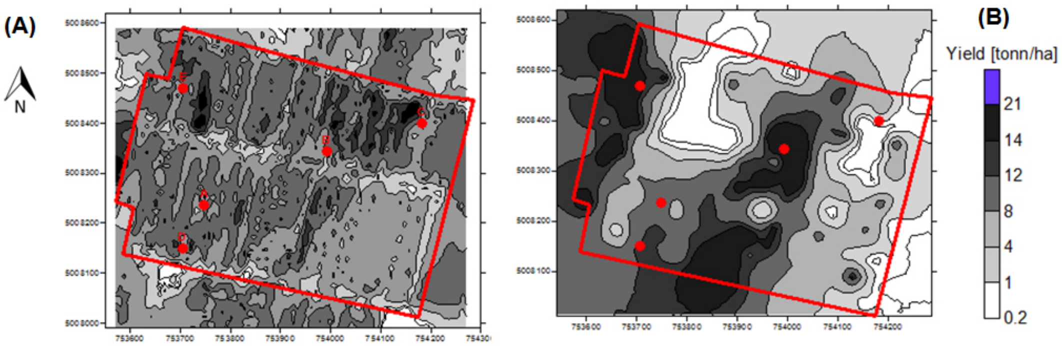

Figure 3.4: Observed (a) and simulated (b) crop yield at harvesting for year 2011. Data provided by [Braga et al., 2012].

the parameters related to the plant dimensions (roots lengths, canopy area, etc.) are modified in the upscaling procedure. Field data (rainfall, temperature, relative humidity, radiation) are used to calculate the atmospheric forcing. Input evaporation is considered as a potential rate, and actual evaporation is evaluated based on system state condition allowing the switching between Neumann and Dirichlet boundary conditions [Camporese et al., 2010]. Since measurements of transpiration fluxes are not available at the site, simulation results are compared with the potential transpiration calculated by the Penmann-Monteith equation (FAO) using the dual-crop coefficient approach [Allen et al., 1998]. For this purpose, the simulations were run ensuring well-watered conditions. The upscaled plot model is shown to capture the expected dynamics (Fig. 3.3a). Notice that a perfect match with the potential transpiration by FAO is considered beyond the objectives of this study. To test the response of plant growth to soil salinity, different simulations were run with increasing values of soil salinity. The predicted relative yield is compared with experimental data published in [van Genuchten and Hoffman, 1984] and the model shows a good agreement with data (Fig. 3.3b). The model is then applied at the field scale, over a 600×600×5m model domain (red square in Fig. 3.1b) to predict the farmland productivity. The surface elevation was built using the micro elevation survey data and the observed soil salinity (Fig. 3.1e) was interpolated over the model grid by kriging. Water table levels are specified for the Northern and Southern boundaries of the model domain according to the observed water level in the irrigation channels. No flow boundary conditions are set on the other edges of the domain. Preliminary results for year 2011 are shown in Fig. 3.4. The model is shown to capture the measured crop productivity even if the spatial pattern observed at the small scale is poorly matched. Moreover, model results show that salt stress is the major cause of crop stress and the sandy regions are the most productive (Fig. 3.4b) as confirmed by the field observations (Fig. 3.4a).

3.6 Conclusions

We have used a Richards equation model coupled to plant dynamics to simulate the spatially distributed maize production on a 21 ha instrumented field on the boundary of the Venice Lagoon (Italy). We assumed that no limitation on crop production was due to nutrient scarcity, while the effect of soil salinity was taken in full consideration. This study is a preliminary application of the model developed and a perfect match between simulation results and field observations was beyond the objectives of this work. The aim was to obtain reasonable estimations of crop yield using literature values of the model parameters and investigate the ability of a fully coupled soil-plant model to predict the spatial variability of land productivity. Simulation results are in the same range of the precision agriculture measurements but the model was not able to capture all the fine scale spatial variability of the observed vegetation patterns. The discrepancy between observations and simulations are to be attributed mainly to neglected fine scale hydrologic constraints, such as the presence of the ditch network used to keep drained the farmland, and physical processes (e.g., nutrient uptake, salt temporal dynamics, etc.). Future work will be aimed at incorporating these features in order to proper calibrate and validate the model against hydrological records (e.g., groundwater levels, soil moisture content, etc.), crop growth and yield data collected at the site.

4

Modeling Convective Rainfall Initiation

4.1 Summary

A mechanistic model for the soil-plant-atmosphere (SPA) system is coupled with a slab representation of the atmospheric boundary layer (ABL) to explore the role of water table fluctuations and free atmospheric (FA) states on predisposition of convective rainfall (CR). The crossing of modeled lifting condensation level and ABL height is interpreted as a necessary (but not sufficient) condition for the predisposition of CR. If the feedback between surface fluxes and FA conditions is neglected, a reduction in latent heat flux associated with reduced water table levels is shown to enhance the predisposition to CR. However, when the SPA system is coupled with the ABL dynamics as well as atmospheric temperature and water vapor concentration budgets, FA conditions have a larger impact on rainfall initiation than water table fluctuations. Plant stress plays a role within a limited range of atmospheric parameters, and a decrease in latent heat flux leads to a suppression of boundary layer clouds. The contents of this chapter has been submitted for publication to the journal *Geophysical Research Letters*:

Bonetti, S., **Manoli, G.**, Domec, J. C., Putti, M., Marani, M., and Katul, G. (2013). The role of water table fluctuations and the free atmospheric state on convective rainfall initiation. *Submitted.*

4.2 Introduction

The link between root-zone soil moisture content, land surface fluxes of sensible (H_s) and latent heat (LE), and cloud formation continues to attract significant attention in the climate, atmospheric, hydrological and ecological communities [e.g., de Arellano et al., 2012, Katul et al., 2012, Koster et al., 2004, Santanello et al., 2007]. In particular, the indirect effects of plants on convective rainfall (CR) initiation remains illusive given the large number of interacting biotic and abiotic processes within the soil-plant-atmosphere (SPA) system. The dynamics of H_s and LE and the soil-plant-atmospheric state variables, which are regulated by root-zone soil moisture states, control the diurnal variation of convective ABL height and lifting condensation level (LCL) and thus their crossing [Siqueira et al., 2009]. This crossing is a necessary but not sufficient condition for the predisposition to rainfall [Juang et al., 2007, Siqueira et al., 2009]. Previous studies considered the effects of soil moisture on boundary layer dynamics under prescribed free atmospheric (FA) forcing [e.g., Koster et al., 2004, Maxwell et al., 2007], showing that below-ground processes can impact CR initiation. Other studies focused instead on FA feedbacks on CR with simplified soil moisture conditions [e.g., Clark and Arritt, 1995, daRocha et al., 1996, Findell, 2003, Konings et al., 2010, Siqueira et al., 2009]. However, the interplay between water table (WT) fluctuations and predisposition to CR under different FA conditions continues to resist complete theoretical treatment, and frames the compass of this work. The basic premise is that WT reductions increase H_s by diminishing the supply of water to the root-plant system. This WT reduction leads to an increase in the convective ABL height thereby enhancing the ABL-LCL crossing likelihood. On the other hand, WT reductions also diminish the water vapor source within the ABL because of reduced LE, thereby increasing the LCL and reducing the ABL-LCL crossing likelihood. This reduced water vapor source within the ABL may be mediated by the FA if sufficient water vapor is entrained from the ABL top or enters laterally through moisture convergence. These two competing effects suggest that in a soil-plant-atmosphere system where WT and FA water vapor entrainment are the main sources of water, there exists a rain/no-rain transition such that at a given WT level, FA water vapor entrainment must exceed a minimum threshold to ensure an ABL-LCL crossing. The objective of this work is illustrate the existence and the prototypical shape of such a threshold via simulations and field measurements.

4.3 Mathematical Methods

A conceptual model of the SPA system is illustrated in Fig. 4.1. The modeling approach is briefly presented but detailed descriptions of the model equations and parameters are provided in the Appendix.

4.3.1 Soil-Plant model

The SPA system (Fig. 4.1a) is modeled by water potential gradients in the soil (ψ_i), plant trunk (ψ_R) and leaf (ψ_L) and nonlinear conductivities that vary with the water potentials of each compartment [Manoli et al., 2013a]. Soil moisture dynamics is described using a three-dimensional Richards equation modified to include a 3-D root water uptake (RWU) defined by a local macroscopic sink term. The soil-plant hydraulic model is then linked to the atmosphere by a biochemical model of photosynthesis, where light attenuation is resolved across various canopy layers and the stomatal conductance g_s of each layer is optimized for maximum carbon gain at a given water loss via a marginal water use efficiency [Volpe et al., 2013]. The derivation of g_s includes Fickian mass transfer of CO_2 (f_c) and H_2O (f_w) through stomatal pores and a biochemical model of photosynthesis modified to include the

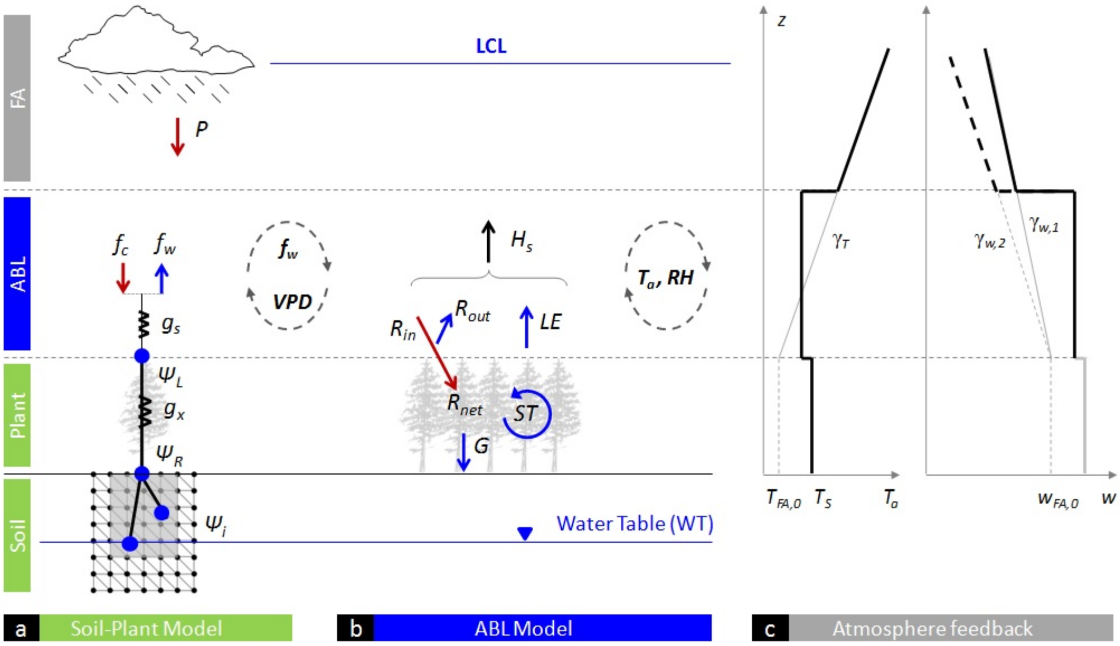

Figure 4.1: Conceptual Model: the soil-plant system (a), is modeled in terms of water potential in the soil (ψ_i), plant trunk (ψ_R) and plant leaf (ψ_L) through a series of conductactances (e.g. trunk xylem, g_x, and stomata, g_s). The hydraulic model is linked to the atmosphere by transpiration flux f_w, carbon assimilation f_c and VPD. The ABL model is based on a 1-D energy balance (b) and the atmospheric feedback (c) is included by considering the evolution of ABL temperature (T_a) and humidity (w) as described in the Appendix.

effects of water stress via a marginal water use efficiency [Katul et al., 2010, Volpe et al., 2013]. The transpiration flux f_w from the soil through the plant into the atmosphere is driven by a time-integrated leaf water potential ψ_L, which is controlled by both local soil moisture and atmospheric forcings (e.g the vapor pressure deficit, VPD).

4.3.2 Atmospheric Model

4.3.2.1 LCL Model

The lifting condensation layer (LCL) height z_{LCL} is determined from Juang et al. [2007]:

$$z_{LCL} = \frac{RT_a}{gM_a} \ln\left(\frac{P_s}{P_{LCL}}\right) \tag{4.1}$$

where $R = 8.314$ [J mol^{-1} K] is the universal gas constant, T_a is the mean air temperature [K], g is the gravitational acceleration [m s^{-2}], M_a is the molecular weight of air ($\sim$ 29 g mol^{-1}), P_s [kPa] is the atmospheric pressure at the canopy surface, and P_{LCL} [kPa] is the atmospheric pressure at z_{LCL}. The value of P_{LCL} can be written as Juang et al. [2007]:

$$P_{LCL} = P_s \left(\frac{T_{LCL}}{T_a} \right)^{3.5} \tag{4.2}$$

where T_{LCL} [K] is the saturation point temperature at z_{LCL}, which can be derived from the Clausius-Clapeyron equation Juang et al. [2007]:

$$T_{LCL} = \frac{2840}{3.5 \cdot \ln\left(T_a\right) - \ln\left(\frac{rP_s}{0.622+r}\right) - 7.108} + 55 \tag{4.3}$$

where the parameter 3.5 is the inverse of the Poisson constant for air and r is the near-surface atmospheric water vapor mixing ratio, determined by **?** as:

$$r = 0.622 \cdot \frac{e_a(T_a)}{P_s - e_a(T_a)} \tag{4.4}$$

where the actual vapor pressure e_a [kPa] is calculated as $e_a = e_s \cdot RH/100$, being RH [%] the relative humidity of the air and e_s [kPa] the saturation vapor pressure, given by the Clausius-Clapeyron relation:

$$e_s\left(T\right) = 0.6108 \cdot \exp\left(\frac{17.27 \cdot (T - 273.15)}{(T - 273.15) + 237.3} \right) \tag{4.5}$$

where T [K] is the temperature.

4.3.2.2 ABL Model

The dynamic of the Atmospheric Boundary Layer (ABL) height z_{ABL} is defined as:

$$\frac{dz_{ABL}}{dt} = \frac{H_s \cdot (1+\beta)}{\gamma_T \cdot z_{ABL}} \tag{4.6}$$

where γ_T is set to the temperature lapse rate (estimated equal to 5 K km^{-1} from sounding data at MHX airport using a linear regression analysis) and H_s is the surface sensible heat flux (described later). According to Tennekes [1973], the sensible heat flux entrained from the top of the mixed layer is a constant fraction β of H_s. Numerical and experimental studies **??** suggest β varies between 0.2 and 0.4. Here, we set β=0.2 to match ABL dynamics with field observations (see next section).

Energy balance The sensible heat flux H_s [K m s^{-1}] is calculated from the energy balance at the canopy top:

$$H_s\left(T_s\right) = \frac{1}{c_p \cdot \rho_a} \left[R_n\left(T_s\right) - LE - G - ST\right] \tag{4.7}$$

where T_s [K] is the canopy skin temperature, $LE = \lambda \cdot \rho_w \cdot f_w \cdot A_c^{-1}$ is the latent heat flux [W m^{-2}] with λ = 44000 J mol^{-1} being the latent heat of vaporization, c_p = 1005 J kg^{-1} K^{-1} is the specific heat capacity of dry air at constant pressure, ρ_a and ρ_w [kg m^{-3}] are the air and water density, respectively. The soil heat flux

G [W m^{-2}] is based on field data and the storage of heat within the canopy ST [W m^{-2}] is assumed to be 5% of the net radiation R_n. The net radiation R_n [W m^{-2}] is calculated as $R_n = R_{ns} - R_{nl}$, where R_{ns} and R_{nl} are the net shortwave and longwave radiation at the canopy top, respectively. The net shortwave radiation is calculated as $R_{ns} = (1-\alpha) \cdot R_s$ being R_s the incoming shortwave radiation measured above the canopy and α is the canopy albedo (estimated from measured outgoing shortwave radiation). The net longwave radiation is calculated according to the Stefan-Boltzmann's law:

$$R_{nl}(T_s) = \sigma \left[\varepsilon_s T_s^4 - \varepsilon_a T_a^4\right] \tag{4.8}$$

where $\sigma = 5.67 \cdot 10^{-8}$ [W K^{-4} m^{-2}] is the Stefan-Boltzmann constant and ε_s [-] is the canopy surface emissivity that varies between 0.8 and 1.0 **?**. In this study, it is assumed that $\varepsilon_s = 0.9$, as commonly done in many other models **?**. The emissivity of the clear-sky atmosphere ε_a [-] is calculated according to Brutsaert [1975]:

$$\varepsilon_a = 1.24 \cdot \left(\frac{e_s(T_a) \cdot \frac{RH}{100}}{T_a}\right)^{\frac{1}{7}}. \tag{4.9}$$

Aerodynamic balance The sensible heat flux between the canopy surface and the atmosphere can be expressed as:

$$H_s(T_s) = g_a(T_s - T_a) \tag{4.10}$$

where $g_a = 1/r_a$, being r_a [s/m] the aerodynamic resistance, calculated as **?**:

$$r_a = \frac{ln\left[\frac{z_m - d}{z_{om}}\right] \cdot ln\left[\frac{z_h - d}{z_{oh}}\right]}{k^2 \cdot u_z} \tag{4.11}$$

where z_m is the height of wind speed measurements [m], z_h is the height of humidity measurements [m], $d = 2/3\ h_c$ is the zero-plane displacement height [m], $z_{om} = 0.123\ h_c$ is the roughness length governing the momentum transfer [m], $z_{oh} = 0.1\ z_{om}$ is the roughness length governing transfer of heat and vapor [m], $k = 0.41$ [-] is the von Karman's constant and u_z is the wind speed [m/s] at height z above the ground.

Non-linear closure equation Equating Eq.(4.7) and Eq.(4.10) provides a non-linear equation for the unknown T_s:

$$H(T_s) = g_a \cdot (T_s - T_a) - \frac{1}{c_p \cdot \rho_a} \cdot [R_n(T_s) - LE - G - ST] = 0 \tag{4.12}$$

which can be solved iteratively by the Newton-Raphson method. Eq.(4.12) is a 4^{th} order polynomial with four real solutions. To ensure the convergence of the numerical procedure to a correct value of T_s, the air temperature T_a is used as initial guess of the Newton iteration (i.e. $T_s(0) = T_a$). Eq.(4.6) is solved numerically by the forward Euler scheme. As the simulations require a continuous ABL height, a Nocturnal Boundary Layer (NBL) must also be included. A stationary NBL height

z_{night} = 100 m is imposed Siqueira et al. [2009], ?. This height is constant as long as nocturnal conditions prevail, and serves as the initial condition for daytime conditions. The transition from day-to-night is also abrupt, with the ABL height dropping from its near maximum value to z_{night} when the sensible heat flux at the surfaces switches from being positive to negative.

4.3.2.3 Soil-Plant-ABL coupling

The Soil-Plant model is coupled with the atmosphere via the calculation of the stomatal conductance g_s:

$$g_s(\psi_L) = \frac{a_1}{a_2 + s\ c_a}\left[-1 + \left(\frac{c_a}{a\ \lambda(\psi_L)\ VPD}\right)^{1/2}\right] + g_{s,n} \tag{4.13}$$

where s is a model constant, c_a [mmol mol^{-1}] is the CO_2 concentration in the atmosphere and the cost parameter λ [μmol mol^{-1}], i.e. the cost of water for the plant to complete the photosynthesis, is estimated from the leaf water potential according to Manzoni et al. [2011]. The nocturnal stomatal conductance $g_{s,n}$ is determined from the relation between sapflow and VPD ?. Given the canopy temperature T_s, it is possible to define the vapor pressure deficit (VPD) as a function of leaf vapor pressure and vapor pressure at ambient conditions:

$$VPD = e_s\left(T_s\right) - e_s\left(T_a\right) \cdot \frac{RH}{100} \tag{4.14}$$

The soil-plant-atmosphere continuum is thus fully coupled.

4.3.2.4 Atmosphere feedback

To describe the simultaneous effects of surface fluxes and free Atmosphere (FA) conditions on ABL and LCL dynamics, a well mixed ABL is assumed and the conservation equations for ABL potential temperature T_a and specific humidity w are employed as follows:

$$z_{ABL}\frac{dT_a}{dt} = H_s + (T_{FA} - T_a) \cdot \frac{dz_{ABL}}{dt} \tag{4.15}$$

$$z_{ABL}\frac{dw}{dt} = \frac{LE}{\rho_a \lambda} + (w_{FA} - w) \cdot \frac{dz_{ABL}}{dt} \tag{4.16}$$

where T_{FA} and w_{FA} are the potential temperature and humidity in the FA above z_{ABL}. Assuming a linear profile of T_{FA} and w_{FA} in the free atmosphere it directly follows that:

$$T_{FA} = T_{FA,0} + \gamma_T \cdot z_{ABL} \tag{4.17}$$

$$w_{FA} = w_{FA,0} + \gamma_w \cdot z_{ABL} \tag{4.18}$$

where $T_{FA,0} = 288$ [K] and $w_{FA,0} = 7.58 \times 10^{-3}$ [kg kg^{-1}] according to ?. Relative Humidity is then calculated as $RH = 100 \cdot w/w_s$, where $w_s = 0.622 \cdot e_s(T_a)/(P_a - e_s(T_a))$ is the specific humidity at saturation [kg kg^{-1}]. Modeled T_a and RH are then coupled with the previously described SPA model, thus providing a fully coupled description of the ABL-FA structure.

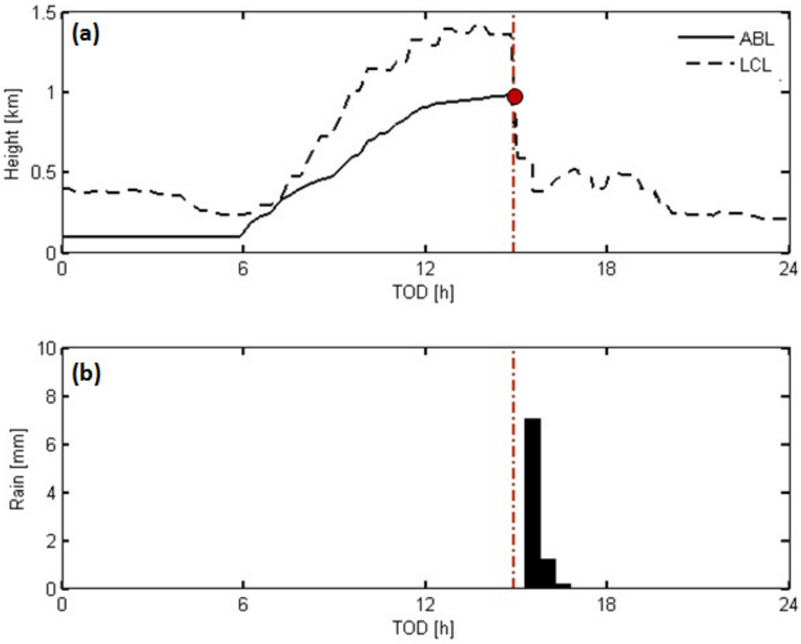

Figure 4.2: Modeled ABL and LCL heights (a), predicted rainfall event timing (ABL - LCL crossing defined by the red dot in panel a) and corresponding measured precipitation on day 176 of year 2007 (b).

4.3.3 Model Runs

First, the model is applied to a study area where the rooting system is sufficiently deep, WT fluctuations are large, and summertime rainfall is primarily convective. The site is a Loblolly pine (*Pinus taeda L.*) plantation in the lower coastal plain of North Carolina, USA (US-NC2 in the Ameriflux database). The study area and the data collected are described elsewhere [Sun et al., 2010]. Two sets of model runs are conducted. The first uses measured T_a and RH as input. By prescribing T_a and RH from measurements, the z_{LCL} time variations are prescribed and the predisposition to CR is primarily controlled by ABL dynamics only. That is, the ABL T_a and RH are independent from changes in H_s and LE within the model runs. The second set of model runs considers the simultaneous effects of H_s, LE and FA conditions on z_{ABL} and z_{LCL} dynamics. In these model runs, the depth-averaged T_a and RH within the ABL are computed (Fig. 4.1c).

4.4 Convective rainfall initiation

The model described above was parameterized for the pine plantation case of study. The soil-plant component was recently evaluated [Manoli et al., 2013a] while the ABL model is applied here to predict the predisposition of CR events between January 2007 and December 2008. Model results show good agreement with measurements (see Fig. S1 in the Appendix). In particular, net radiation is well matched: the correlation coefficient between modeled and measured R_n is 0.99 with the slope of the least-squares regression line equal to 0.99 and intercept -5.99 W m^{-2}. On the other hand, some discrepancies exist between modeled and eddy-covariance measured H_s and LE, with correlation coefficient of 0.68, a regression slope of 0.75 and an intercept 30.64 W m^{-2}. However, measured fluxes are also impacted by some degree of uncertainty (i.e. the energy balance is not closed [Sun et al., 2010]). Not withstanding these issues, it can be surmised that the model-data H_s and LE agreement is satisfactory. More significant for the objectives here is the ability of the model to capture the time variation of z_{ABL} (see Fig. S2 in the Appendix) and predict the initiation of CR events (Fig. 4.2). As already mentioned, the probability of initiation of a CR event is necessarily dictated by a crossing of the ABL with the LCL (an example is provided in Fig. 4.2a). To further explore the model performance, the measured rainfall time series is cleared from all nighttime events and non-clear sky conditions prior to rainfall. The pdf of the timing error of rainfall events, defined as difference between observed and predicted rainfall initiation time $t_{data} - t_{model}$, is shifted towards positive values, thus indicating that the model tends to satisfactorily anticipate the timing when rainfall events do occur. In particular, 68% of the observed CR events occur after 2 hours from the modeled timing. In fact, it is well known that after the ABL-LCL intersection, a period ranging from few minutes up to 2 hours is needed to generate CR on the ground [Juang et al., 2007].

4.5 Influence of water table fluctuations

The role of WT fluctuations on the predisposition of CR is now investigated using the model. WT depth is chosen as a control parameter since it is a good predictor of soil moisture state and easily measured in the field, thus allowing a broader application at larger scales. Two-years of simulations were conducted by setting a constant WT and using measured T_a, RH and photosynthetically active radiation (PAR) for 2007 and 2008 to produce plausible initial soil moisture profiles at a specified WT. The interacting effects of FA conditions at this preset WT level are explored by including the atmospheric feedback (see Appendix) or censoring them. When the feedbacks are included, simulation runs are conducted for an additional 100 days with periodically forced atmospheric conditions represented by a prototypical clear sky day (chosen here as September 2nd, 2007). The predisposition to CR is then evaluated using the crossing between the ABL and LCL heights at steady state conditions (see Fig. S3 in the Appendix). Since nocturnal ABL dynamics are not modeled, measured T_a and w are imposed at night (periodically forced each evening) and only daytime dynamics are modeled. The whole scheme is then repeated for another WT level until a wide range of WT conditions is explored.

4.5.1 Soil-Plant-ABL Model

When the feedback to the atmosphere is censored, the probability of CR initiation increases (Fig. 4.3) with a lowering of the WT as expected. The increase of predisposition to CR is due to a decrease in LE that then enhances H_s to the atmosphere (via the energy balance residual), thereby increasing z_{ABL} (via the ABL

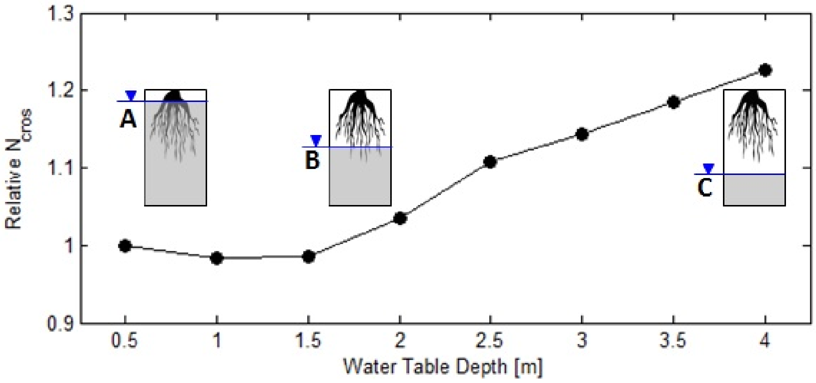

Figure 4.3: Effect of water table fluctuations on the predisposition of CR obtained by the ABL model.

budget equations). In fact, the number of ABL-LCL crossings (N_{cross}) increases by more than 20% when following three possible states: when plants are well watered - no effects are observed (Case A in Fig. 4.3) until a transition zone (Case B) that leads to increased water stress (Case C) and subsequent effect on convection trigger. These results are based on the assumption that RH and T_a are externally imposed and independent from H_s and LE. It is known that a decrease in LE can lead to a suppression of ABL clouds [de Arellano et al., 2012] but, on the other hand, it has also been demonstrated that precipitation may actually be initially enhanced as observed during the early phases of deforestation in Amazonia [Chagnon and Bras, 2005]. The predisposition to CR is therefore controlled by the interplay between H_s and LE at the surface and FA conditions at the top of the ABL.

4.5.2 Atmospheric feedback

When the atmospheric feedback between the soil-plant-ABL system and ABL T_a and RH is allowed, a different picture emerges when compared to the one with imposed T_a and RH. If T_a and RH are controlled by surface and entrainment fluxes, a decrease in LE leads to a decline in boundary layer cloud formation [de Arellano et al., 2012]. A low evaporative fraction (i.e. the ratio between evapotranspiration to available energy) enhances ABL growth and entrainment of dry air thus leading to a decrease in RH and an increase in z_{LCL}. Even though the initial increase in z_{ABL} due to reduced WT promotes CR (positive feedback), the subsequent decrease in RH enhances z_{LCL} and thus reduces the predisposition to CR (negative feedback). To investigate the role of both WT fluctuations and FA conditions on the predisposition of CR, a sensitivity analysis is performed by varying γ_w and WT (Fig. 4.4). The results demonstrate that plants play some role in controlling the occurrence of CR only within a restricted range of γ_w. When w mostly originates from the FA ($\gamma_w >$ -1.0×10^{-6} kg kg^{-1}m^{-1} for the case study) the $z_{LCL}(t)$ is not controlled by plants and the ABL-LCL crossing is not reduced, as in the case of reduced LE fluxes (stress conditions). On the other hand, a transition zone (-2.5×10^{-6} $< \gamma_w <$-1.5×10^{-6} kg kg^{-1}m^{-1} for the case study) exists where the plant stress (WT lower than the

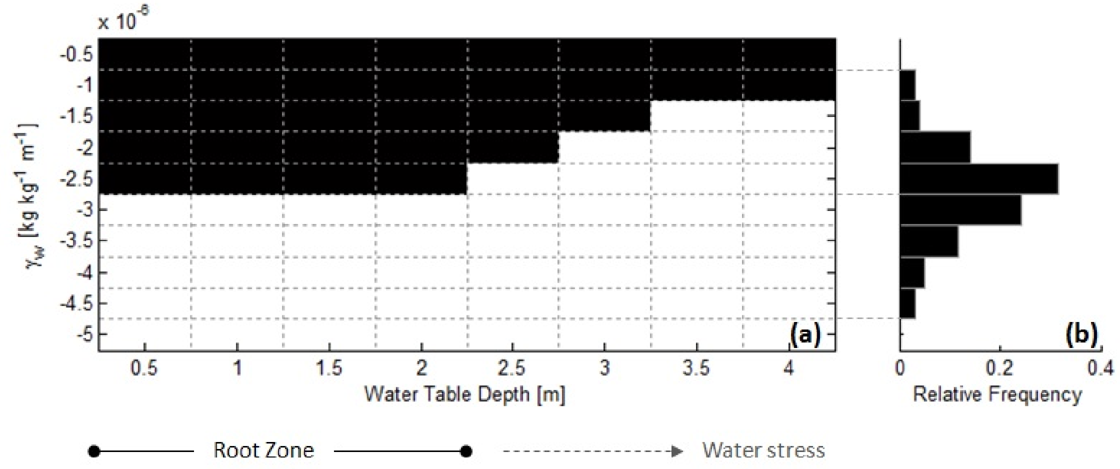

Figure 4.4: Effect of WT fluctuations on predisposition of CR by accounting for the atmospheric feedback. The black region in panel (a) represents ABL-LCL crossing conditions while the white region represents no-rainfall conditions. Note that the relative frequency of γ_w measured at the nearby MHX aiport (from June to September 2007, i.e. during the season of summertime CR) is centered in the transition zone (b).

root zone) may shift the system to an ABL-FA state where boundary layer cloud formation is suppressed (as demonstrated, for example, in de Arellano et al. [2012]). Interestingly, the γ_w observed at a nearby airport (estimated by us from sounding data using a linear regression analysis applied between 500 and 5000 m above the surface) fluctuates in the range of values at this transition zone delineated here.

4.6 Conclusions

Model runs here reveal two contrasting pictures regarding the role of WT fluctuations on the predisposition of CR. When the atmospheric feedback between the soil-plant-ABL system and the ABL temperature and humidity is censored, lowering WT increases the predisposition to CR. The main pathway leading to this increase in predisposition to CR is that reduced WT reduces root-water uptake, increases sensible heat flux, and subsequently leads to an expansion of the convective ABL. Because the ABL air temperature and humidity are externally imposed and not impacted by land-surface or entrainment fluxes, this imposition is equivalent to forcing the LCL dynamics and de-coupling them from the land-surface fluxes. The outcome from this picture is as expected: increases in ABL height alone translate to more frequent crossing with the LCL, thereby enhancing the predisposition to CR. When atmospheric feedback between the soil-plant-ABL system and the ABL temperature and humidity is allowed, the emerging picture is more complex. The predisposition to CR now depends on the FA humidity state, which is governed by synoptic scale processes much larger than the ABL height. If the entrainment flux of water vapor is much larger than LE, then lowering WT increases the predisposition to CR as before. However, if the entrainment flux of water vapor is commensurate to or smaller than LE, then lowering WT reduces the predisposition to CR, which is opposite to the previous case. Here, the expansion in ABL height due to increases in H_s cannot 'keep-up' with the increases in LCL resulting from the dryer air within the ABL column due to reduced LE. Stated differently, if the source of water vapor within the ABL is originating from the soil reservoir, then lowering the WT will suppress CR. On the other hand, if the source of water vapor in the ABL is supplied by the free atmosphere, then lowering WT will have the opposite effect - and the predisposition to CR is increased.

5

Coupled Hydro-Geophysical Data Assimilation

5.1 Summary

The modeling of unsaturated groundwater flow is affected by a high degree of uncertainty related to both measurement and model errors. Geophysical methods such as Electrical Resistivity Tomography (ERT) can provide useful indirect information on the hydrological processes occurring in the vadose zone. In this paper, we propose and test an iteratаed particle filter method to solve the coupled hydrogeophysical inverse problem. We focus on an infiltration test monitored by time-lapse ERT and modeled using Richards equation. The goal is to identify hydrological model parameters from ERT electrical potential measurements. Traditional uncoupled inversion relies on the solution of two sequential inverse problems, the first one applied to the ERT measurements, the second one to Richards equation. This approach does not ensure an accurate quantitative description of the physical state, typically violating mass balance. To avoid one of these two inversions and incorporate in the process more physical simulation constraints, we cast the problem within the framework of a SIR (Sequential Importance Resampling) data assimilation approach that uses a Richards equation solver to model the hydrological dynamics and a forward ERT simulator combined with Archie's law to serve as measurement model. ERT observations are then used to update the state of the system as well as to estimate the model parameters and their posterior distribution. The limitations of the traditional sequential Bayesian approach are investigated and an innovative iterative approach is proposed to estimate the model parameters with high accuracy. The numerical properties of the developed algorithm are verified on both homogeneous and heterogeneous synthetic test cases based on a real-world field experiment. The contents of this chapter has been submitted for publication to the *Journal of Computational Physics* and *Water Resources Research*:

Manoli, G., Rossi, M., Pasetto, D., Deiana, R., Ferraris, S., Cassiani, G., and Putti, M. (2013c). An iterative particle filter approach for coupled hydro-geophysical inversion of a controlled infiltration experiment. *Submitted.*

Rossi, M., **Manoli, G.**, Pasetto, D., Deiana, R., Ferraris, S., Strobbia, C., Putti, M., and Cassiani, G. (2013). Quantitative hydro-geophysical monitoring and modeling of a controlled infiltration experiment. *Submitted.*

5.2 Introduction

Electrical Resistivity Tomography (ERT) is a practical, cost-effective, indirect tool for collecting soil and moisture content data in subsurface environments [Binley and Kemma, 2005, Cassiani et al., 2012, Daily et al., 1992, Yeh and Šimůnek, 2002, Zhou et al., 2002]. When applied to the simulation of the dynamics of the vadose zone, ERT relies on the inversion of the direct current (DC) flow equation providing an image of the electrical resistivity [Binley and Kemma, 2005], with the soil moisture pattern reconstructed from petrophysical relations, such as, e.g., Archie's Law [Archie, 1942]. A second inverse problem is finally used to estimate hydrological model parameters. It is well known that inverse modeling of a parabolic diffusion equation is generally an ill-posed problem and regularization techniques are often employed to achieve well-posedness [Chung et al., 2005, Ha et al., 2006, van den Doel and Ascher, 2006, Yeh and Šimůnek, 2002]. Traditional geophysical inversion is at the same time an over- and under- constrained problem, in the sense that the problem character can change in space, and benefits from the use of prior information embedded in the regularization procedure [Menke, 1984]. However, imposing smoothness via regularization may introduce inaccuracies or even unphysical constraints into the estimates of the hydrological properties [Rings and Hauck, 2009]. To cope with this limitation coupled hydro-geophysical approaches seem highly promising [Hinnell et al., 2010]. By these procedures, the spatial distribution and the temporal dynamics of the geophysical properties are enforced by a physically based hydrologic model combined with petrophysical relations, and explicit assumptions for spatial and temporal regularization are no longer needed.

Even though the coupled approach avoids an independent geophysical inversion, estimation of the hydrologic properties (e.g. soil hydraulic parameters) is still a highly non-linear, mixed-determined inversion problem. For these reasons, although parameter estimation can be made theoretically well-posed, the physical interpretation of the estimated parameters is still not well understood [Hansen and Penland, 2007]. The presence of structural model errors (model approximations, uncertain initial conditions, etc.), as well as measurement uncertainties, suggests that a deterministic search for the best parameters is not likely to converge to a single set of "true" values. A stochastic approach based on ensemble forecasting seems therefore the most appropriate solution procedure [Hansen and Penland, 2007, Smith et al., 2009].

Sequential Data Assimilation (S-DA) methods (typically called filters) have been successfully applied to improve model predictions by incorporating real system observations onto the dynamical model and have been already employed to correct the hydrological states of groundwater infiltration models [Camporese et al., 2009b]. Their ability to include structural and parametric error distributions make them particularly attractive for application to the problem of dynamic parameter estimation [Hansen and Penland, 2007]. Because of the high nonlinearity of porous media infiltration models, the typical filtering method used in hydrological applications is the Ensemble Kalman filter (EnKF) [Evensen, 2003]. Notwithstanding the linear optimality properties of the Kalman Gain [Jazwinski, 1970], the main limitation of EnKF is that it is based on the Gaussian approximation of the filtering probability distribution, possibly leading to inaccurate results or even divergence of the posterior pdfs in presence of a strongly nonlinear relation between observations and state variables [Arulampalam and Ristic, 2000, Gauthier et al., 1993, Pasetto et al., 2012]. To cope with arbitrary non-Gaussian prior distributions, the family of particle filters is a highly attractive alternative, as it is directly based on the Bayesian filtering rule [Doucet et al., 2000, Gordon et al., 1993]. Particle filters have been recently introduced into hydrology [Hsu et al., 2009, Moradkhani et al., 2005, Pasetto et al., 2012, Weerts and El Serafy, 2006, Zhou et al., 2006] and used also for estimation of hydrological model parameters [Hendricks Franssen and Kinzelbach, 2008, Salamon and Feyen, 2009, Vrugt et al., 2005]. All these latter studies focus on the assimilation of direct hydrological information (e.g. discharge [Pasetto et al., 2012] or soil moisture data [Camporese et al., 2009a, Montzka et al., 2011, Plaza et al., 2012]). Recently, a coupled hydro-geophysical parameter estimation procedure by S-DA has been presented by [Rings et al., 2010], but its ability to provide accurate estimates of unknown model parameters remains to be proven, as shown by the consistent underestimation of saturated hydraulic conductivity in the results of [Rings et al., 2010]. As a matter of fact, the structural uncertainties of both the hydrologic evolution and geophysical observation models strongly affect the estimated parameters. Sequential filters correct both model parameters and state variables at each assimilation time, yielding identified parameter values that vary in time [Hansen and Penland, 2007].

In this paper we propose an iterative procedure to overcome the problem of the sensitivity to the initial guess and provide accurate identification of unknown model parameters from indirect state information. The method is grounded on a Sequential Importance Resampling (SIR) particle filter, already tested in similar hydrological applications [Pasetto et al., 2012, Rings et al., 2010], whereby an ERT forward simulation model is embedded into the observation equation and both parameter and state distributions are updated at each assimilation step. Iteration is introduced by sequentially repeating until convergence the same simulation period, using as initial guess the state values and parameter pdfs evaluated from the results of the previous iteraton. Compared to more sofisticated statistical updates, the use of iterations allows the inclusion of a less accurate but computationally more efficient inversion scheme able to cope with large dimensional problems. We validate the methodology on synthetic test cases and apply the methods to a field experiment comparing the results of our procedure with traditional uncoupled inversion of ERT data. We focus on both homogeneous and heterogeneous systems with parameters distributed by zones. The proposed procedure displays convergence of the posterior distribution towards the correct value of the hydraulic conductivity in both the homogenous and heterogeneous scenarios independently from the initial guess. The numerical results obtained from the synthetic test cases show that the iterativ approach yields faster convergence with respect to standard DA methods, using consistently smaller ensemble sizes and a drastic reduction of the number of forward model runs, in particular for the heterogeneous test case. The results obtained in the application to the real world problem are consistent with the desired physical constraints at relatively low computational costs, thus improving significantly on existing coupled flow-ERT procedures.

5.3 Parameter estimation by sequential data assimilation

The state space model describing the S-DA problem can be written as:

$$\begin{aligned} x_t &= \mathcal{F}(x_{t-1}, \lambda, w_t), \qquad (5.1)\\ y_t &= \mathcal{H}(x_t, \lambda, v_t), \qquad (5.2) \end{aligned}$$

where x_t is the state vector at assimilation time t, $\mathcal{F}$ is the evolution operator, λ is the time-independent parameter vector, w_t is the stochastic model error, y_t is the observation vector, $\mathcal{H}$ is the observation model, and v_t is the stochastic error term in the observations. Model uncertainty is connected, e.g., to structural model errors, parameter errors, initial solution errors, etc. Casted in a stochastic framework, the objective of S-DA is to estimate the posterior probability density function (pdf) of the state vector at time t conditioned to the observations y_t^{obs} that become available at time t. Because of model nonlinearity, Monte Carlo-based approaches are used to discretize the state and observation pdfs in equations (5.1) and (5.2). To relax the Gaussian hypothesis inherent to Kalman-filter based algorithms we estimate the state and parameter pdfs employing a SIR (Sequential Importance Resampling) particle filter, which has been successfully tested in hydrological applications [Pasetto et al., 2012] in standard S-DA mode.

5.3.1 Sequential Importance Resampling for parameter estimation

Let the state vector x_t be characterized by a probability density function denoted by $p(x_t)$ and let $p(\lambda)$ be the prior distribution of the parameters λ. The sequence of random variables $\{x_0, x_1, \dots\}$ defines a Markov chain where (5.1) and $p(w_t)$ uniquely identify the transition probability density function $p(x_t|x_{t-1}, \lambda)$. The variance associated to $p(x_t)$ typically increases with time during the numerical simulation, leading to highly uncertain forecasts. Our goal is to obtain the posterior distribution of the parameters λ and of the state variables x_t, conditioned to the field observations $y_{1:t}^{obs}$, i.e., the filtering pdf $p(x_t, \lambda|y_{1:t}^{obs})$. Sequential data assimilation allows to compute a posterior distribution as soon as a field observation y_t^{obs} becomes available. For this reason in the following we will assume that the parameters are time dependent, λ_t, in the sense that they may change when their posterior distribution changes.

The S-DA technique consists of two basic steps that are repeated sequentially. In the forecast step the state pdf is propagated in time to obtain the forecast pdf,

$p(x_t, \lambda_t | y^{obs}_{1:t-1})$. This is expressed by the Chapman-Kolmogorov equation as:

$$p\left(x_t, \lambda_t | y^{obs}_{1:t-1}\right) = \int p\left(x_t, \lambda_t | x_{t-1}, \lambda_{t-1}\right)\, p\left(x_{t-1}, \lambda_{t-1} | y^{obs}_{1:t-1}\right) dx_{t-1} d\lambda_{t-1}. \tag{5.3}$$

Note that in this step we have the effective propagation from time $t-1$ to time t of the system state by formal application of (5.1) using constant values of the parameters. The second step is called analysis or update and consists in correcting the forecast pdf using the new field observation y^{obs}_t. Bayes' theorem allows the factorization of the filtering pdf as:

$$p\left(x_t, \lambda_t | y^{obs}_{1:t}\right) = C p\left(y^{obs}_t | x_t, \lambda_t\right) p\left(x_t, \lambda_t | y^{obs}_{1:t-1}\right),$$

where C is a normalization constant and the other two factors are the likelihood function, to which we assign a known distribution, and the forecast pdf, computed in (5.3), respectively. The analysis step essentially consists in a reinitialization of the system state variables and of the parameters given the forecast and the observations.

In the SIR algorithm the forecast and filtering pdfs are approximated using an ensemble of N random samples (also called particles), $\{x^{(i)}_t, \lambda^{(i)}_t\}$, $i = 1, \ldots, N$, with associated weights $\{\omega^{(i)}_t\}$, $i = 1 \ldots, N$:

$$p\left(x_t, \lambda_t | y^{obs}_{1:t-1}\right) \approx \sum_{1=1}^{N} \omega^{(i-)}_t \delta\left(x_t - x^{(i-)}_t\right) \delta\left(\lambda_t - \lambda^{(i-)}_t\right), \tag{5.4}$$

$$p\left(x_t, \lambda_t | y^{obs}_{1:t}\right) \approx \sum_{1=1}^{N} \omega^{(i+)}_t \delta\left(x_t - x^{(i+)}_t\right) \delta\left(\lambda_t - \lambda^{(i+)}_t\right), \tag{5.5}$$

where $\delta(\cdot)$ is the Dirac delta function, and superscripts '$-$' and '$+$' denote the realizations before and after the update, respectively. The SIR algorithm starts by assigning uniform weights to the N realizations of the ensemble. The Monte Carlo discretization reduces the forecast step to the propagation in time of the ensemble members using the system dynamics and, in the update step, new weights are calculated recursively, by means of the likelihood function, as:

$$\omega^{(i)}_t = C \omega^{(i)}_{t-1} p(y^{obs}_{1:t} | x^{(i-)}_t, \lambda_t), \tag{5.6}$$

where C is a normalization constant. To avoid the ensemble deterioration phenomenon [**?**], resampling is performed when $N_{eff} < 0.5N$, where N_{eff} is the effective ensemble size, evaluated as:

$$N_{eff} = \left[\sum_{i=1}^{N} (\omega^{(i)}_t)^2\right]^{-1},$$

and is representative of the number of realizations that have non-negligible weights. We adopt the systematic resampling method [**?**], to duplicate samples with large weight and discard samples with negligible weight. The resampling procedure maintains the ensemble size equal to N by generating new members using parameters drawn from the posterior distribution and assigning to them uniform weights. The duplicated realizations will then differentiate in the following forecast step. If the resampling step does not occur, i.e., all the particles have sizable weights, then $x^{(i+)}_t = x^{(i-)}_t, \lambda^{(i+)}_t = \lambda^{(i-)}_t$ and only the weights are changed according to (5.6), yielding an effective weighted distribution given by (5.4) and (5.5).

5.3.2 Iterative parameter estimation

Since the resampling step is a reinitialization of the system state variables at an observation time, it is convenient to use this step to sample new realizations from the posterior pdf of the parameters. Let $\{\hat{\lambda}_t^{(i)}\}$, $i = 1, \ldots, N$ be the parameter values of the realizations after the resample. Most of these parameters are equal, the number of different values corresponding to the number of realizations that have non-negligible weights. Maintaining these values for the parameter update, i.e. $\lambda_t^{(i+)} = \hat{\lambda}_t^{(i)}$, may yield an impoverishment of the ensemble with the consequence that the posterior distribution is not adequately explored and erroneous parameter estimations may be identified. This can be exemplified in the case that only one realization is duplicated after the resample. In this case the posterior distribution collapses in one single value that cannot change in the subsequent updates. To guarantee a good performance of the filter it is then necessary to perturb the duplicated parameters to effectively explore the relevant pdf. Moradkhani et al. [2005] propose a perturbation of the parameters with independent additive Gaussian variates, $\lambda_t^{(i+)} = \hat{\lambda}_t^{(i)} + \xi_t^{(i)}$, $\xi_t^{(i)} \sim N(0, Var(\lambda_t^{(i-)}))$, while [Moradkhani et al., 2012, Vrugt et al., 2012] use a Markov-Chain sampling of the parameters with the computation of the Metropolis ratio to accept or eventually reject the sampled values. While the first approach requires a large number of realizations, the second strategy incurs in increased computational effort due to the repetition of the forecast step necessary for the computation of the Metropolis ratio. Here we propose to sample the updated parameters from a probability distribution that maintains the initial structure, but employing the moments updated with the ensemble statistics. For example, assuming an initial distribution defined only by the first and second moments (e.g., uniform, normal, log-normal distributions), the proposed scheme updates the expected value μ_{λ_t} and the coefficient of variation cv_{λ_t} on the basis of the prior $\{\lambda_t^{(i-)}\}$ and the resampled $\{\hat{\lambda}_t^{(i)}\}$ parameters. To this aim, we impose that the expected value of the new distribution be given by the mean of the resampled parameters:

$$\mu_{\lambda_t} = E[\hat{\lambda}_t^{(i)}], \tag{5.7}$$

and the coefficient of variation be given by the maximum between the coefficient of variations of the forecasted and the updated parameters,

$$cv_{\lambda_t} = s \cdot \max\left(cv_{\lambda_t^{(-)}}, cv_{\hat{\lambda}_t}\right), \tag{5.8}$$

where s is a tuning coefficient used to force a gradual reduction of the variance of the distribution (typically s=0.9) and the use of the maximum value avoids the fast collapse of the filter when only a few realizations are resampled. The sequence of posterior parameter distributions obtained with this procedure needs several updates to converge and hence we iterate the filtering procedure by cyclic repetition of the assimilation interval until the resampling step is no longer performed at any update of the period. This stopping criterion ensures that no further progresses are obtained by continuing the iterations. A more computationally savvy approach would be to stop on the basis of average residual or parameter update metrics. At each restart of the filtering process (external iteration) the mean and variance of the

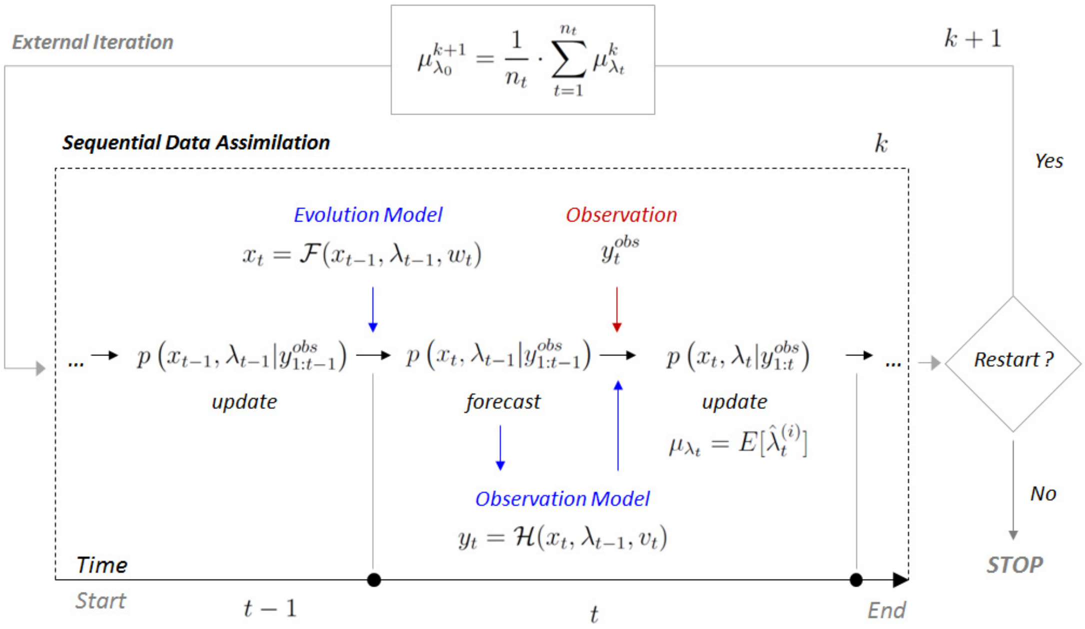

Figure 5.1: Scheme of the iterative particle filter method (modified from [Dowd, 2007]). The data assimilation cycle starts with a distribution of the system state at time $t-1$ which is used by the evolution model to provide a forecast at time t. The forecast state is converted by the observation model into a forecasted observation which is combined with the field observation y_t to produce the update at time t. When all the available data are assimilated, the data assimilation cycle is restarted (k-th external iteration) until convergence of the model parameter λ_t (see main text for details).

prior distribution of the parameters is updated by:

$$\begin{aligned} \mu_{\lambda_0}^{k+1} &= \frac{1}{n_t} \sum_{t=1}^{n_t} \mu_{\lambda_t}^k, \\ cv_{\lambda_0}^{k+1} &= \frac{1}{n_t} \sum_{t=1}^{n_t} cv_{\lambda_t}^k, \end{aligned}$$

where n_t is the number of updates in each S-DA cycle (k-th external iteration). Instead of restarting the S-DA procedure with the posterior distribution at the previous S-DA cycle, we use a “mean posterior disitribution” to reduce the effect of the initial bias on the parameter estimation. The procedure is illustrated schematically in Figure 5.1.

5.4 Evolution and Observation models of water infiltration and ERT

In this study we are interested in applying the S-DA method to a coupled hydrogeophysical model. The evolution model (5.1) describes the soil moisture dynamics in the vadose zone and ERT observations are used to update system state and parameters by means of a geophysical electrical current flow observation model (5.2).

5.4.1 Evolution model

We use Richards' equation to describe the infiltration process in a variably-saturated isotropic porous medium:

$$S_s S_w(\psi)\frac{\partial \psi}{\partial t} + \phi \frac{\partial S_w(\psi)}{\partial t} = \vec{\nabla} \cdot \left[\boldsymbol{K}_s K_r(\psi)\left(\vec{\nabla}\psi + \eta_z\right)\right] + q, \tag{5.9}$$

where S_s is the elastic storage term, S_w is water saturation, ψ is water pressure, t is time, ϕ is the porosity, $\boldsymbol{K}_s$ is the saturated hydraulic conductivity tensor, K_r is the relative hydraulic conductivity, $\eta_z = (0,0,1)^T$ with z the vertical coordinate directed upward and q is a source/sink term. The saturated hydraulic conductivity is modeled as a diagonal matrix and its components K_x, K_y and K_z are the saturated hydraulic conductivities along the coordinate directions x, y and z, respectively. Equation (5.9) is highly nonlinear due to the pressure head dependencies of saturation and relative hydraulic conductivity. These constitutive functions are modeled using the characteristic relations proposed by [van Genuchten and Nielsen, 1985]:

$$S_w(\psi) = \begin{cases} (1 - S_{wr})(1 + \beta_\psi)^{-m} + S_{wr} & \psi < 0, \\ 1 & \psi \geq 0, \end{cases} \tag{5.10}$$

$$K_r(\psi) = \begin{cases} (1 + \beta_\psi)^{-m/2}\left[(1 + \beta_\psi)^m - \beta_\psi^m\right]^2 & \psi < 0, \\ 1 & \psi \geq 0, \end{cases} \tag{5.11}$$

where S_{wr} is the residual water saturation, $\beta_\psi = (\psi/\psi_s)^\alpha$, ψ_s is the capillary or air entry pressure, α is a constant and $m = 1 - 1/\alpha$, with $1.25 < \alpha < 6$. Equation (5.9) is numerically solved using the subsurface module of the CATHY model (CATchment HYdrology [Camporese et al., 2010]), a linear tetrahedral finite element method with backward Euler scheme with adaptive time stepping and Newton-like iterations for the solution of nonlinear system [Paniconi and Putti, 1994]. The system state vector x_t of (5.1) collects the nodal pressure head ψ at simulation time t. The nonlinear function $\mathcal{F}$ is a formal representation of the numerical solver and comprises a number of time steps to advance within the assimilation interval $[t-1, t]$. The stochastic noise w_t, kept constant during the forecast step, represents model uncertainty and is generally specified by a normal or lognormal distribution of the parameters.

5.4.2 Observation model

We monitor the infiltration process with ERT measurements. ERT emits direct current (DC) from evenly spaced electrodes installed at the soil surface and monitors the electrical potential differences at other locations. The DC injection pairs are moved sequentially to generate a number of electrical potential fields. Using moisture content-resistivity relationships (e.g., Archie's Law [Brovelli and Cassiani, 2011, Brovelli et al., 2005]) and assuming that changes in conductivity correspond to changes in moisture content, the water flow in the vadose zone can be monitored [Hinnell et al., 2010, Nenna et al., 2011, Rings et al., 2010]. The intensity of the electrical potential field $\varPhi$ induced in the soil by the input current can be modeled as [Nenna et al., 2011]:

$$-\vec{\nabla} \cdot \left[\kappa\left(S_w\right) \vec{\nabla} \varPhi\right] = I\left[\delta\left(\vec{r} - \vec{r}_{S+}\right) - \delta\left(\vec{r} - \vec{r}_{S-}\right)\right], \tag{5.12}$$

where κ is the scalar electrical conductivity of the bulk (porous medium plus contained fluid), I is the applied current, δ is the Dirac delta function, and $\vec{r}_{S+}$ and $\vec{r}_{S-}$ are the current source and sink electrode position vectors, respectively. The soil electrical conductivity is related to saturation according to the following petrophysical relationship that is derived from Archie's law [Archie, 1942]:

$$\kappa\left(S_w\right) = \kappa\left(t_0\right)\left(\frac{S_w\left(t\right)}{S_w\left(t_0\right)}\right)^n, \tag{5.13}$$

where $S_w(t_0)$ and $\kappa(t_0)$ are the initial water saturation and the corresponding initial electrical conductivity of the soil, respectively, and n is a dimensionless parameter generally calibrated in the lab using soil samples. Since water saturation varies during the infiltration process, the induced electric field is time dependent. Let y_t^{obs} be the vector collecting the electrical potential differences that are observed at the measurement electrodes at time t. Equations (5.10)-(5.11), (5.12) and (5.13) imply that there exists a nonlinear relation between the water pressure in the soil and the electrical potential differences at all electrodes. In fact, van Genuchten relations (5.10)-(5.11) and Archie's law (5.13) allow us to calculate the soil electrical conductivity field from the water pressure. Equation (5.12) is solved numerically using a three-dimensional linear finite element solver. In order to avoid boundary effects on the simulated electrical potential, the model domain used to simulate the infiltration experiment for both the hydrological and DC current models is enlarged in the three spatial directions to accommodate the geophysical simulations. The solution of (5.12) gives the electrical potential differences $y_{t,i}$, $i = 1, \ldots, N_{obs}$, at the N_{obs} electrode positions to be compared to the corresponding field measurements y_t^{obs}. The general observation model of equation (5.2) becomes $y_t = \mathcal{H}\left(\psi_t\right)$, where $\mathcal{H}$ embeds the nonlinear relation between the soil moisture and the electric potential. The observation y_t^{obs} can then be related to the measurement model using the measurement uncertainties as:

$$y_t^{obs} = y_t\left(1 + v_t\right),$$

where v_t is the observation error, modeled as an unknown realization of a normal random variable with zero mean and standard deviation equal to σ_y. The term v_t incorporates both measurement errors and observation model uncertainties. From the previous equation and the probability distribution of v_t we can now explicitly

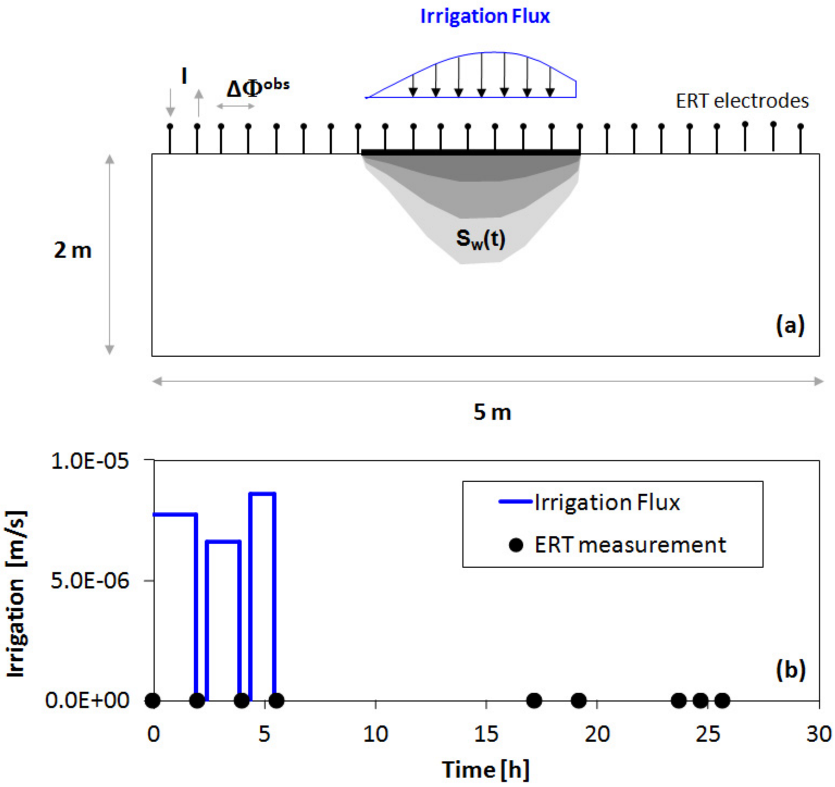

Figure 5.2: Schematic representation of the system geometry (a) and time-behavior of the infiltration flux rates imposed at the surface boundary (b). Black dots indicate the time of ERT measurements.

derive the expression for the likelihood function $p(y_t^{obs}|x_t)$, which in the case of a normal distribution becomes:

$$p\left(y_t^{obs}|x_t\right) = C \cdot exp\left[-\frac{1}{2}\sum_{j=1}^{N_{obs}}\left(\frac{y_{t,j}^{obs} - y_{t,j}}{\sigma_y y_{t,j}}\right)^2\right],$$

where C is a normalization constant. This pdf is estimated from the MC ensemble, hence completing the overall inversion algorithm.

5.5 Experimental Results

The performance of the proposed approach was tested on a controlled infiltration field experiment. First, using the geometry of the real case study, a synthetic problem is designed in order to assess the convergence properties of the developed scheme, then, the real field experiment is simulated.

The controlled infiltration experiment is described in [Rossi et al., 2013] and is similar to a previous experiment discussed by [Cassiani et al., 2009a]. The experimental site is located in Grugliasco (Turin, Italy), nearby the campus of the Agricultural Faculty of the University of Turin. It is characterized by a regular

Table 5.1: Time invariant model parameters

Parameter	Description	Unit	Value	Reference
Evolution model				
ϕ	Soil porosity	-	0.33	[Cassiani et al., 2009b]
S_s	Elastic storage	m^{-1}	5.0E-04	Assumed
S_{wr}	Residual saturation	-	0.003	[Canone et al., 2008]
ψ_r	Capillary pressure	m	-0.185	[Canone et al., 2008]
α	VG model parameter	-	2.0	[Canone et al., 2008]
Observation model				
n	Archie's law parameter	-	1.27	[Cassiani et al., 2009b]
$S_w(t_0)$	Initial value of S_w	-	0.21	Field data
$\kappa(t_0)$	Initial value of κ	S m^{-1}	7.69E-04	Field data

stratigraphic sequence of sandy soil composed mainly of eolic sands with low organic content [Baudena et al., 2012, Cassiani et al., 2009b]. In the unsaturated zone, sand grains are relatively homogeneous with a median diameter (d_{50}) of 200 μm and porosity of $\phi = 0.33$ forming a homogeneous and isotropic soil in the horizon interested by the infiltration process [Cassiani et al., 2009b]. The water table is located approximately 20 m below the surface and the vadose zone is not influenced by the underlying aquifer. A line of sprayers was used to wet an area of about 3 m×20 m for 6 hours using variable in time irrigation rates (shown in Figure 5.2(b)).

The infiltration front was monitored by means of both ERT and GPR WARR surveys [Rossi et al., 2013] along a cross section of the irrigated area. ERT was performed in time-lapse mode using a dipole-dipole configuration, using 24 electrodes placed on the soil surface with a regular spacing of 0.2 m. ERT data were acquired before irrigation (background ERT), during short intervals within the irrigation period, and after the end of irrigation for the following 24 hours. The exact timings of the ERT acquisitions used in the data assimitation procedure (i.e. during and after irrigation) are shown as bullets in Figure 5.2(b).

Soil samples at different depths were collected and used to obtain laboratory estimates of the hydrological parameters S_s, ϕ, α, ψ_s, and S_{wr}, as well as Archie's law constant n. Initial volumetric water content was estimated from GPR measurements at 0.07 $\mathrm{m}^3\ \mathrm{m}^{-3}$, corresponding to an initial water saturation $S_w(t_0) = 0.21$, while background ERT measurements were used to determine the initial soil electrical conductivity $\kappa(t_0) = 7.69 \times 10^{-4}$ S m^{-1}, corresponding to a resistivity of 1300 Ω m. This value is in accordance with Archie's law parameter calibrated during the laboratory experiments [Cassiani et al., 2009b]. The values of these parameters are reported in Table 5.1.

Inverted resistivity data, obtained from the uncoupled approach developed by [Binley and Kemma, 2005], revealed that irrigation was not uniformly distributed in the direction orthogonal to the sprinkler line, probably due to the presence of wind [Rossi et al., 2013]. This was taken into account in order to properly define the top boundary conditions and the irrigation flux was thus modeled with a Gaussian distribution centered at 2.5 m (top boundary), with variance equal to 0.6 m, both values calculated such that the total flux equals the real irrigation rate.

The model of the field experiment is developed using a vertical cross-section orthogonal to the irrigation line, whose schematic representation is illustrated in Figure 5.2(a). For the hydrologic simulation, no-flow boundary conditions (BCs) were set all over the model domain, except for the top boundary where the irrigation rate was imposed as a Neumann flux. Spatially varying input infiltration is considered as a potential rate, and actual infiltration is evaluated based on system state condition allowing the switching between Neumann and Dirichlet BCs in the case of ponding [Camporese et al., 2010].

The finite element grid of the hydrologic model consists of 9792 nodes and 49500 elements while the stationary geophysical model was solved on an enlarged mesh characterized by 21240 nodes and 112404 elements.

5.5.1 Synthetic case

In the synthetic cases, a forward simulation of both the hydrological and the ERT models with pre-imposed parameters was used to generate the true state and the ERT measurements. We are interested in identifying saturated homogeneous or spatially heterogeneous hydraulic conductivity. All other model parameters are based on the values used in the field case study as listed in Table 5.1. The synthetic dataset of ERT observations was generated by the coupled hydro-geophysical forward model assuming the same dipole-dipole configuration of the field experiment. It was then used to constrain the particle filter simulations assuming different levels of measurement errors (σ_y = 5 - 20%).

The convergence of the proposed coupled inversion method is tested by looking at the behavior of a number of error statistics. The discrepancy between measured and simulated observations (electrical potential at the electrodes) is evaluated in terms of ensemble mean relative error (ϵ_y), maximum relative error ($\epsilon_{y,max}$) and root mean square error ($RMSE_y$):

$$\begin{aligned}
\epsilon_y &= \frac{1}{N}\sum_{i=1}^{N}\left[\frac{1}{N_{obs}}\sum_{j=1}^{N_{obs}}\frac{|y_{t,j}^{i,\Phi}-y_{t,j}^{obs}|}{|y_{t,j}^{obs}|}\right] \\
\epsilon_{y,max} &= max_i\left\{max_j\left\{\frac{|y_{t,j}^{i,\Phi}-y_{t,j}^{obs}|}{|y_{t,j}^{obs}|}\right\}\right\} \\
RMSE_y &= \frac{1}{N}\sum_{i=1}^{N}\left[\frac{1}{N_{obs}}\sqrt{\sum_{j=1}N_{obs}\frac{|y_{t,j}^{i,\Phi}-y_{t,j}^{obs}|^2}{|y_{t,j}^{obs}|^2}}\right]_i
\end{aligned}$$

We also look at the L_2-norm of the error ϵ_ψ between the true and the simulated system state values, soil water pressure head, named the pressure error:

$$\epsilon_\psi = \|\bar{\psi}_t - \psi_t^{true}\|_2$$

where $\bar{\psi}_t$ is the ensemble mean pressure field at time t. For all the simulations we require a fixed number (8) of iterations chosen so that convergence is reached within a reasonable computational time and a reliable assessment of error statistics is obtained. The use of one of the stopping criteria proposed in section 5.3.2 would yield faster convergence in all test cases.

5.5.1.1 Homogeneous test case

In this test case, an isotropic and homogeneous soil with hydraulic conductivity equal to $\boldsymbol{K}_s = 10^{-5}$ [m s^{-1}] was employed. The saturated hydraulic conductivity tensor is thus the only unknown parameter $\lambda_t = \{\boldsymbol{K}_s\}$ with $K_x = K_y = K_z$ (homogeneous and isotropic soil).

A preliminary sensitivity analysis on the ensemble size carried out with $N = 20, 50, 100$ suggests that 20 particles are enough for this case study to obtain reliable estimates. Hence, a value $N = 20$ particles is used to test the performance of the method with the different measurement errors (Figure 5.3). However, to better illustrate the behaviour of the pdf of the hydraulic conductivity during the iterative procedure, the simulation results obtained with 100 particles are also shown (Figure 5.4).

The hydraulic conductivity estimated by the iterative particle filter method is shown to converge to the true value $\boldsymbol{K}_s^{true}$ as the number of updates is sufficiently large (Figure 5.3). The number of updates necessary for convergence is shown to depend on the measurement error: when the true observations are assimilated, i.e. when the observations are not randomly perturbed, the method approaches $\boldsymbol{K}_s^{true}$ after four iterations (Figure 5.3a) but for increasing noise, more iterations are needed to achieve convergence. As a matter of fact, for $\sigma_{\Phi} = 5\%$ and 20% the estimated value $\mu_{\lambda_{t,k}}$ keeps oscillating until the 6^{th} and 7^{th} external iteration, respectively (Figure 5.3(c) and Figure 5.3(e)). Our iterative DA approach allows reducing the error between simulated and observed states and the relative errors on the identified parameters stabilize at a value that necessarily increases with measurement noise. The convergence speed depends on σ_{Φ}, observing slower convergence for higher noises. The results demonstrate that the traditional particle filter (i.e. the non-iterative approach) may provide a biased estimate of the model parameter unless larger ensemble sizes are used. This is highlighted in Figure 5.4 where the pdf of the hydraulic conductivity at different updates of the first and second iterations are shown. If the initial guess of the model parameter is overestimated, the predicted value at the end of the first iteration (8^{th} update in Figure 5.4(a)) is underestimated. This is due to the fact that the particle filter has to correct the model parameter more than necessary to balance the bias on the predicted state during the initial updates. For example, a higher initial estimate of $\boldsymbol{K}_s$ corresponds to a higher infiltration capacity and thus causes an over-estimated total infiltrated water, with a corresponding over-estimation of the front speed. Hence, at later times, the inversion procedure must identify an under-estimated $\boldsymbol{K}_s$ to accommodate the slower observed saturation front depth. As a result, the pdf of the parameter is shifted further than necessary on the opposite direction of the initial guess. The iterative approach allows the filter to “forget” the initial bias and converge more efficiently to the true parameter (Figure 5.4(b)). The results in Figure 5.5 show that the error ϵ_{ψ} develops at the edge of the infiltration front where sensitivities are highest. The iterative procedure successfully reduces the discrepancy between simulated and true system

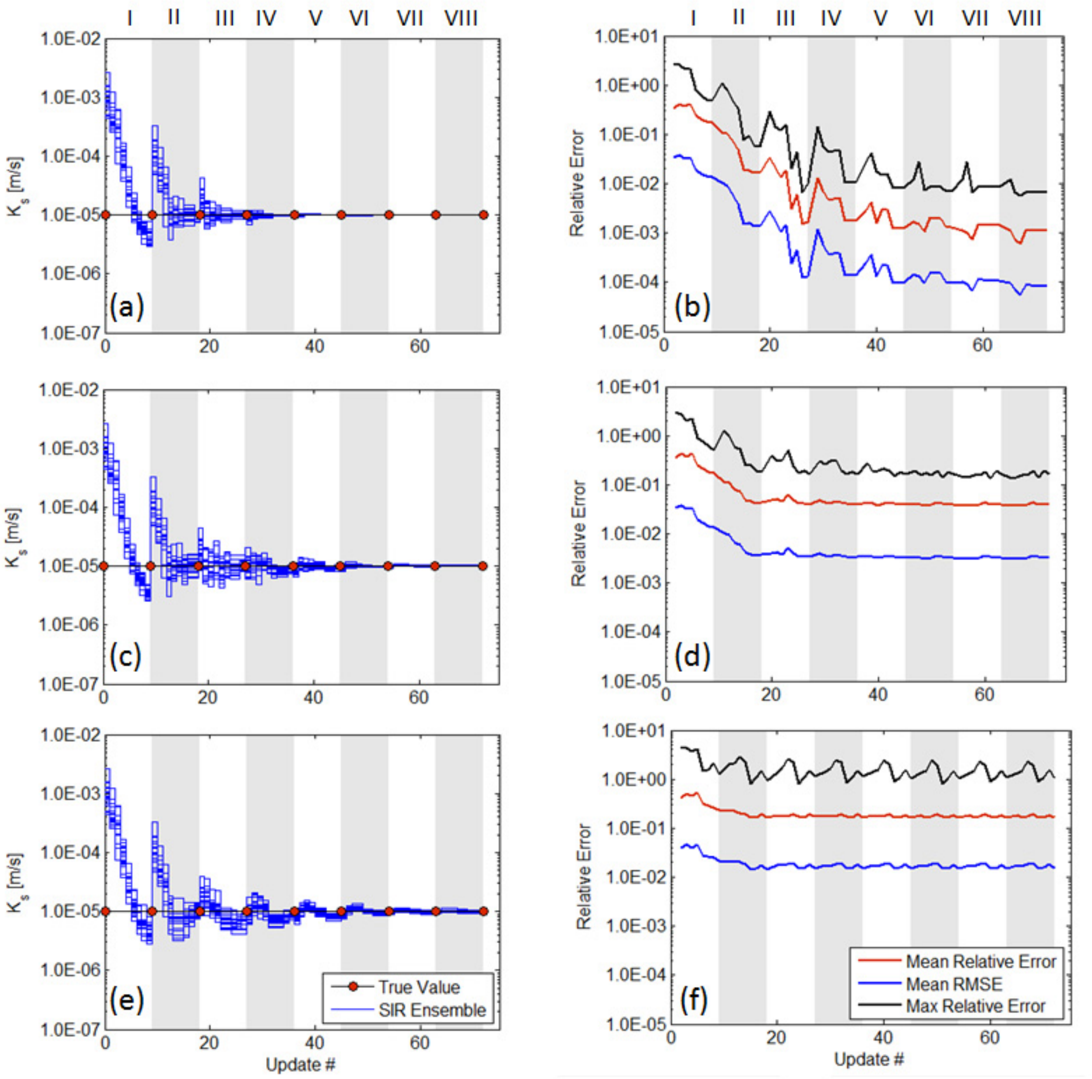

Figure 5.3: Synthetic test case results: convergence of the hydraulic conductivity (a,c,e) and relative errors between true and simulated observations (b,d,f). Mean relative error (ϵ_y), Mean $RMSE_y$ and Maximum Relative error ($\epsilon_{y,max}$) are shown. The performance of the method for different measurements error is illustrated: (a,b) $\sigma_{\Phi} = 5\%$ with measurements not randomly perturbed, (c,d) $\sigma_{\Phi} = 5\%$, and (e,f) $\sigma_{\Phi} = 20\%$ with randomly perturbed measurements. Red dots indicate the true value of $\boldsymbol{K}_s$. The roman numerals indicate the external iteration step. Each external iteration consists of 8 SIR updates

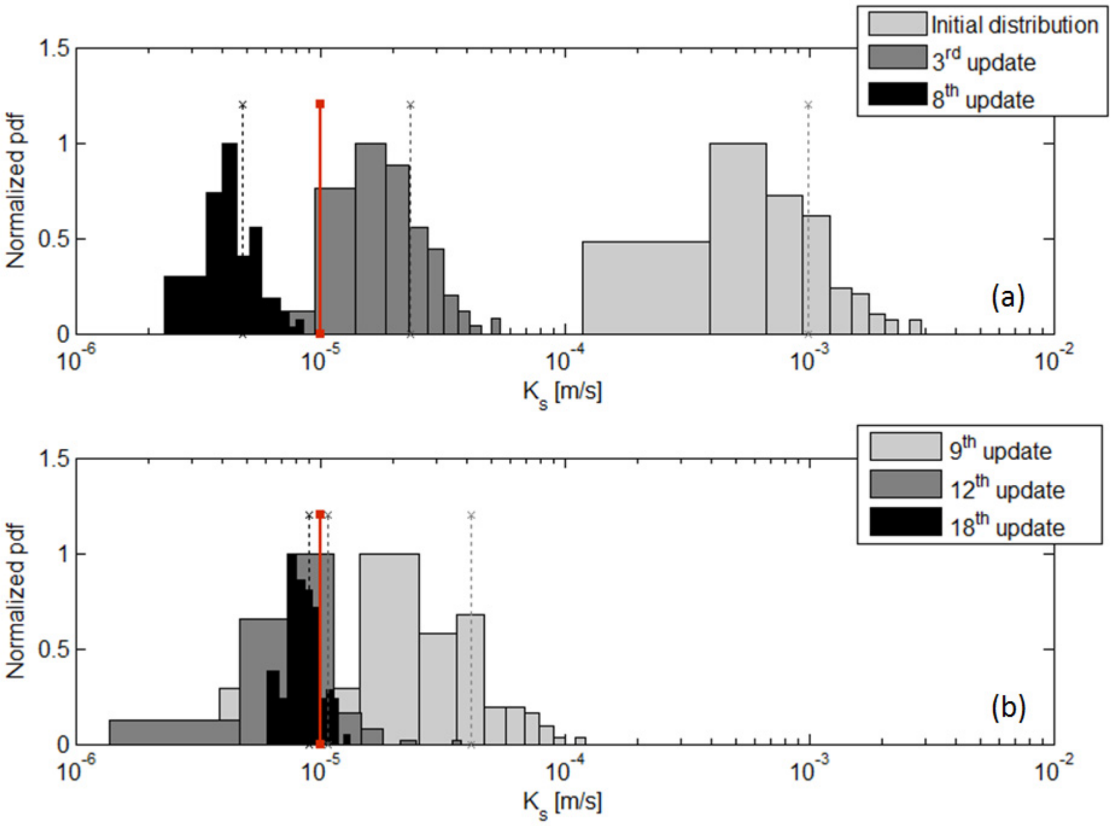

Figure 5.4: Synthetic test case results: pdf of the hydraulic conductivity normalized on the maximum value of the pdf. Panel (a) and (b) refer to the first and second external iteration of the SIR method, respectively. The simulation was run with an ensemble size N=100. Dotted lines indicate the ensemble mean and the red line indicates the true value of $\boldsymbol{K}_s$.

state and the restart is shown to be fundamental to achieve negligible errors. The traditional SIR method corrects also the system state after each update but errors up to 0.6 m (in term of predicted pressure head) are still observed at the end of the first iteration of the sequential procedure. The iterated approach allows instead a reduction of the error ϵ_y down to negligible values ($\epsilon_y < 10^{-3}$ m). The synthetic simulations confirmed that the particle filter is an efficient method to update the system state and the iterative procedure is shown to be essential to provide precise estimates of the model parameters at lower computational effort.

5.5.1.2 Heterogeneous test case

The ability of the proposed methodology to estimate multiple model parameters is now investigated. We consider the same infiltration experiment, now characterized by an isotropic heterogenous soil (Figure 5.6(a-b)). The model domain is divided into four zones with different hydraulic conductivities (thus providing four unknown model parameters). The results of the iterative SIR scheme, shown in Figure 5.6(c-d), demonstrate that the iterative approach successfully estimates multiple model

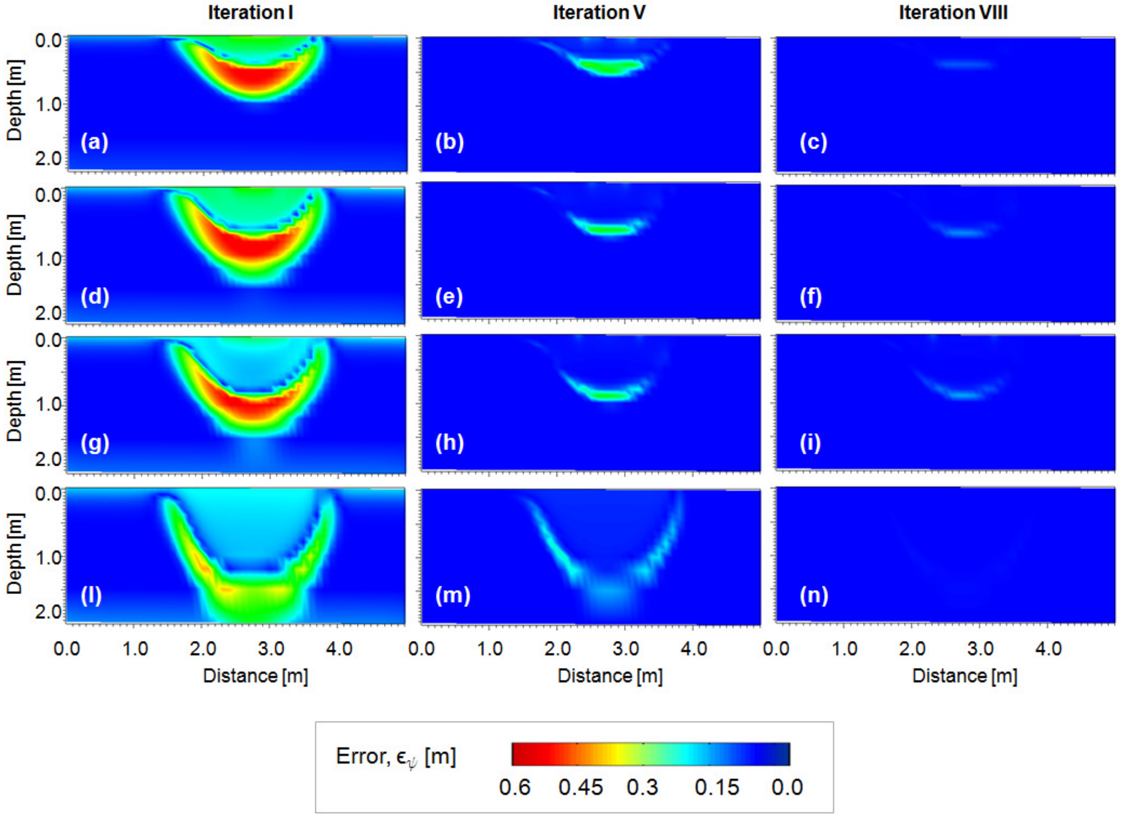

Figure 5.5: Spatial distribution of the error ϵ_ψ, representing the discrepancy between simulated (ensemble mean) and true system state (pressure field).

parameters. In addition, the results in Figure 5.7 show that the method is insensitive to the initial guess μ_{λ_0}, thus confirming the reliability of the proposed approach.

We note that the identification is practically achieved after four iterations, for a total of 80 forward model runs. At later iterations the identified values of zones 3 and 4 display small oscillations whose amplitude seem to decrease slowly (Figure 5.6(e-f)). This is likely due to the fact that both zones 3 and 4 receive information from the infiltration experiment at later times. At the first 4 observation times the true infiltration front is shallower than the material interface, and only the last 4 measurements contribute information towards the identification of hydraulic conductivity of zones 3 and 4.

To test the improvements obtained by our proposed iterative method with respect to standard (non iterative) DA methods, we solve the same problem with a one-iteration SIR approach but with an ensemble size $N = 160$. This value corresponds the same number of forward model runs used in the previous simulations using (pre-fixed) eight iterations. We perform this comparison for the case of $\sigma_\Phi = 20\%$ and randomly perturbed measurements.

The convergence results of the iterative and non-iterative procedures for this case are compared in Figure 5.8. The iterated simulation converges to the correct hydraulic conductivities of zones 1, 2 and 3, and only a small discrepancy exists in the estimation of $\boldsymbol{K}_s$ in zone 4. The value of this bias is consistent with the

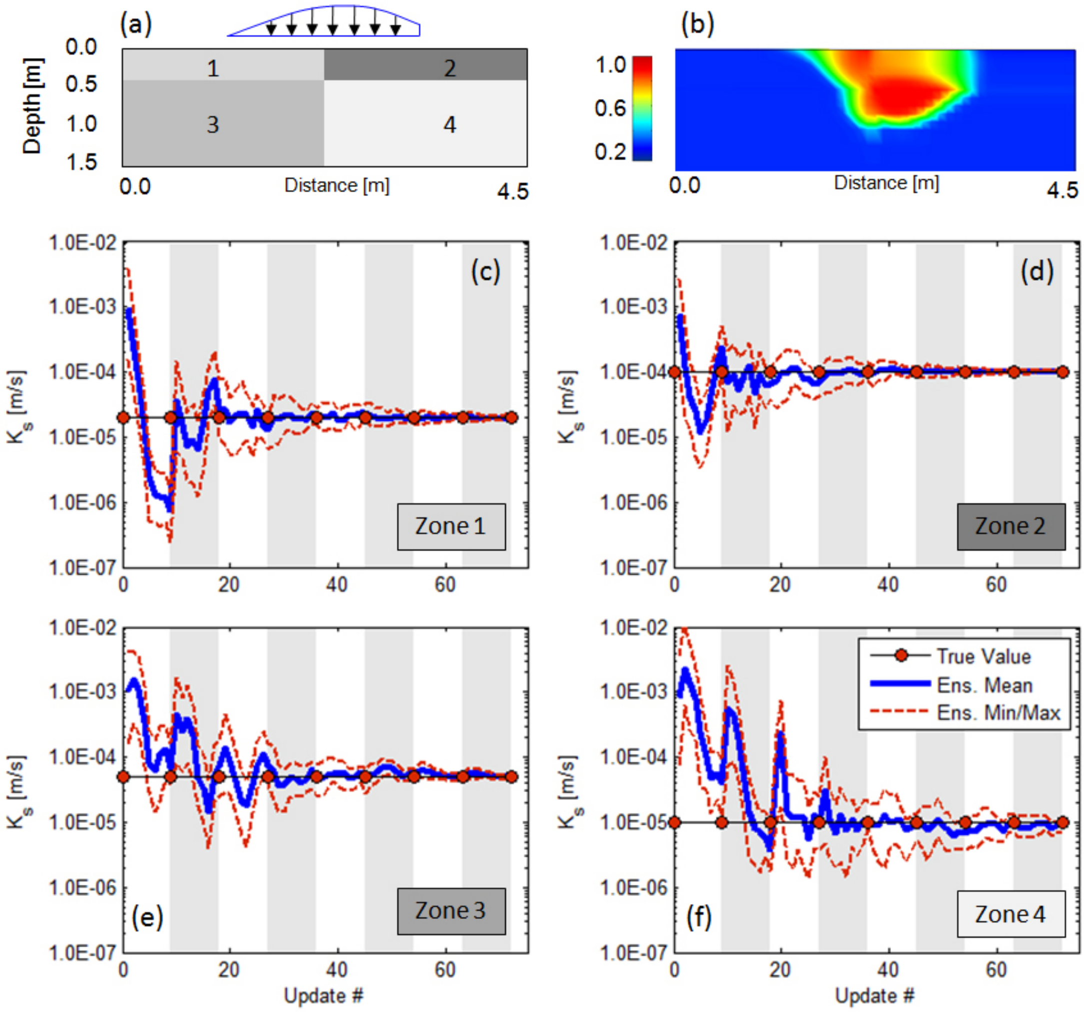

Figure 5.6: Heterogeneous test case results: (a) conceptual model of the model domain (divided into 4 zones with different soil properties) and (b) the simulated soil saturation at $t = 5.5h$. Convergence of the hydraulic conductivities of the four zones is shown in panels c-f. The results are relative to $\sigma_{\Phi} = 5\%$ with randomly perturbed measurements.

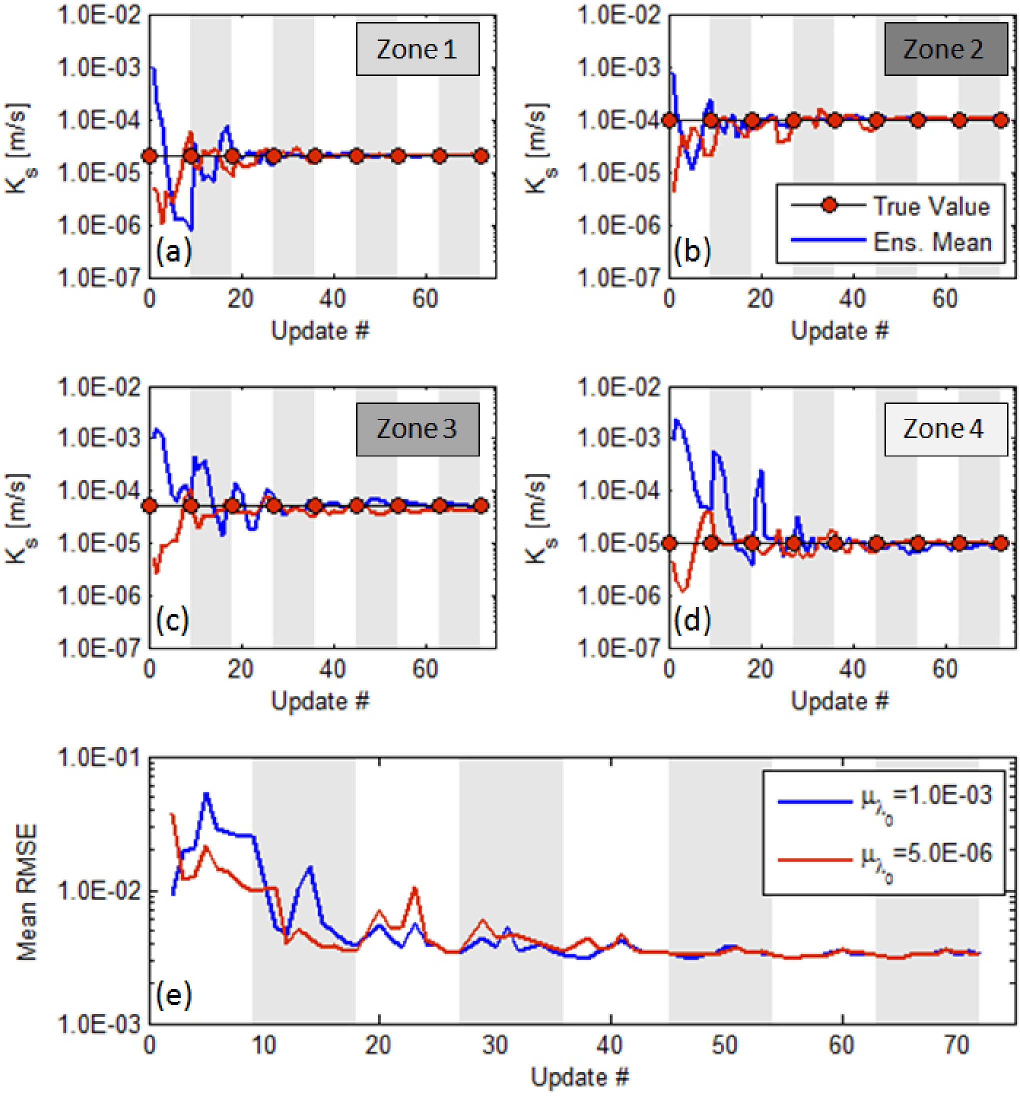

Figure 5.7: Heterogeneous test case results: convergence of the hydraulic conductivities (ensemble mean values) of the four zones (a-d) and mean RMSE (e) for different initial values μ_{λ_0}. The results are relative to $\sigma_\Phi = 5\%$ with randomly perturbed measurements.

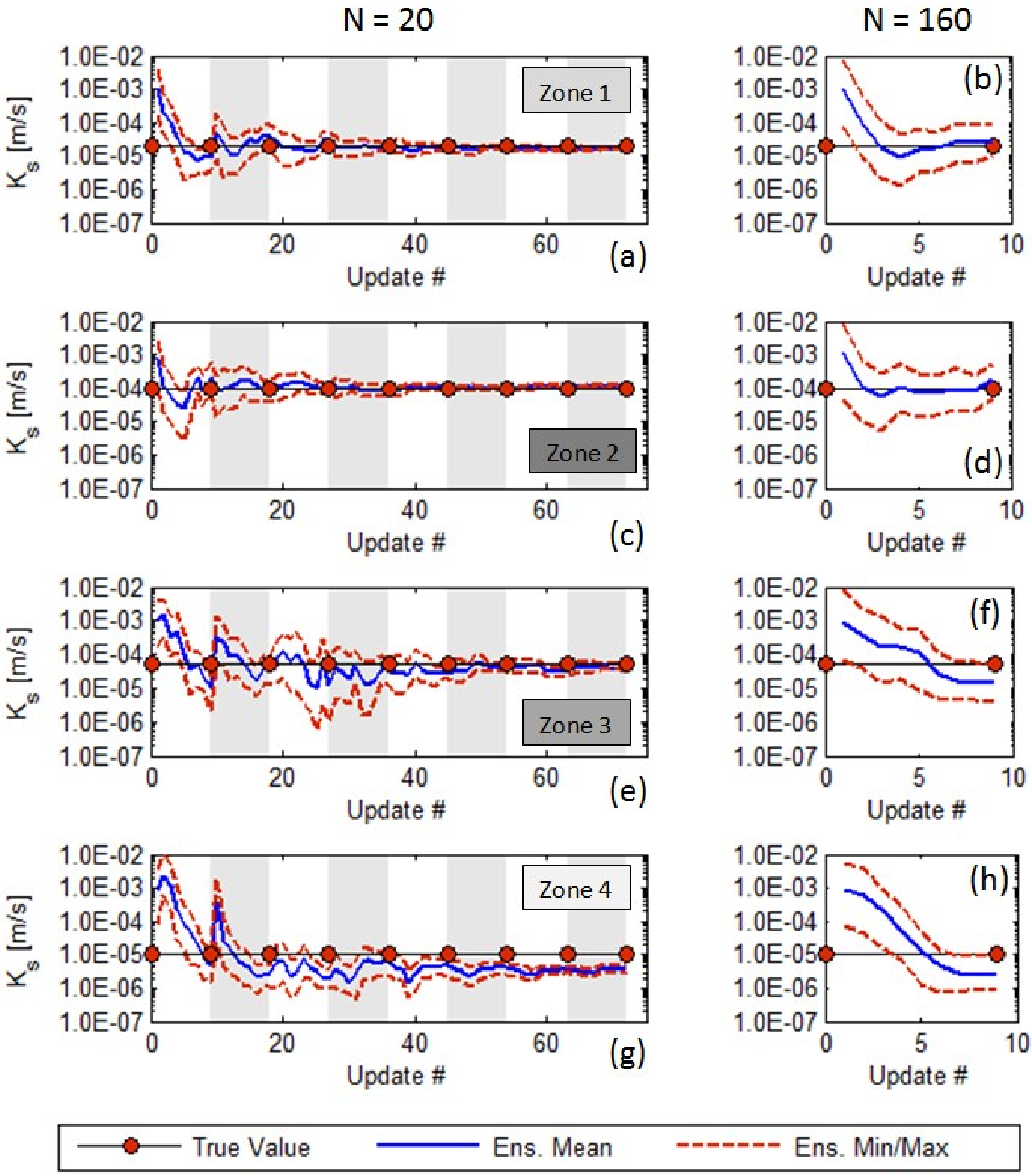

Figure 5.8: Heterogeneous test case results: comparison of the iterative approach ($N = 20$) with a non-iterative simulation with ensemble size $N = 160$. The convergence of the four hydraulic conductivities for the iterative (panels a,c,e,g) and non-iterative (panels b,d,f,h) cases is illustrated (runs with $\sigma_\Phi = 20\%$ and randomly perturbed measurements).

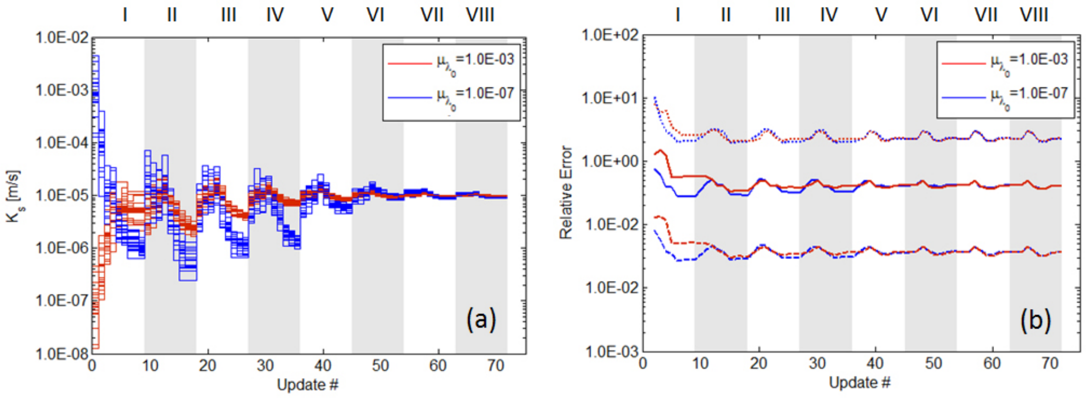

Figure 5.9: Field experiment results: convergence of the hydraulic conductivity (a) and relative errors (b) for different initial values of hydraulic conductivity μ_{λ_0}. The roman numerals at the top of the panels indicate the external iteration count. Mean relative error (ϵ_y), Mean $RMSE_y$ and Maximum Relative error ($\epsilon_{y,max}$) are shown.

20% measurement uncertainty, implying that the inverse procedure has arrived at the correct solution. On the contrary, the results for the non-iterative SIR show a bias in the identification of the parameters of zones 3 and 4. The corresponding ensemble means underestimate the true values, reflecting the earlier observation that starting from a large $\boldsymbol{K}_s$ leads to an underestimation of the parameter value. The final posterior distributions of the parameters have a higher ensemble variance than the corresponding iterative-results, yielding an uncertain characterization of the soil structure. The non-iterative SIR procedure shows a parameter distribution with strong variations during the assimilation, corresponding to a large variance of the posterior distribution.

5.5.2 Field experiment

The results of the field data inversion are shown in Figure 5.9. The assimilation of ERT measurements provides similar results to the synthetic test case, thus confirming the reliability of the method. The iterative particle filter is shown to converge to a value of hydraulic conductivity $\boldsymbol{K}^*$ which is independent to the initial guess μ_{λ_0}. As a matter of fact, starting from $\mu_{\lambda_0} = 10^{-3}$ ms^{-1} the method provides a final estimate $\boldsymbol{K}^* = 8.9 \times 10^{-6} \pm 3.6 \times 10^{-7}$ ms^{-1} and starting from $\mu_{\lambda_0} = 10^{-7}$ ms^{-1}, the final estimate is $\boldsymbol{K}^* = 9.8 \times 10^{-6} \pm 2.9 \times 10^{-7}$ ms^{-1}. Note that in both cases the initial guess is two orders of magnitude away from the final estimate and the two final intervals for the identified parameter value are overlapping. It must be emphasized that the method does not provide just an estimate of hydraulic conductivity but a full probability distribution of the estimate. As shown by the synthetic test, in the case of large measurement noise, the relative errors slightly decrease during the first updates and quickly stabilize. The residual errors are larger than observed in the synthetic test case thus indicating a bias due to external factors not accounted for in the model setup. The hydraulic conductivity estimated by the iterative particle

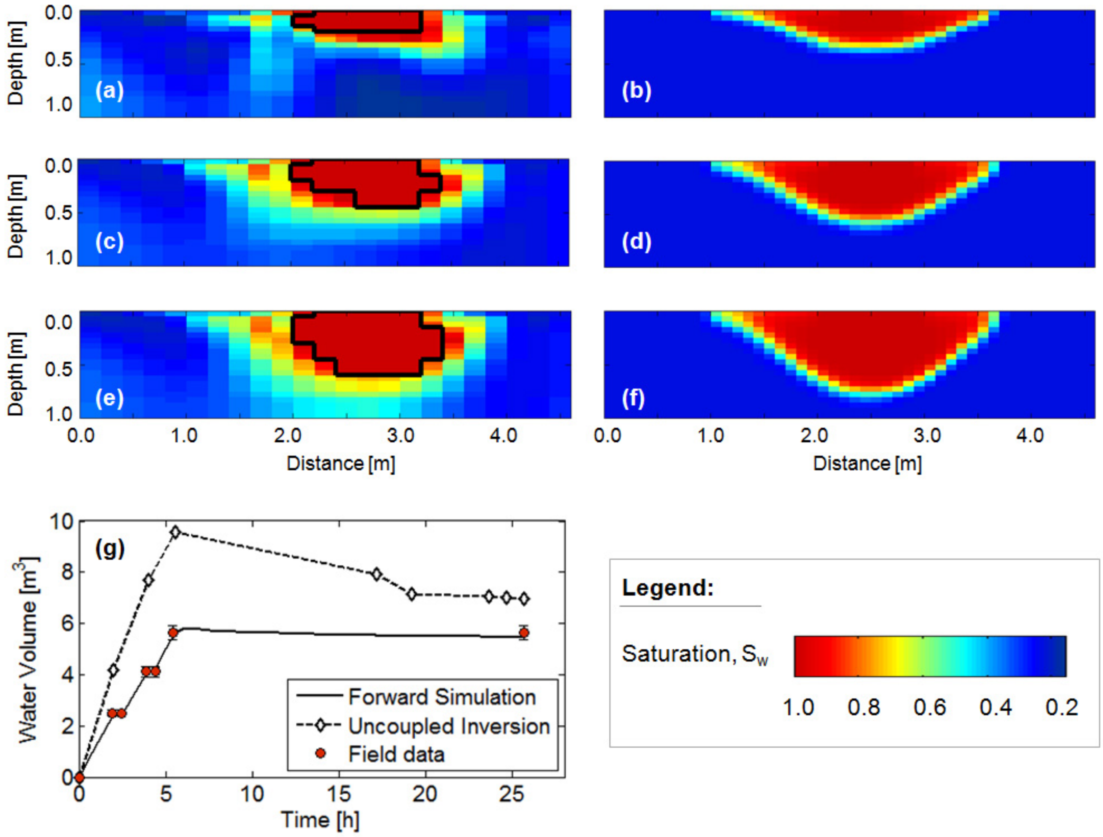

Figure 5.10: Time-lapse soil saturation estimated by uncoupled inversion (a,c,e) and by the forward simulation with the hydraulic conductivity estimated by the coupled approach (b,d,f). The results are shown at (a,b) $t = 2h$, (c,d) $t = 4h$, and (e,f) $t = 5.5h$. The black contour indicates the area where uncoupled inversion provides unphysical saturation estimates ($S_w > 1$). Mass balance (g): the forward simulation (black line) matches the volume of water injected at the site (red circles with a 5% error bar) while the estimate from uncoupled inversion of ERT data overestimates the mass of water in the system.

filter method is shown to converge to the $\boldsymbol{K}^*$ value. However, the reliability of the estimate has to be proven. For this purpose, a forward hydrologic simulation is run with $\boldsymbol{K}_s = \boldsymbol{K}^*$ and the results are compared with field observations (Figure 5.10). The robustness of the estimated parameter is confirmed by the spatial agreement of simulated soil moisture fields obtained by the coupled and uncoupled inversion procedures (Figure 5.10(a-f)) and by the excellent agreement between the amount of injected water and the predicted mass balance (Figure 5.10(g)). Further comparison between the forward simulation and field data are presented in [Rossi et al., 2013] where the simulated infiltration is shown to match the front depth estimated by the GPR survey. The discrepancy between the simulation and the time-lapse saturation estimated by uncoupled inversion increases for increasing front depth. As a matter of fact the resolution of traditional ERT inversion decreases with depth and, given the electrode configuration used in this study, the inverted resistivity is not reliable for depth higher than 1 m. In addition, the conversion of inverted resistivity to soil saturation by Archie's law (calibrated in the lab) provided regions of $S_w > 1$ (black contour in Figure 5.10). Even though these regions can be corrected empirically to ensure a consistent saturation field (according to common practice in geophysical applications anyway) the uncoupled approach over-estimates the total water present in the system at any time (Figure 5.10). Therefore, while the forward simulation provides a full conservation of mass, the traditional inversion approach provides a good qualitative description of the physical process but does not ensure a correct mass balance (Figure 5.10g).

5.6 Discussion

The results presented in this paper demonstrate the accuracy and robustness of the proposed iterative methodology and highlight the weaknesses of both, uncoupled ERT inversion and traditional particle filter applications with ERT data. As shown in Figures 5.3, 5.4, and 5.8 for the synthetic test cases and in Figure 5.9 for the field simulations, a single iteration of the particle filter method does not provide a reliable estimate of the soil hydraulic conductivity. To verify this hypothesis, we use as initial guess the parameter value $\mu_{\lambda_0} = 10^{-3}$ m s^{-1} and then employ the identified parameter μ_{λ_8} estimated at the end of the first iteration to run a forward simulation of the infiltration experiment. In this case, the irrigation intensity is found to be higher than the infiltration capacity, thus leading to surface ponding not observed at the site during the experiment. Therefore, if the particle filter is used to estimate the model parameters without enough updates to ensure convergence, the method may lead to wrong predictions of the system dynamics. The results of our simulations further show that a non-iterative SIR approach with a large ensemble is not fully capable of performing a correct identification, suggesting that the iterative approach is computationally more efficient for solving the problem of interest.

The proposed coupled hydro-geophysical modeling framework presents the following advantages compared to more traditional approaches: (1) a forward geophysical model is used and the inversion of the geophysical data is avoided thus guaranteeing physical consistency with the hydrologic quantities; (2) the sequential approach provides a dynamic correction of the simulated system state, thus correcting intrinsic model errors (i.e. unknown initial condition), with relatively small compuational requirements; (3) the data assimilation approach is particularly interesting for field applications where the geophysical measurements can be affected by external factors (e.g. soil evaporation, a rainfall event during the geophysical survey, etc.) that can be easily included in the hydro-geophysical modeling framework; (4) the filtering approach describes quantitatively both model and observation errors, and provides the probability density functions of both system state and model parameters.

5.7 Conclusions

A sequential Bayesian approach for coupled hydro-geophysical assimilation of ERT measurements in a variably saturated flow model is presented. An innovative iterative approach is proposed to achieve accurate identification of the model parameters. The robustness of the methodology is tested on spatially homogeneous and heterogeneous synthetic test cases and validated on a field infiltration experiment. We show that the new approach has several advantages compared to uncoupled inversion and traditional sequential data assimilation techniques. In particular the iterative particle filter provides accurate parameter estimation as opposed to traditional SIR that may lead to biased results. Further work will focus on testing the methodology for the estimation of multiple and spatially varying parameters (e.g. Archie's law, retention curves, heterogeneous soil, etc.).

6

Summary and Conclusions

This thesis is a contribution to modeling soil-plant-atmosphere interactions and coupled hydro-geophysical data assimilation for eco-hydrological applications. In this chapter the scientific results are summarized highlighting the major achievements and suggesting future research directions.

6.1 Eco-Hydro-Geophysical modeling

Modeling Land-Atmosphere interactions. A mechanistic model for the soil-plant-atmosphere has been developed and applied to different case studies to improve the current understanding of the feedback mechanisms regulating the land-atmosphere system. The soil-plant model is based on a numerical solution to the 3D Richards equation modified to account for a 3D RWU, trunk xylem, and stomatal conductances. The model is used to diagnose plant responses to water stress in the presence of competing rooting systems: the overlap between rooting zones is shown to enhance soil drying but it has been shown that the transpiration-bulk root-zone soil moisture relations do not deviate appreciably from their proto-typical form commonly assumed in eco-hydrology. These results are particularly relevant to account for root competition in common lumped eco-hydrological models.

Given the three-dimensionality of the approach, the model is then applied to a crop field in order to evaluate the impact of land elevation, soil heterogeneities, and seawater contamination on farmland productivity. To this purpose, a crop growth module has been added to the SPA simulator, thus providing an innovative modeling tool for agricultural applications (e.g. precision farming, irrigation system design, etc).

The model is then coupled with a slab representation of the atmospheric boundary layer (ABL) to explore the role of water table fluctuations and free atmospheric (FA) states on predisposition of convective rainfall. Simulation results demonstrated that a reduction in latent heat flux associated with reduced water table levels may enhance the predisposition to convective rainfall. However, when the SPA system is fully coupled with the atmosphere (i.e. accounting for atmospheric temperature and water vapor concentration budgets) plant stress plays a role within a limited range of atmospheric parameters, and a decrease in latent heat flux leads to a suppression of boundary layer clouds. Understanding such complex feedback mechanisms has become a scientific imperative to understand the impact of climate change and human-induced changes on the biosphere. In addition, improving the current understanding of convective rainfall initiation is crucial to improve the reliability of seasonal rainfall forecasts [Koster et al., 2004].

Coupled Hydro-Geophysical Inversion. The use of Electrical Resistivity Tomography to collect indirect information on the hydrological processes occurring in the vadose zone has been also explored. We presented an infiltration experiment monitored by time-lapse ERT and we used a modified Sequential Importance Resampling (SIR) method to assimilate ERT measurements in a coupled hydro-geophysical model. In this dissertation we demonstrated the limitations of the traditional sequential Bayesian approach and we proposed an innovative iterative approach to improve model predictions and estimate the model parameters with high accuracy.

6.2 Challenges for future research

Future research should focus on extending the proposed data assimilation framework to the soil-plant-atmosphere system. As a matter of fact, calibration of soil-plant models requires spatial information on RWU processes and the results presented in this thesis demonstrated that ERT data can be easily used to constrain model predictions.

In addition, thanks to the applicability of the model developed to large scales (from field to the watershed), spatially explicit measurements of plant variables (e.g. the crop yield data illustrated in Chapter 3) can be used as observations to update the hydrological simulation and estimate the soil parameters.

Acknowledgments

This study was supported by the University of Padova, Italy, within the Research Program "GEO-RISKS: Geological, morphological and hydrological processes: monitoring, modeling and impact in the north-eastern Italy", WP4. Additional support for the work at Duke University, North Carolina (USA), was provided by "Fondazione Ing. Aldo Gini" (Italy).

A Appendix

A.1 Soil-Plant Model

A.1.1 Additional model equations

Soil-root system The water flux from the soil to the plant root is derived from the energy (E) balance:

$$E = \psi_i + z_i = \psi_R + z_R + \Delta E_i + \Delta E_r \tag{A.1}$$

where ΔE_i and ΔE_r are the energy losses associated with water entering the root membrane and reaching the trunk. Assuming that energy losses within the root system are negligible when compared to the energy losses across the membrane, i.e. $\Delta E_r << E_i$, and $\Delta E_i = q_i/g_i$, from Eq. (A.1) it follows that an expression for q_i can be derived and given by:

$$q_{i,j} = -g_{i,j}\left[(\psi_{R,j} + z_{R,j}) - (\psi_i + z_i)\right] a_{R,i}, \tag{A.2}$$

where $a_{R,i}$ is the total root surface area per unit soil volume introduced to obtain a flux per unit volume (see main text).

Xylem-Leaf system The vulnerability curve (the vulnerability of xylem to cavitation) provides the value of g_x (per unit ground area) as a function of the leaf water potential as ψ_L [Daly et al., 2004]:

$$g_x(\psi_L) = g_{x,max} exp\left[-\left(-\frac{\psi_L}{d}\right)^c\right] \tag{A.3}$$

The cost parameter λ, i.e. the cost of water for the plant to complete the photosynthesis, can be estimated from the leaf water potential ψ_L according to equation [Manzoni et al., 2011]:

$$\lambda(\psi_L) = \lambda^*_{max}\frac{c_a}{c^*_a} exp[-\beta(< \psi_L > -\psi_{L,max})^2],$$

where λ^*_{max} is the maximum λ at a reference $c_a = c^*_a = 400ppm$, β is a fitting parameter, $\psi_{L,max}$ is the leaf water potential at λ^*_{max} and $< \psi_L >$ is the average value of ψ_L over a time period that must be much longer than the time scale over which stomatal conductance varies. Here, the previous 24 hour period is selected as an averaging period so as to ensure that λ varies on time scales much longer than diurnal [Volpe et al., 2013]).

A.1.2 Model implementation

Eq. (5.9) is solved numerically using the linear tetrahedral finite element method with backward Euler scheme for the time discretization. The resulting system of ODEs can be written as follows:

$$\begin{aligned} \left(H^{k+1} + \frac{P^{k+1}}{\Delta t_k}\right)\mathbf{\Psi}^{k+1} &= \frac{P^{k+1}}{\Delta t_k}\mathbf{\Psi}^{k} - \mathbf{q}(\mathbf{\Psi}^{k+1}, \mathbf{\Psi}_L) && \text{(A.4)} \\ \mathbf{G}(\mathbf{\Psi}^{k}, \mathbf{\Psi}_L) &= 0 && \text{(A.5)} \end{aligned}$$

where $\mathbf{\Psi} \in \mathbf{R}^n$ and $\mathbf{\Psi}_L \in \mathbf{R}^p$ being n and p the number of grid nodes and the number of plants respectively. The non-linear system described in Eq.(A.4) is solved using the Picard iteration Paniconi and Putti [1994]:

$$\left(H^{k+1,m} + \frac{P^{k+1,m}}{\Delta t_k}\right)\mathbf{s}^m = -\mathbf{g}(\mathbf{\Psi}^{k+1,m}, \mathbf{\Psi}_L) \tag{A.6}$$

where $\mathbf{s}^m = \mathbf{\Psi}^{k+1,m+1} - \mathbf{\Psi}^{k+1,m}$ and Paniconi and Putti [1994]:

$$\mathbf{g}(\mathbf{\Psi}^{k+1}, \mathbf{\Psi}_L) = H^{k+1}\mathbf{\Psi}^{k+1} + \frac{P^{k+1}}{\Delta t_k}(\mathbf{\Psi}^{k+1} - \mathbf{\Psi}^{k}) - \mathbf{q}(\mathbf{\Psi}^{k+1}, \mathbf{\Psi}_L) \tag{A.7}$$

The value of $\mathbf{\Psi}_L = \{\psi_{L,j}\}_{j=1,p}$ is evaluated from Eq. (A.5) at every Picard iteration by the secant method:

$$\psi^{n+1}_{L,j} = \psi^{n}_{L,j} - G_j(\mathbf{\Psi}^{k,m}, \psi^{n}_{L,j})\frac{\psi^{n}_{L,j} - \psi^{n-1}_{L,j}}{G_j(\mathbf{\Psi}^{k,m}, \psi^{n}_{L,j}) - G_j(\mathbf{\Psi}^{k,m}, \psi^{n-1}_{L,j})} \tag{A.8}$$

where G_j is defined by Eq.(4.12) in the main text. The two initial values $\psi^0_{L,j}$ and $\psi^1_{L,j}$ are chosen from the range of physical values for the leaf water potential ($-10 < \psi_{L,j} < 0$ MPa) ensuring that $G_j(\mathbf{\Psi}^{k,m}, \psi^0_{L,j}) \cdot G_j(\mathbf{\Psi}^{k,m}, \psi^1_{L,j}) < 0$. When no roots exists, the value of $\psi_{L,j}$ that minimizes G_j is assumed as the solution. Since the function $G_j(\mathbf{\Psi}, \psi_{L,j})$ may have multiple unphysical roots, the secant method has been preferred to other more efficient algorithms (e.g. Newton Raphson). Furher details on the numerical implementation of the Richards equation (CATHY model) can be found in Camporese et al. [2010], Paniconi and Putti [1994].

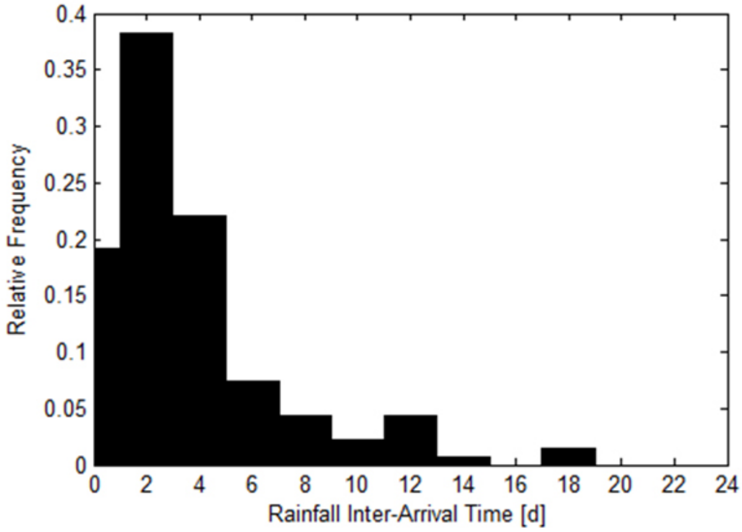

Figure A.1: Relative frequency of rainfall inter-arrival times based on measured rainfall collected at the site during years 2007-2008.

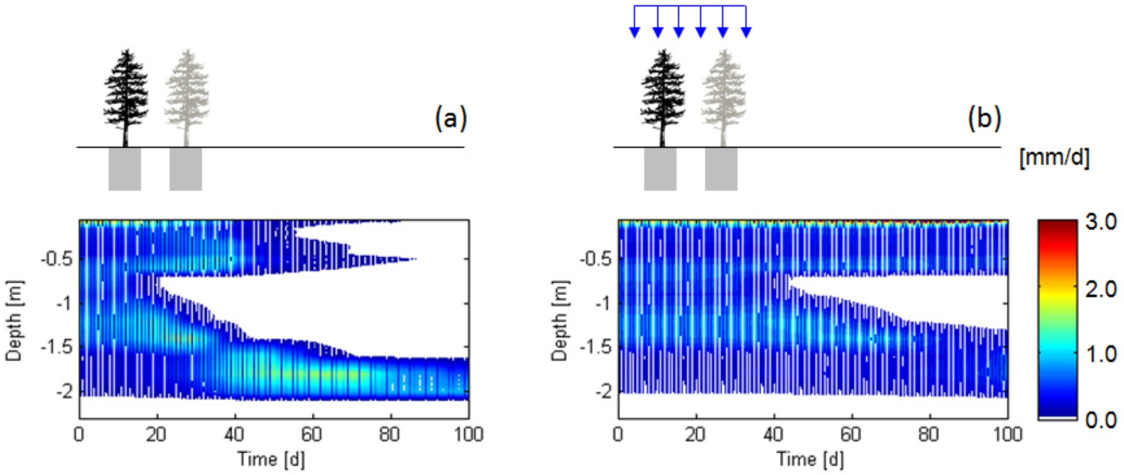

Figure A.2: Effect of rainfall on RWU of tree T1 ($D = 1m$).

A.2 Additional Results

A.2.1 Soil-Plant Model

Additional results are presented in Figures A.1 - A.4. First the relative frequency of rainfall inter-arrival times observed at the site is illustrated (Fig. A.1). Rainfall events generally occur every 2-6 days but dry periods of up to 18 days are also recorded in this 2-year period. The effect of rainfall during the simulated dry-down experiment is also investigated (Fig. A.2). The simulation was run setting a constant

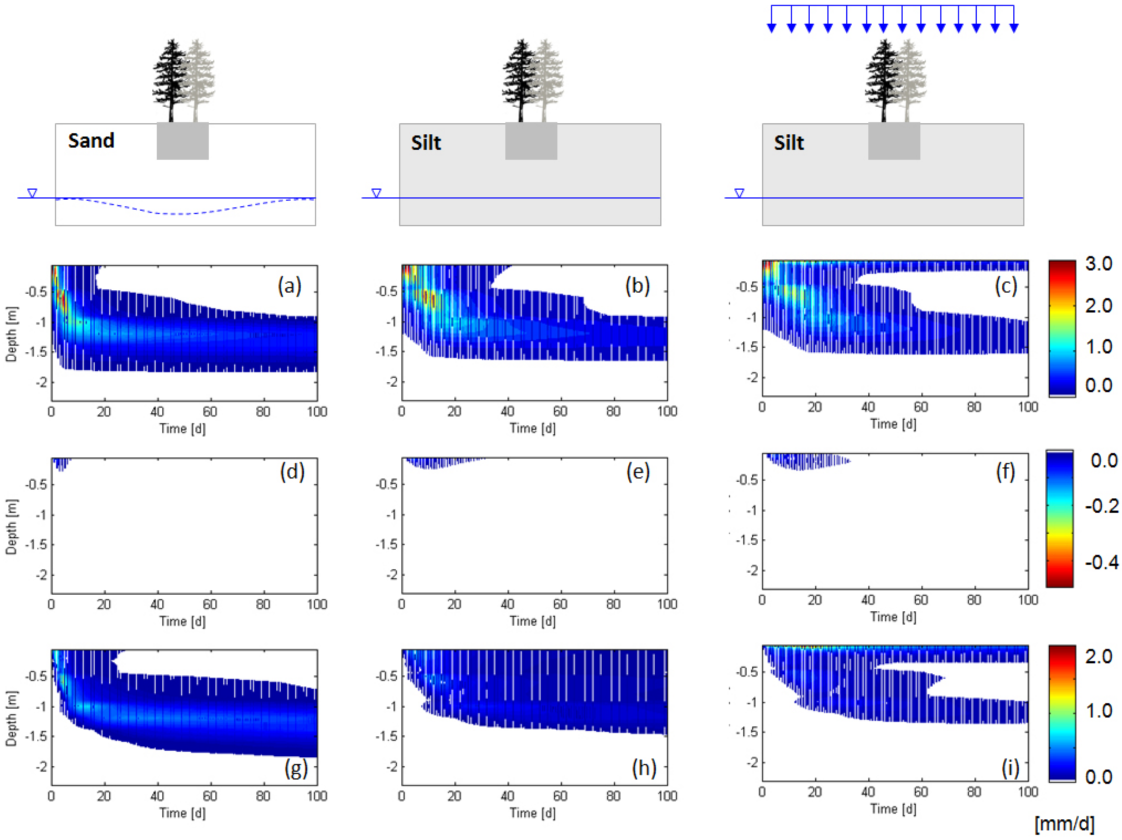

Figure A.3: Water fluxes in the root zone of tree T1 ($D = -1.5$): modeled (a,b,c) RWU, (d,e,f) HR and (g,h,i) Darcy's flux divergence as a function of depth for the case of sandy soil (left panels), silty soil (central panels) and silty soil with constant rainfall (right panels).

flux of 1 mm/d on the top boundary of the domain. The results demonstrate that rainfall provides available water on the top soil and RWU is thus sustained during the drying cycle. Since the simulations are based on a layered soil, additional simulations were performed with homogeneous soil properties (Fig. A.3). The case of sandy and silty soils were explored using an exponential root distribution (see main text for details). The results in Fig. A.4 demonstrate that both soil hydraulic properties and rainfall modify the dynamics of the system. As expected, the transition to stress conditions is faster in the case of sandy soil compared to silt. Due to the difference in the soil water retention curves, the soil saturation-RWU relation varies with the soil type as expected. Rainfall is shown to delay water stress (because the imposed rainfall flux is lower than daily transpiration) shifting the stress response function to drier soil conditions (Fig. A.4a).

A.2.2 Atmospheric Model

Additional model results are presented in Figures A.5 - A.7. First modeled and observed surface energy fluxes are compared (Fig. A.5). The ability of the model

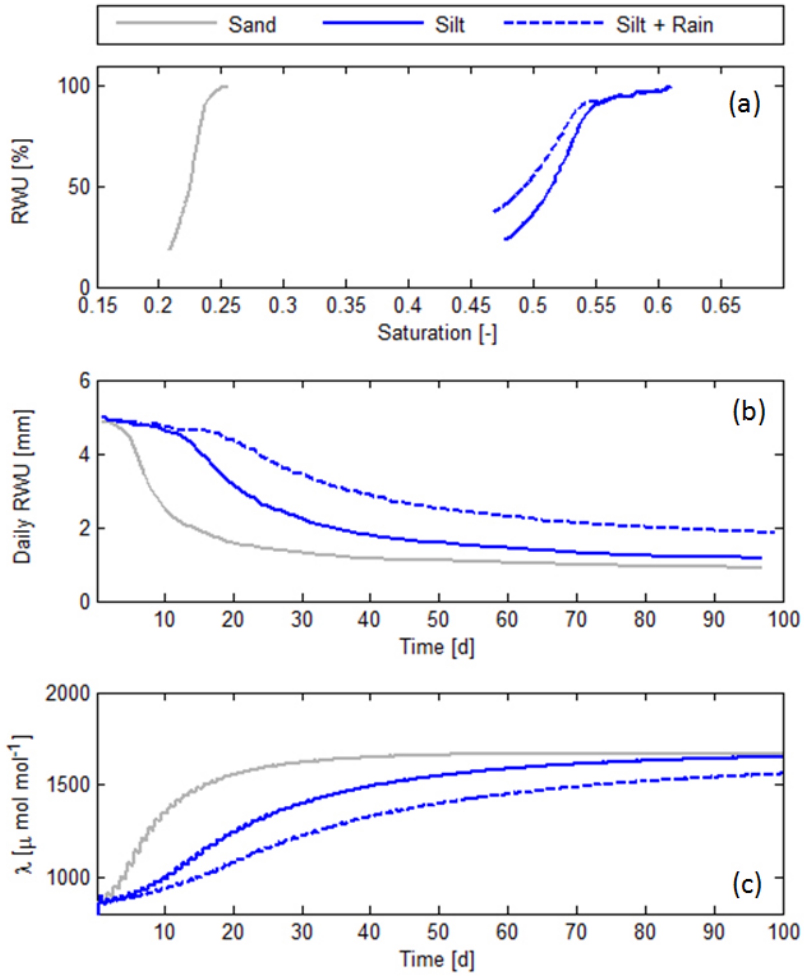

Figure A.4: Transpiration dynamics of tree T1 ($D = -1.5$): (a) relative RWU as a function of average soil moisture, (b) daily RWU, and (c) λ for different simulation scenarios (sandy soil, silty soil and silty soil with constant rainfall).

to simulate ABL and LCL dynamics is also demonstrated (Fig. A.6). An example of simulation results by the fully coupled SPA model is the illustrated (Fig. A.7).

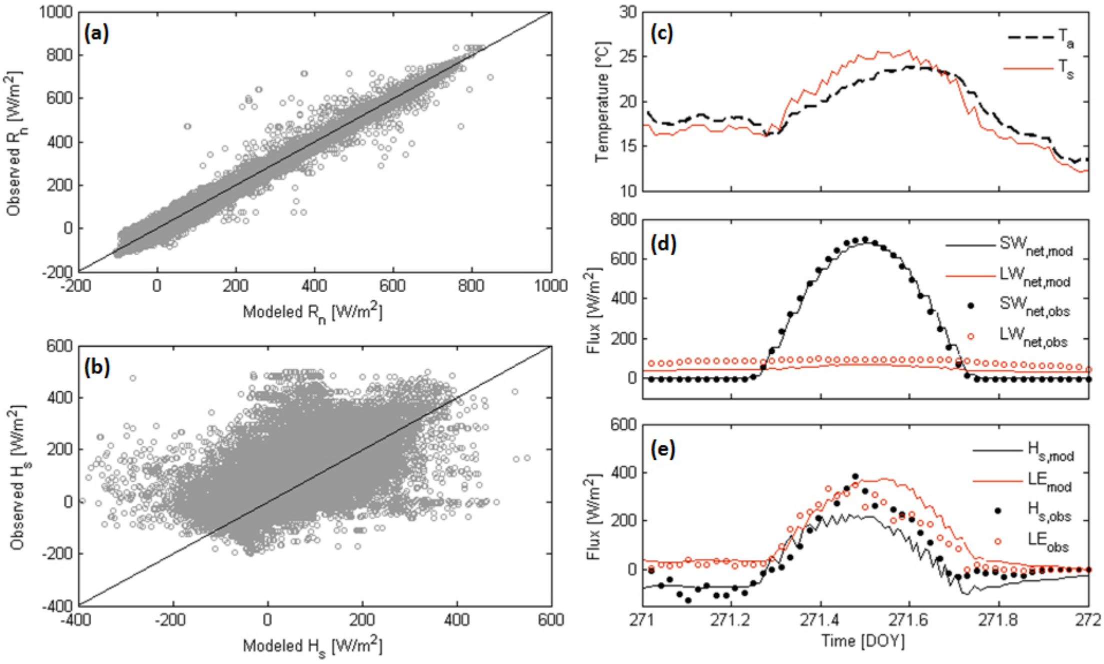

Figure A.5: Model testing: comparison of modeled and observed net radiation (a) and sensible heat flux (b). Daily dynamics of air and canopy temperature (c), net short and long wave radiation (d), sensible heat and latent heat fluxes (e) are shown and compared with observations.

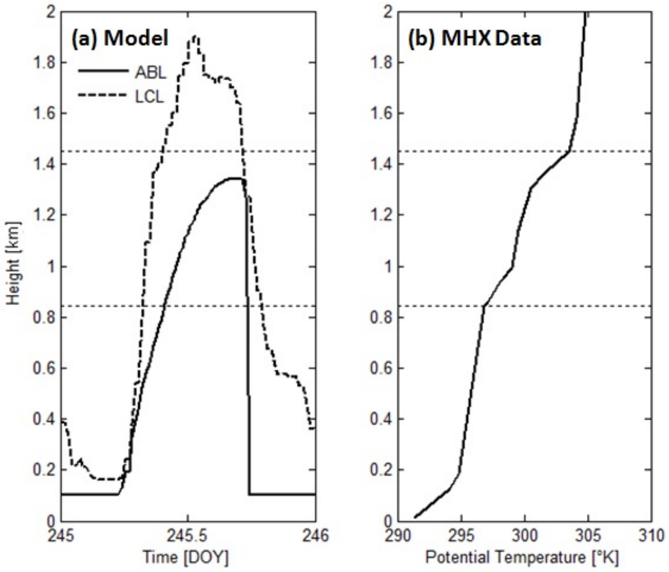

Figure A.6: (a) Evolution of modeled ABL and LCL profiles during DOY 245 (year 2007) compared with the (b) observed ABL heigth estimated from the potential temperature profile recorded at a nearby airport (MHX). The jump in potential temperature observed in panel (b) represents the approximate ABL height.

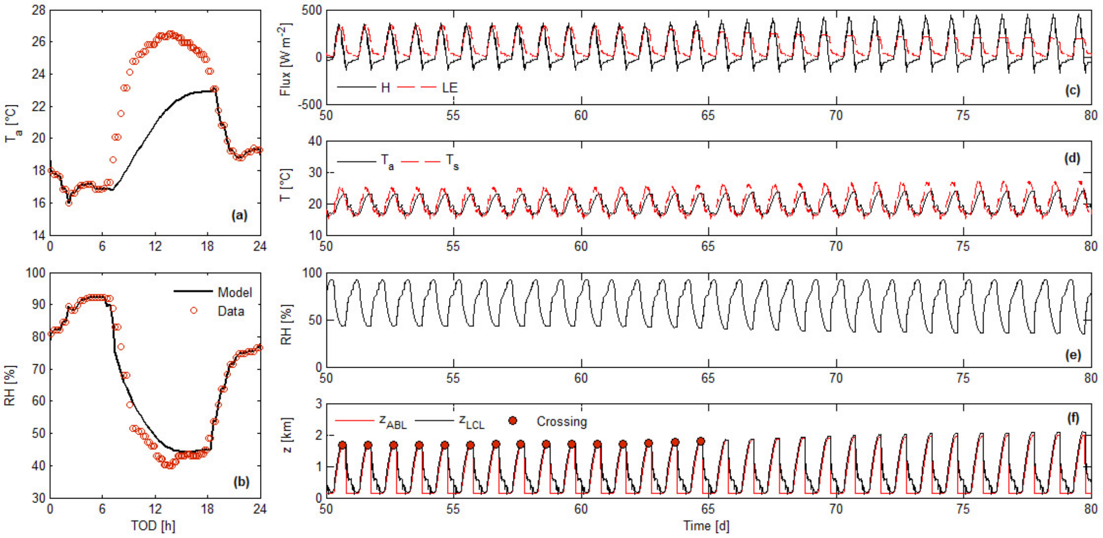

Figure A.7: Comparison between modeled and measured Air Temperature Ta (a) and Relative Humidity RH (b) on 2nd September (DOY 245) 2007. Example of fully coupled model results with water table depth fixed to 2.5 m and a humidity lapse rate equal to -2.5E-6 kg/kg/m: (c) Sensible heat flux Hs and Latent heat flux LE; (d) Air Temperature Ta and Canopy Temperature Ts; (e) Relative Humidity RH; (f) ABL and LCL heights and their crossing.

Bibliography

Allen, R. G., Pereira, L. S., Raes, D., and Smith, M. (1998). Crop evapotranspiration: Guidelines for computing crop requirements. Irrigation and drainage. Paper No. 56. Technical report, FAO, Rome, Italy.

Amenu, G. G. and Kumar, P. (2008). A model for hydraulic redistribution incorporating coupled soil-root moisture transport. *Hydrol. Earth Syst. Sci.*, 12:55–74.

Anderegg, W. R. L., Kane, J. M., and Anderegg, L. D. L. (2013). Consequences of widespread tree mortality triggered by drought and temperature stress. *Nature Clim. Change*, 3:30–36.

Archie, G. E. (1942). The electrical resistivity log as an aid in determining some reservoir characteristics. *Trans. Am. Inst. Min. Metall. Eng.*, 146:54–61.

Arulampalam, M. S. and Ristic, B. (2000). Comparison of the particle filter with range-parametrized and modified polar EKFs for angle-only tracking. In *Proc. SPIE*, volume 4048, pages 288–299.

Aspinwall, M. J., King, J. S., Domec, J. C., McKeand, S. E., and Isik, F. (2011). Genetic effects on transpiration, canopy conductance, stomatal sensitivity to vapour pressure deficit, and cavitation resistance in loblolly pine. 4:168–182.

Baudena, M., Bevilacqua, I., Canone, D., Ferraris, S., Previati, M., and Provenzale, A. (2012). Soil water dynamics at a midlatitude test site: Field measurements and box modeling approaches. *J. Hydrol.*, 414-415:329–340.

Bergamaschi, L., Bru, R., Martnez, A., Mas, J., and Putti, M. (2013). Low-rank update of preconditioners for the nonlinear Richards equation. *Math. Comput. Model.*, 57(7-8):1933–1941.

Bergamaschi, L., Bru, R., Martnez, A., and Putti, M. (2006). Quasi-newton preconditioners for the inexact Newton method. *Electron. Trans. Numer. Anal.*, 23:76–87.

Binley, A. and Kemma, A. (2005). Electrical methods. In Rubin, Y. and Hubbard, S. S., editors, *Hydrogeophysics*, volume 50, pages 129–156. Springer.

Boaga, J., Rossi, M., and Cassiani, G. (2013). Monitoring soil-plant interactions in an apple orchard using 3d electrical resistivity tomography. *Procedia Environ. Sci.*, 19:394–402.

Bonan, G. B. (2008). Forests and climate change: Forcings, feedbacks, and the climate benefits of forests. *Science*, 320:1444–1449.

Bonetti, S., Manoli, G., Domec, J. C., Putti, M., Marani, M., and Katul, G. (2013). The role of water table fluctuations and the free atmospheric state on convective rainfall initiation. *Submitted.*

Braga, F., Morari, F., Rizzetto, F., Scudiero, E., Teatini, P., Tosi, L., and Xing, Q. (2012). Characterizing the saltwater effect on soil productivity by WorldView-2 images. The southern margin of the Venice Lagoon, Italy. In *7th EUREGEO, European Congress on Regional Geoscientific Cartography and Information Systems*, volume 1, pages 361–362. S. Scappini and S. Zapparoli eds., Centro Stampa Regione Emilia-Romagna Publ.

Brovelli, A. and Cassiani, G. (2011). Combined estimation of effective electrical conductivity and permittivity for soil monitoring. *Water Resour. Res.*, 47:W08510.

Brovelli, A., Cassiani, G., Dalla, E., Bergamini, F., Pitea, D., and Binley, A. M. (2005). Electrical properties of partially saturated sandstones: a novel computational approach with hydro-geophysical applications. *Water Resour. Res.*, 41(8):W08411.

Brutsaert, W. (1975). On a Derivable Formula for Long-Wave Radiation from Clear Skies. *Water Resour. Res.*, 11:742–744.

Caldwell, M. M. and Richards, J. H. (1989). Hydraulic lift: Water efflux from upper roots improves effectiveness of water uptake by deep roots. *Oecologia*, 79:1–5.

Campbell, G. S. and Norman, J. M. (2000). *An Introduction to Environmental Biophysics*. Springer, New York.

Camporese, M., Paniconi, C., Putti, M., and Orlandini, S. (2010). Surface-subsurface flow modeling with path-based runoff routing, boundary condition-based coupling, and assimilation of multisource observation data. *Water Resour. Res.*, 46:W02512.

Camporese, M., Paniconi, C., Putti, M., and Salandin, P. (2009a). Comparison of data assimilation techniques for a coupled model of surface and subsurface flow. *Vadose Zone J.*, 8(4):837–845.

Camporese, M., Paniconi, C., Putti, M., and Salandin, P. (2009b). Ensemble Kalman filter data assimilation for a process-based catchment scale model of surface and subsurface flow. *Water Resour. Res.*, 45:W10421.

Canone, D., Ferraris, S., Sander, G., and Haverkamp, R. (2008). Interpretation of water retention field measurements in relation to hysteresis phenomena. *Water Resour. Res.*, 44(4):W00D12.

Cassiani, G., Giustianini, M., Ferraris, S., Deiana, R., and Strobbia, C. (2009a). Time-lapse surface-to-surface gpr measurements to monitor a controlled infiltration experiment. *Bollettino di Geofisica Teorica ed Apllicata*, 50(2):209–226.

Cassiani, G., Kemna, A., Villa, A., and Zimmermann, E. (2009b). Spectral induced polarization for the characterization of free-phase hydrocarbon contamination of sediments with low clay content. *Near Surf. Geophys.*, 7(5-6):547562.

Cassiani, G., Ursino, N., Deiana, R., Vignoli, G., Boaga, J., Rossi, M., Perri, M. T., Blaschek, M., Duttmann, R., Meyer, S., Ludwig, R., Soddu, A., Dietrich, P., and Werban, U. (2012). Non-invasive monitoring of soil static characteristics and dynamic states: a case study highlighting vegetation effects. *Vadose Zone J.*, 11:vzj2011.0195.

Chagnon, F. and Bras, R. L. (2005). Contemporary climate change in the amazon. 32:L13703.

Chung, E., Chan, T., and Tai, X. (2005). Electrical impedance tomography using level set representations and total variation regularizationa. *J. Comp. Phys.*, 205:357–372.

Clark, C. A. and Arritt, R. W. (1995). Numerical simulations of the effect of soil moisture and vegetation cover on the development of deep convection. *J. Appl. Meteorol.*, 34:2029–2045.

Couvreur, V., Vanderborght, J., and Javaux, M. (2012). A simple three-dimensional macroscopic root water uptake model based on the hydraulic architecture approach. *Hydrol. Earth Syst. Sci.*, 16:2957–2971.

Daily, W., Ramirez, A., La Brecque, D. J., and Nitao, J. (1992). Electrical resistivity tomography of vadose zone water movement. *Water Resour. Res.*, 28(5):1429–1442.

Daly, C., Bachelet, D., Lenihan, J. M., Neilson, R. P., Parton, W., and Ojima, D. (2000). Dynamic simulation of tree-grass interactions for global changes studies. *Ecological Applications*, 10:449–469.

Daly, E., Porporato, A., and Rodriguez-Iturbe, I. (2004). Coupled dynamics of photosynthesis, transpiration, and soil water balance. Part i: Upscaling from hourly to daily level. *J. Hydrometeorol.*, 5:546–558.

daRocha, H. R., Nobre, C. A., Bonatti, J. P., Wright, I. R., and Sellers, P. J. (1996). A vegetation atmosphere interaction study for amazonia deforestation using field data and a single column model. *Q. J. Roy. Meteor. Soc.*, 122:567–594.

de Arellano, J. V. G., van Heerwaarden, C. C., and Lelieveld, J. (2012). Modelled suppression of boundary-layer clouds by plants in a CO_2-rich atmosphere. *Nature Geoscience*, 5:701–704.

Diggs, J. (2004). Hydrology and nitrogen loading of forested fields in a coastal plain watershed. Master's thesis, North Carolina State University, Raleigh, NC, USA.

Dirmeyer, P. A., Koster, R. D., and Guo, Z. (2006). Do global models properly represent the feedback between land and atmosphere? *J. Hydrometeorol.*, 7:1177–1198.

Domec, J. C., King, J. S., Noormets, A., Treasure, E., Gavazzi, M. J., Sun, G., and McNulty, S. G. (2010). Hydraulic redistribution of soil water by roots affects whole-stand evapotranspiration and net ecosystem carbon exchange. *New Phytol.*, 187:171–183.

Domec, J. C., Ogée, J., Noormets, A., Jouangy, J., Gavazzi, M. J., Treasure, E., Sun, G., McNulty, S. G., and King, J. S. (2012). Interactive effects of nocturnal transpiration and climate change on the root hydraulic redistribution and carbon and water budgets of southern United States pine plantations. *Tree Phys.*, 32:707–723.

Doucet, A., Godsill, S., and Andrieu, C. (2000). On sequential Monte Carlo sampling methods for Bayesian filtering. *Stat. Comput.*, 10(3):197–208.

Doussan, C., Pierret, A., Garrigues, E., and Pages, L. (2006). Water uptake by plant roots: Ii Modelling of water transfer in the soil rootsystem with explicit account of flow within the root system Comparison with experiments. *Plant Soil*, 283:99–117.

Dowd, M. (2007). Bayesian statistical data assimilation for ecosystem models using Markov Chain Monte Carlo. *J. Marine Syst.*, 68(4-3):439–456.

Eagleson, P. S. (1978). Climate, soil and vegetation. 1. Introduction to water balance dynamics. *Water Resour. Res.*, 14:705–712.

Evensen, G. (2003). The ensemble Kalman filter: theoretical formulation and practical implementation. *Ocean Dyn.*, 53(4):343–367.

Farquhar, G. D., von Caemmerer, S., and Berry, J. A. (1980). A Biochemical Model of Photosynthetic CO_2 Assimilation in Leaves of C_3 Species. *Planta*, 149:78–90.

Feddes, R., Kowalik, P., and Zaradny, H. (1978). Simulation on of field water use and crop yield. Technical report, Centre for Agricultural Publishing and Documentaion, Wageningen, the Netherlands.

Findell, K. L.and Eltahir, E. A. B. (2003). Atmospheric controls on soil moisture-boundary layer interactions. part ii: Feedbacks within the continental united states. *J. Hydrometeorol.*, 4:570–583.

Garré, S., Javaux, M., Vanderborght, J., Pagès, and Vereecken, H. (2011). Three-dimensional electrical resistivity tomography to monitor root zone water dynamics. *Vadose Zone J.*, 10:412–424.

Gauthier, P., Courtier R, P., and Moll, P. (1993). Assimilation of simulated wind lidar data with a Kalman filter. *Mon. Weather Rev.*, 121(6):1803–1820.

Gordon, N. J., Salmond, D. J., and Smith, A. F. M. (1993). Novel approach to nonlinear/non-Gaussian Bayesian state estimation. *IEE Proc.-F*, 140(2):107–113.

Green, S. R., Kirkham, M. B., and E., C. B. (2006). Root uptake and transpiration: from measurements and models to sustainable irrigation. *Agric. Water Manage.*, 86:140–149.

Ha, T., Pyun, S., and Shin, C. (2006). Efficient electric resistivity inversion using adjoint state of mixed finite-element method for Poissons equation. *J. Comp. Phys.*, 214:171–186.

Hansen, G. A. and Penland, C. (2007). On stochastic parameter estimation using data assimilation. *Physica D*, 230:88–98.

Hendricks Franssen, H.-J. and Kinzelbach, W. (2008). Real-time groundwater flow modeling with the ensemble Kalman filter: Joint estimation of states and parameters and the filter inbreeding problem. *Water Resour. Res.*, 44(9):W09408.

Hinnell, A. C., Ferré, T. P. A., Vrugt, J. A., Huisman, J. A., Moysey, S., Rings, J., and Kowalsky, M. (2010). Improved extraction of hydrologic information from geophysical data through coupled hydrogeophysical inversion. *Water Resour. Res.*, 46:W00D40.

Hsu, K. L., Moradkhani, H., and Sorooshian, S. (2009). A sequential Bayesian approach for hydrologic model selection and prediction. *Water Resour. Res.*, 45(12):W00B12.

Huxman, T. E., Wilcox, B. P., Breshears, D. D., Scott, R. L., Snyder, K. A., Small, E. E., Hultine, K., Pockman, W. T., and Jackson, R. B. (2005). Ecohydrological implications of woody plant encroachment. *Ecology*, 86:308–319.

Ivanov, V. Y., Bras, R. L., and Vivoni, E. R. (2008). Vegetation-hydrology dynamics in complex terrain of semiarid areas: 1. a mechanistic approach to modeling dynamic feedbacks. *Water Resour. Res.*, 44:W03429.

Jarvis, N. J. (1994). The MACRO model (Version 3.1), technical description and sample simulations. reports and dissertaions 19. Technical report, Dep. Soil Sci., Swedish Univ. Agric. Sci, Uppsala, Sweden.

Javaux, M., Schröder, T., Vanderborght, J., and Vereecken, H. (2008). Use of a Three-Dimensional Detailed Modeling Approach for Predicting Root Water Uptake. *Vadose Zone J.*, 7:1079–1088.

Jazwinski, A. H. (1970). *Stochastic Processes and Filtering Theory.* Academic Press, New York.

Juang, J. Y., Porporato, A., Stoy, P. C., Siqueira, M. S., Oishi, A. C., Detto, M., Kim, H. S., and Katul, G. (2007). Hydrologic and atmospheric controls on initiation of convective precipitation events. *Water Resour. Res.*, 43:W03421.

Jury, W. A., Or, D., Pachepsky, Y., Vereecken, H., Hopmans, J. W., Ahuja, L. R., Clothier, B. E., Bristow, K. L., Kluitenberg, G. J., Moldrup, P., Šimůnek, J., van Genuchten, M. T., and Horton, R. (2011). Kirkham's Legacy and Contemporary Challenges in Soil Physics Research. *Soil Sci. Soc. Amer. J.*, 75:1589–1601.

Kalbacher, T., Schneider, C. L., Wang, W., Hildebrandt, A., Attinger, S., and Kolditz, O. (2011). Modeling soil-coupled water uptake of multiple root system with automatic time stepping. *Vadose Zone J.*, 10:727–735.

Katul, G., Manzoni, S., Palmroth, S., and Oren, R. (2010). A stomatal optimization theory to describe the effects of atmospheric CO_2 on leaf photosynthesis and transpiration. *Annals of Botany*, 105:431–442.

Katul, G., Oren, R., Manzoni, S., Higgins, C., and Perlange, M. B. (2012). Evapotranspiration: a process driving mass transport and energy exchage in the soil-plant-atmosphere-climate system. *Rev. Geophys.*, 50:RG3002.

Konings, A. G., Katul, G., and Porporato, A. (2010). The rainfall-no rainfall transition in a coupled land convective atmosphere system. 37:L14401.

Koster, R. D., Dirmeyer, P. A., Guo, Z., Bonan, G., Chan, E., Cox, P., Gordon, C. T., Kanae, S., Kowalczyk, E., Lawrence, D., Liu, P., Lu, C.-H., Malyshev, S., McAvaney, B., Mitchell, K., Mocko, D., Oki, T., Oleson, K., Pitman, A., Sud, Y. C., Taylor, C. M., Verseghy, D., Vasic, R., Xue, Y., and Yamada, T. (2004). Regions of strong coupling between soil moisture and precipitation. 305:1138–1140.

Kuhlmann, A., Neuweiler, I., van der Zee, S. E. A. T. M., and Helmig, R. (2012). Influence of soil structure and root water uptake strategy on unsaturated flow in heterogeneous media. *Water Resour. Res.*, 48:W02534.

Laio, F., Porporato, A., Ridolfi, L., and Rodriguez-Iturbe, I. (2001). Plants in water-controlled ecosystems: active role in hydrologic processes and response to water stress. II. Probabilistic soil moisture dynamics. *Adv. Water Resources*, 24:707–723.

Manoli, G., Bonetti, S., Domec, J. C., Putti, M., Katul, G., and Marani, M. (2013a). Tree root systems competing for soil moisture in a 3d soil-plant model. *Submitted.*

Manoli, G., Bonetti, S., Scudiero, E., Teatini, P., Binning, P. J., Morari, F., Putti, M., and Marani, M. (2013b). Monitoring and modeling farmland productivity along the venice coastland, italy. *Procedia Environ. Sci.*, 19:361–368.

Manoli, G., Rossi, M., Pasetto, D., Deiana, R., Ferraris, S., Cassiani, G., and Putti, M. (2013c). An iterative particle filter approach for coupled hydro-geophysical inversion of a controlled infiltration experiment. *Submitted.*

Manzoni, S., Vico, G., Katul, G.and Fay, P., Polley, W., Palmroth, S., and Porporato, A. (2011). Optimizing stomatal conductance for maximum carbon gain under water stress: a meta-analysis across plant functional types and climates. *Func. Ecol.*, 25:456–467.

Maxwell, R. M., Chow, F. K., and Kollet, S. J. (2007). The groundwater-land-surface-atmosphere connection: Soil moisture effects on the atmospheric boundary layer in fully-coupled simulations. *Adv. Water Resources*, 30:2447–2466.

Mendel, M., Hergarten, S., and Neugebauer, H. J. (2002). On a better understanding of hydraulic lift: A numerical study. *Water Resour. Res.*, 38:1183.

Menke, W. (1984). *Geophysical Data Analysis: Discrete Inverse Theory.* Elsevier, New York.

Milly, P. C. D. (1993). An analytical solution of the stochastic storage problem applicable to soil water. *Water Resour. Res.*, 29:3755–3758.

Montzka, C., Moradkhani, H., Weihermüller, L., Hendricks Franssen, H.-J., Canty, M., and Vereecken, H. (2011). Hydraulic parameter estimation by remotely-sensed top soil moisture observations with the particle filter. *J. Hydrol.*, 399(3–4):410–421.

Moradkhani, H., DeChant, C. M., and Sorooshian, S. (2012). Evolution of ensemble data assimilation for uncertainty quantification using the particle filter-Markov chain Monte Carlo method. *Water Resour. Res.*, 48(12):W12520.

Moradkhani, H., Hsu, K.-L., Gupta, H., and Sorooshian, S. (2005). Uncertainty assessment of hydrologic model states and parameters: Sequential data assimilation using the particle filter. *Water Resour. Res.*, 41(5):W05012.

Nenna, V., Pidlisecky, A., and Knight, R. (2011). Application of an extended Kalman filter approach to inversion of time-lapse electrical resistivity imaging data for monitoring recharge. *Water Resour. Res.*, 47(10):W10525.

Neumann, R. B. and Cardon, Z. G. (2012). The magnitude of hydraulic redistribution by plant roots: a review and synthesis of empirical and modeling studies. *New Phytol.*, 194:337–352.

Novick, K., Oren, R., Stoy, P., Siqueira, M., and Katul, G. G. (2009). Nocturnal evapotranspiration in eddy-covariance records from three co-located ecosystems in the Southeastern U.S.: Implications for annual fluxes. *Agricultural and Forest Meteorology*, 149:1491–1504.

Paniconi, C. and Putti, M. (1994). A comparison of Picard and Newton iteration in the numerical-solution of multidimensional variably saturated flow problems. *Water Resour. Res.*, 30(12):3357–3374.

Pasetto, D., Camporese, M., and Putti, M. (2012). Ensemble Kalman filter versus particle filter for a physically-based coupled surface-subsurface model. *Adv. Water Resources*, 47(1):1–13.

Plaza, D. A., De Keyser, R., De Lannoy, G. J. M., Giustarini, L., Matgen, P., and Pauwels, V. R. N. (2012). The importance of parameter resampling for soil moisture data assimilation into hydrologic models using the particle filter. *Hydrol. Earth Syst. Sci.*, 16:375–390.

Porporato, A., E., D., and Rodriguez-Iturbe, I. (2004). Soil water balance and ecosystem response to climate change. *Am. Nat.*, 164(5):625–632.

Richard, J. T. V., Higgins, S. I., Bond, W. J., and C., F. E. (2011). Water sourcing by trees in a mesic savanna: responses to severing deep and shallow roots. *Environmental and Experimental Botany*, 74:229–236.

Rings, J. and Hauck, C. (2009). Reliability of resistivity quantification for shallow subsurface water processes. *J. Appl. Geophys.*, 68:404–416.

Rings, J., Huisman, J. A., and Vereecken, H. (2010). Coupled hydrogeophysical parameter estimation using a sequential Bayesian approach. *Hydrol. Earth Syst. Sci.*, 14:545–556.

Ritchie, J. T. (1998). Soil water balance and plant water stress. In Tsuji, G., Hoogenboom, G., and P.K, T., editors, *Understanding Options for Agricultural Production*, pages 41–55. Kluwer Academic Publishers, Dordrecht, The Netherlands.

Rodrguez-Iturbe, I., D'Odorico, P., Porporato, A., and Ridolfi, L. (1999a). Tree-grass coexistence in savannas: The role of spatial dynamics and climate fluctuations. *Geophys. Res. Lett.*, 26:247–250.

Rodrguez-Iturbe, I. and Porporato, A. (2004). *Ecohydrology of Water-Controlled Ecosystems*. Cambridge University Press, New York.

Rodrguez-Iturbe, I., Porporato, A., Ridolfi, L., Isham, V., and Cox, D. (1999b). Probabilistic modelling of water balance at a point: the role of climate, soil and vegetation. *Proc. R. Soc. Lond. A*, 455:3789–3805.

Rossi, M., Manoli, G., Pasetto, D., Deiana, R., Ferraris, S., Strobbia, C., Putti, M., and Cassiani, G. (2013). Quantitative hydro-geophysical monitoring and modeling of a controlled infiltration experiment. *Submitted*.

Salamon, P. and Feyen, L. (2009). Assessing parameter, precipitation, and predictive uncertainty in a distributed hydrological model using sequential data assimilation with the particle filter. *J. Hydrol.*, 376(3–4):428–442.

Samuelson, L., Stokes, T., Cooksey, T., and McLemore, P. t. (2001). Production efficiency of loblolly pine and sweetgum in response to four years of intensive management. *Tree Phys.*, 21:369–376.

Santanello, J. A., Friedl, M. A., and Ek, M. B. (2007). Convective planetary boundary layer interactions with the land surface at diurnal time scales: Diagnostics and feedbacks. *J. Hydrometeorol.*, 8:1082–1097.

Santini, A. (2013). Four decades of progress in monitoring and modeling of processes in the soil-plant- atmosphere system: Applications and challenges. *Procedia Environ. Sci.*, 19:1–2.

Scudiero, E., Deiana, R., Teatini, P., Cassiani, G., and Morari, F. (2011). Constrained optimization of spatial sampling in salt contaminated coastal farmland usingEMI and continuous simulated annealing. *Procedia Environ. Sci.*, 7:234–239.

Siqueira, M., Katul, G., and Porporato, A. (2008). Onset of water stress, hysteresis in plant conductance, and hydraulic lift: Scaling soil water dynamics from millimeters to meters. *Water Resour. Res.*, 44:WR01432.

Siqueira, M., Katul, G., and Porporato, A. (2009). Soil Moisture Feedbacks on Convection Triggers: The Role of SoilPlant Hydrodynamics. *J. Hydrometeorol.*, 10:96–112.

Smith, P. J., Dance, S. L., Baines, M. J., Nichols, N. K., and Scott, T. R. (2009). Variational data assimilation for parameter estimation: application to a simple morphodynamic model. *Ocean Dyn.*, 56:697–708.

Srayeddin, I. and Doussan, C. (2009). Estimation of the spatial variability of root water uptake of maize and sorghum at the field scale by electrical resistivity tomography. *Plant Soil*, 3:185–207.

Sun, G., Noormets, A., Gavazzi, M. J., McNulty, S. G., Chen, J., Domec, J. C., King, J. S., Amatya, D. M., and Skaggs, R. W. (2010). Energy and water balance of two contrasting loblolly pine plantations on the lower coastal plain of North Carolina, USA. *Forest. Ecol. Manag.*, 259:1299–1310.

Supit, I., Hoijer, A. A., and van Diepen, C. A. (1994). *System description of the WOFOST 6.0 crop simulation model implemented in CGMS, vol. 1: Theory and Algorithms*. Joint Research Centre, Commission of the European Communities, EUR 15956 EN, Luxembourg.

Teatini, P., Tosi, L., Viezzoli, A., Baradello, L., Zecchin, M., and Silvestri, S. (2011). Understanding the hydrogeology of the venice lagoon subsurface with airborne electromagnetics. *J. Hydrol.*, 411:342–354.

Tennekes, H. (1973). A Model for the Dynamics of the Inversion Above a Convective Boundary Layer. *J. Atmos. Sci.*, 30:558–567.

van Dam, J. C., Huygen, J., Wesseling, J. G., Feddes, R. A., Kabat, P., van Walsum, P. E. V., Groenedijk, P., and van Diepen, C. A. (1997). Theory of SWAP Version 2.0. Technical report, Department Water Resources, Wageningen Agricultural University.

van den Doel, K. and Ascher, U. M. (2006). On level set regularization for highly ill-posed distributed parameter estimation problems. *J. Comp. Phys.*, 216:707–723.

van Genuchten, M. T. and Hoffman, G. (1984). Analysis of crop salt tolerance data. In Shainberg, I. and Shalhevet, J., editors, *Soil Salinity under Irrigation, Processe and Management*, volume 51, pages 258–271. Springer Verlag, New York.

van Genuchten, M. T. and Nielsen, D. R. (1985). On describing and predicting the hydraulic properties of unsaturated soils. *Ann. Geophys.*, 3(5):615–628.

van Laar, H. H., Goudriaan, J., and van Keulen, H. (1997). *SUCROS 97: Simulation of crop growth for potential and water-limited production situations.* DLO Research Institute for Agrobiology and Soil Fertility.

Vogel, T., Dohnal, M., Dusek, J., Votrubova, J., and Tesar, M. (2013). Macroscopic Modeling of Plant Water Uptake in a Forest Stand Involving Root-Mediated Soil Water Redistribution. *Vadose Zone J.*

Volpe, V., Manzoni, S., Marani, M., and Katul, G. (2011). Leaf conductance and carbon gain under salt-stressed conditions. *J. Geophys. Res.*, 116:G04035.

Volpe, V., Marani, M., Albertson, J. D., and Katul, G. (2013). Root controls on water redistribution and carbon uptake in the soilplant system under current and future climate. *Adv. Water Resources*, 60:110–120.

Vrugt, J. A., Diks, C. G. H., Gupta, H. V., Bouten, W., and Verstraten, J. M. (2005). Improved treatment of uncertainty in hydrologic modeling: Combining the strengths of global optimization and data assimilation. *Water Resour. Res.*, 41(1):W01017.

Vrugt, J. A., ter Braak, C. J. F., Diks, C. G. H., and Schoups, G. (2012). Hydrologic data assimilation using particle markov chain Monte Carlo simulation: Theory, concepts and applications. *Adv. Water Resources*, 51:457–478.

Šimůnek, J., van Genuchten, M. T., and Šejna, M. (March 2006). The HYDRUS Software Package for Simulating the Two- and Three-Dimensional Movement of Water, Heat, and Multiple Solutes in Variably-Saturated Media. Technical report, PC-Progress, Prague, Czech Republic.

Weerts, A. H. and El Serafy, G. Y. H. (2006). Particle filtering and ensemble Kalman filtering for state updating with hydrological conceptual rainfall-runoff models. *Water Resour. Res.*, 42(9):W09403.

Yeh, T. C. J. and Šimůnek, J. (2002). Stochastic fusion of information for characterizing and monitoring the vadose zone. *Vadose Zone J.*, 1(2):207–221.

Zhou, Q. Y., Shimada, J., and Sato, A. (2002). Temporal variations of the three-dimensional rainfall infiltration process in heterogeneous soil. *Water Resour. Res.*, 38(4):1–1–1–15.

Zhou, Y., McLaughlin, D., and Entekhabi, D. (2006). Assessing the performance of the ensemble Kalman filter for land surface data assimilation. *Mon. Weather Rev.*, 134(8):2128–2142.